Spectroscopic Study of Highly Ionised Plasmas : Detailed and Statistical Approaches

Xieyu Na

université PARIS-SACLAY

NNT : 2017SACLS592

Thèse de doctorat

Spectroscopic Study of Highly Ionized Plasmas: Detailed and Statistical Approaches

Thèse de doctorat de l'Université Paris-Saclay
préparée à l'Université Paris-Sud

École doctorale n°572 ondes et matière (EDOM)
Spécialité de doctorat: physique des plasmas

Thèse présentée et soutenue à Palaiseau, le 16 Novembre 2017, par

Mme. Xieyu Na

Composition du Jury :

Mme. Lydia Tchang-Brillet Professeur émérite, Université Pierre-et-Marie Curie / Observatoire de Paris-Meudon / CNRS / ENS / Université Cergy-Pontoise (-UMR 8112)	Présidente
Mme. Annette Calisti DR au CNRS, Université Aix-Marseille / CNRS (-UMR 7345)	Rapporteur
M. Gérard Massacrier CR au CNRS, CNRS / ENS Lyon (-UMR 5574)	Rapporteur
M. Djamel Benredjem Professeur, Université Paris-Sud / CNRS (-UMR 9188)	Examinateur
M. Jean-Marcel Rax Professeur, Ecole Polytechnique / Université Paris-Sud / CNRS / ENSTA (-UMR 7639)	Examinateur
M. Michel Poirier Ingénieur CEA, CEA / CNRS (-UMR 9222)	Directeur de thèse

To my grandma, with endless love

Acknowledgment

> Il n'y a qu'un héroïsme au monde: c'est de voir le monde tel qu'il est, et de l'aimer.
>
> Romain Rolland

Après plusieurs tentatives de rédiger cette partie avant la soutenance, je pensais pouvoir être plus posée une fois devenue Dr.Na. Mais non, les sentiments de gratitude et de reconnaissance continuent de me mettre dans un état suffisamment effervescent que mon sens de l'objectivité physicienne est mis à l'épreuve. S'il y a une hiérarchie à laquelle est soumise une vie matérielle, le plus haut placé sera peut-être le temps. Ainsi retraçons quelques souvenirs par ordre chronologique.

"Le langage est source de malentendus"

Tout a commencé par la prise de contact avec Michel Poirier, rendue possible grâce à la plateforme du Master de Fusion.

Une fois admise aux concours d'EDOM – dont la préparation a été assistée par Michel et Frédéric Thais, je me joins au groupe MHDE/LIDYL/IRAMIS/DSM/CEA qui comptait Maylis Dozières en 2ème année, Clément Caizergues et Madeny Belkhiri en fin de thèse, Michel, Frédéric et Thomas Blenski comme permanents. Les documents administratifs étaient transférés à Jacqueline Bandura et signés par Philippe Martin. Le prêt et le retour des livres sont assurés par la Bibliothèque de Saclay. Je prenais la succession de Madeny, qui m'a notamment initiée au fonctionnement du code FAC. Je partageais le même bureau avec Maylis pendant deux ans. Le temps du déjeuner fut l'occasion d'échanges au sein du groupe MHDE, rejoint de temps en temps par Robin Piron et agrandi avec l'arrivée de Dominique Gilles. Les sujets de discussion étaient la plupart du temps d'ordre socio-géo-politique.

Concernant les missions doctorales, Philippe Caillou m'a contactée pour un monitorat à l'IUT de Sceaux, encadrée par Isabelle Bournaud. J'ai sous ma responsabilité deux groupes, chacun composé d'une vingtaine d'étudiants.

Thomas m'a suggéré de participer au 7ème Forum Lasers et Plasmas où j'ai rencontré Franck Gilleron et Jean-Christophe Pain. Franck m'a montré un exemple de calcul de variance en utilisant les opérateurs de la 2nd quantification et l'algèbre de Racah. Jean-Christophe m'a donné l'idée d'implémenter les pseudo-UTAs, m'a envoyé les cours ainsi que le livre des Bauche à sa publication.

Après un an de trajets quotidiens, fatigants comme m'en avait avertie Michel, j'ai déménagé de Paris à Palaiseau dont la proximité m'a permis de m'impliquer davantage dans la vie culturelle et sportive du centre. Frédéric m'a présentée à Sylvie Jubera et Pascal Salières. Sylvie m'a accueillie dans son groupe de jogging qui court les mardis et jeudis midis. Au retour, je retrouvais

souvent Stéphane Guizard et Allan Bildé au déjeuner. Pascal m'a mise en contact avec Bernard Crabol, qui m'a inscrite au cours de la classe de piano de l'AACCEA avec Julie Safarova. Suite au forum annuel de l'AACCEA, Modeste Donati a partagé l'annonce de Brigitte Schalber grâce à qui j'ai eu le premier piano acoustique à moi, emménagé à l'aide des amis. Éric Vincent m'a autorisée à faire partie de la classe jusqu'à la fin de ma thèse. Julie m'a mise en relation avec Frédérique Napoléone pour le concert à 4 mains.

Au cours de ma thèse, Michel et Thomas m'ont donné les opportunités de participer aux divers formations et échanges internationaux. Avec Michel, nous avons publié 2 articles. Je prends conscience de mon évolution progressive au niveau de l'autonomie et de la communication.

En rassemblant mes notes en LaTeX, j'entamais la rédaction de la thèse. À chaque version du manuscrit, Michel m'envoyait une version de commentaires. Michel, Philippe M. et Jacques Robert ont signé les documents relatifs à la soutenance. Le manuscrit fut rapporté par Annette Calisti et Gérard Massacrier qui ont contribué à son amélioration et qui m'ont autorisée à passer la soutenance. Lydia Tchang-Brillet, Djamel Benredjem et Jean-Marcel Rax ont accepté d'être membres du jury. Thomas, Dominique et Michel ont assisté aux répétitions et m'ont donné des conseils.

"Le sentier qui finit où le chemin commence"

Avec Frédérique et Julie, nous compléterons sans doute le travail sur la Fantaisie de Schubert avec au moins le 2ème mouvement. Avec Françoise Thais et Frédéric, nous organiserons sans doute d'autres échanges culinaires et musicaux. Avec Dominique, nous ne manquerons sans doute pas d'occasion de nous balader dans la nature comme en ville.

Un jour, Michel partagera peut-être son expertise montagnarde avec ses doctorants, anciens et nouveaux. Un jour, X. Na apparaîtra peut-être dans des articles à côté de A. Calisti, G. Massacrier, F. Gilleron, J-C. Pain, M. Poirier, et al. Un jour, madame encadrera peut-être ses doctorants qui lui feront confesser le temps jadis auprès de son directeur de thèse.

Quoi qu'il advienne, ce qui se décante de ce sentier de 38 mois continue certainement à m'inspirer sur de nouveaux chemins: à savoir le dévouement au travail, la force de la culture et de la connaissance, l'importance de confronter les différences culturelles – entre "ne pas déranger" et "prendre l'initiative" par exemple – et de s'y adapter, la persévérance et l'envie constante de se dépasser dans une course, la profondeur et la finesse procurées par les émotions musicales, l'égalité des chances, l'intelligence de comprendre les besoins d'autrui et la bonté d'essayer de les satisfaire.

Enfin, je voudrais remercier toutes les personnes impliquées, et en dépassant le cadre de la thèse, rendre hommage à l'amour et à l'amitié que me témoignent familles et amis. Quoi que je devienne, je sais qu'à vos yeux, je suis toujours la même.

Palaiseau, automne 2017

Contents

List of Figures

List of Tables

Part I

Synthèse en français

Étude spectroscopique des plasmas hautement ionisés : approches détaillée et statistique

Les spectres d'absorption et d'émission dans des plasmas chauds, comme ceux rencontrés en astrophysique et en sciences de la fusion nucléaire, présentent souvent des structures complexes. Afin de les interpréter, il existe des méthodes dites statistiques qui décrivent les ensembles non résolus de raies par des structures dites faisceaux de transition. Par rapport aux méthodes détaillées qui tentent de calculer les spectres raie par raie en nécessitant la diagonalisation de l'hamiltonien du système considéré, les méthodes statistiques sont basées sur la détermination des moments de distribution, qui met en jeu le calcul des moyennes en configuration. L'objet de cette thèse consiste à comparer les deux approches – détaillée et statistique, en utilisant notamment le code de structure atomique FAC (Flexible Atomic Code).

Dans cette synthèse, le sujet de la thèse est présenté dans un premier temps à travers ses mots clés. Puis, quelques éléments sont extraits des deux travaux publiés au cours de la thèse, dont l'un numérique sur la modélisation des spectres des transitions dipolaires magnétiques dans des plasmas de tungstène, et l'autre analytique sur le calcul des moyennes des énergies spin-orbite dans une configuration multi-électronique. Enfin, la synthèse se termine par une conclusion composée d'un résumé de travaux effectués et de plusieurs perspectives proposées.

0.1 Présentation du sujet

Plasma

Généralement considéré comme le 4ème état de matière, un plasma est constitué d'un ensemble de particules chargées s'interagissant par des forces électromagnétiques.
Les plasmas de grandes variations de températures T et de densités n, cf. Fig. 1.1 et Table 1, sont caractérisés par leur capacité de maintenir *l'état de quasi-neutralité*, traduit par l'égalité des charges positives et négatives

$$n_e = Z \times n_i \tag{1}$$

où $n_{e,i}$ =densités électronique, ionique, Z =degré d'ionization moyen, et s'explique par les paramètres fondamentaux tels que la *longueur de Debye*

$$\lambda_D \propto \sqrt{T_e/n_e}. \tag{2}$$

	Haute	Basse
T_e	$\gtrsim 10^7$K	$\lesssim 2\times10^4$K
n_i	$\gtrsim 10^{23}$m^{-3}	$\lesssim 10^{25}$m^{-3}

Table 1: Classification - grosso modo - des domaines d'étude des plasmas en fonction de leurs températures et densités.

Spectroscopie atomique

La physique des plasmas chauds représente un champ d'études multi-disciplinaires, parmi lesquelles l'étude des spectres radiatifs atomiques, qui sont principalement de deux types : en émission et en absorption, l'intensité $I(\lambda)$ et l'opacité $\kappa(\lambda)$ respectivement sont représentées en fonction des longueurs d'onde (ou de façon équivalente des énergies $I(E), \kappa(E)$) des photons mis en jeu.
La spectroscopie atomique joue un rôle essentiel dans le diagnostic des propriétés radiatives des plasmas sur le plan expérimental, qui permet de contribuer en contrepartie au développement théorique de la physique atomique dans leur sein. Une illustration d'étude expérimentale de la spectroscopie des plasmas de cuivre du laboratoire est montrée dans la Fig. 1.

Quant à la plupart des calculs atomiques, le point de départ consiste à déterminer la structure électronique des éléments atomiques du plasma étudié, comme les énergies de niveaux et de configurations.

- Un niveau est caractérisé par des nombres quantiques tels que n, l, m_l, m_s;
- Une configuration désigne un ensemble de sous-couches électroniques partageant les m valeurs de
  - (n_i, l_i) dans le cas non relativiste:

$$C_{\rm nr} = (n_1 l_1)^{\nu_1} (n_2 l_2)^{\nu_2} ... (n_p l_p)^{\nu_p} \tag{3}$$

  - (n_i, l_i, j_i) dans le cas relativiste:

$$C_{\rm r} = (n_1 l_1 j_1)^{\omega_1} (n_2 l_2 j_2)^{\omega_2} ... (n_q l_q j_q)^{\omega_q} \tag{4}$$

  où ν_i, ω_i sont les nombres d'occupation de i, tels que

$$\nu_i^{\max} = 2(2l_i + 1), \quad \omega_i^{\max} = 2j_i + 1. \tag{5}$$

Les dégénérescences des configurations g_C s'obtiennent en fonction de celles des sous-couches g_i:

$$g_{C_{\rm nr}} = \prod_{i=1}^{p} g_{i,{\rm nr}}, \quad g_{C_{\rm r}} = \prod_{i=1}^{q} g_{i,{\rm r}} \tag{6}$$

où

$$g_{i,{\rm nr}} = \binom{\nu_i^{max}}{\nu_i}, \quad g_{i,{\rm r}} = \binom{\omega_i^{max}}{\omega_i} \tag{7}$$

Par exemple, $g(3s3p^4) = \binom{2}{1}\binom{6}{4} = g(s)\cdot[g(p_+^4) + g(p_- p_+^3) + g(p_-^2 p_+^2)] = 30.$

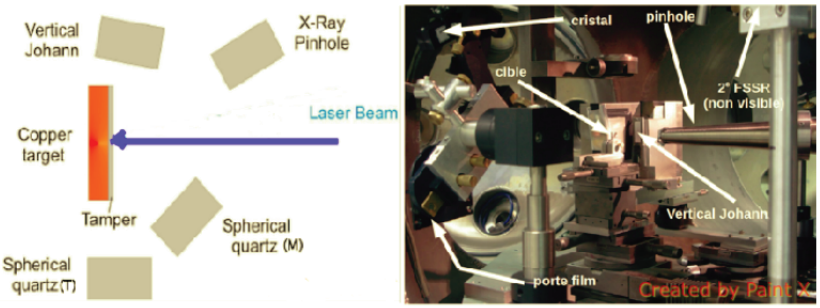

(a) Création de plasmas par interaction laser-cible solide

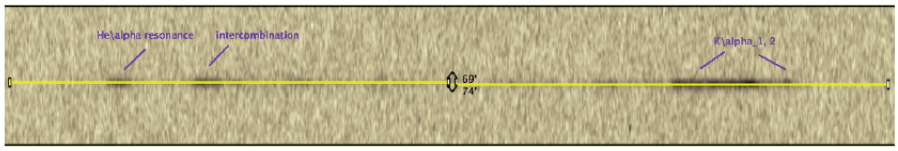

(b) Recueil des données spectrales sur film

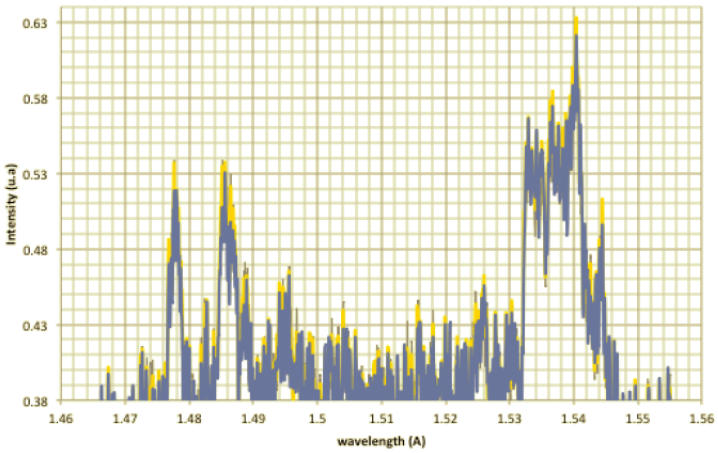

(c) Représentation des spectres expérimentaux $I(\lambda)$

Figure 1: Illustration d'étude expérimentale de la spectroscopie des plasmas de cuivre du laboratoire (Source: travaux du stage Master 2 sur les ions creux).

Généralement, deux classes de modèles de la physique atomique dans des plasmas sont utilisées :

- détaillée, qui consiste à construire les spectres en sommant raie par raie;
- statistique, qui regroupe des approches différentes telles que la description d'atome moyen statistique ($1s^{0,95}\ 2s^{0,89}$... à (n,T) donné) et les méthodes de moyenne, par exemple pour moyenner les niveaux en configuration ($1s^2\ 2s\ 2p$), voire en supraconfiguration ($(1s)^2\ (2s2p)^2$).

Dans cette thèse, nous nous focalisons sur les méthodes qui moyennent les niveaux en configuration et nous allons considérer les faisceaux de transition. Alors qu'une *raie* spectrale traduit une transition électronique entre 2 niveaux, un *faisceau* désigne l'ensemble des transitions entre les niveaux de 2 configurations.

Modèle UTA (Unresolved Transition Array) – Faisceau de transition non-résolue

Dans les spectres des plasmas hautement ionisés, deux caractéristiques sont souvent présentes. D'une part, le nombre de raies les constituant peut être très important, lié par exemple aux transitions parmi un nombre élevé de sous-couches électronique ouvertes. De l'autre part, les raies d'énergies voisines sont susceptibles de se recouvrir en formant des structures non-résolues. Un exemple pertinent se trouve dans la Figure 2.2 du livre des Bauche et de Peyrusse (2015). Ainsi est-il adéquat d'appliquer le modèle UTA dans l'interprétation de tels spectres.

Le modèle UTA est basé sur le calcul des moments $\mu_n[X]$ ainsi qu'au choix des fonctions F de distribution. Les moments de distribution d'ordre n s'écrivent :

$$\mu_n[X] = \frac{\sum_{i=1}^{N}(X_i)^n\omega_i}{\sum_{i=1}^{N}\omega_i}, \quad \omega_i = \text{poids statistiques de } X_i \tag{8}$$

En spectroscopie statistique, il est d'usage d'étudier par exemple

- la distribution des énergies de raies $X_i = E_{ab}$ pondérées par leurs forces $\omega_i = f_{ab}$;
- la distribution des énergies $X_i = E_a$ des niveaux par leurs dégénérescences $\omega_i = g_a$; etc.

En générale, les 4 premiers ordres, qui représentent respectivement

- $\mu_1 =$ la moyenne,
- $\mu_2 =$ la variance,
- $\mu_3 =$ la dissymétrie,
- $\mu_4 =$ l'aplatissement

d'une distribution, permettent d'en caractériser globalement son profil. Et les fonctions de distribution usuelles $F(\mu_n[X])$ sont de type Gaussien, Gram-Charlier, Gaussien généralisé, etc.

Comme illustration, en utilisant le code FAC, les transitions $3d^24p - 3d^24s$ dans les plasmas de KrX et ZrXIV sont calculées en modes détaillé et UTA, dont les spectres sont montrés dans la Fig. 3.1.

0.2 Modélisation des spectres

Problématique étudiée

Afin d'explorer l'une des caractéristiques des plasmas hautement ionisés, qui est l'importance croissante des transitions dipolaires magnétiques M_1 par rapport au type dipolaire électrique E_1, nous nous intéressons à la contribution lié-lié des transitions M_1 dans le cas du complex $3*14$ (14 électrons dans les sous-couches de $n=3$) dans les plasmas de tungstène ($W, Z=74$) de charges aux alentours de 50+, en régime de température-densité équivalent du tokamak d'ITER.

Nous allons comparer les spectres d'émission détaillés et UTA avec le code FAC, qui est un code atomique relativiste, bien adapté aux cas des éléments lourds fortement chargés. Son mode UTA calcule des faisceaux de transitions entre les configurations relativistes C_r.

Cette étude est motivée par deux aspects notamment: d'un côté, l'élément tungstène W étant choisi comme composant du divertor du tokamak d'ITER, le calcul de sa perte radiative suscite d'intérêt dans la communauté de la fusion nucléaire; de l'autre côté, vis-à-vis de la spectroscopie statistique des raies interdites, il s'agit de tester l'implémentation dans le code FAC des formules analytiques des moments μ_n pour les transitions du type M_1, obtenues récemment.

Construction des spectres liés-liés

Les spectres liés-liés résultent des transitions spontanées et stimulées qui sont caractérisées par les coefficients d'Einstein – A_{21}, B_{21}, B_{12}, à partir desquels se définissent les paramètres spectroscopiques tels que la force des raies f, etc. Dans le cas des spectres d'émission, l'intensité d'émission s'écrit

$$I(E_{ab}) = n_i \sum_{ab} p_a A_{ab} E_{ab} S_{ab} \tag{9}$$

avec n_i =densité ionique, p_a =population a, A_{ab} =taux de transition $a \to b$ et S_{ab} =profil ab, où selon l'option choisie, a, b peuvent désigner deux niveaux ou configurations et ab une raie ou un faisceau.

Le code atomique FAC nous fournit les quantités E, A, g, f soit par diagonalisation de l'Hamiltonien dans l'option détaillée, soit avec les formules analytiques des moments (ex. σ i.e. μ_2) préalablement implémentées dans l'option UTA. Nous avons écrit un post-processeur afin de calculer les quantités p, S de l'Eq.(9). Plus précisément, nous avons fait les choix suivants :

- $S =$ profil Gaussien

  $$S(E) = \frac{1}{\sqrt{2\pi}\sigma} e^{-\frac{(E-\mu_1)^2}{2\sigma^2}} \tag{10}$$

  avec $\sigma^2_{\text{Détail}} = \sigma^2_{\text{Doppler}}$ et $\sigma^2_{\text{UTA}} = \mu_2^c + \sigma^2_{\text{Doppler}}$;

- $p =$ loi Saha-Boltzmann

  En effet, basé sur la théorie de la *température effective* T_{eff} – température qui en supposant la loi de Saha-Boltzmann pour T_e^{ETL} donnerait la même charge moyenne que par le calcul hors ETL, et en utilisant le code FLYCHK – doté des modèles collisionnel-radiatif et ETL, nous avons constaté qu'à la densité $n_e = 10^{14}\text{cm}^{-3}$, la température effective T_{eff} de $T_e^{\text{hors ETL}} \approx 8800$ eV est de $T_e^{\text{ETL}} \approx 200$eV, cf. Fig. 2.2.

Comme exemple, les spectres d'émission des transitions M_1 du complex $3*14$ dans un plasma de W^{50+} sont représentés dans la Fig. 2. Alors que les pics d'émission sont correctement reproduits,

nous notons un écart significatif entre spectres détaillés et UTA dans les ailes de ces structures, par exemple entre 500 et 800 eV.

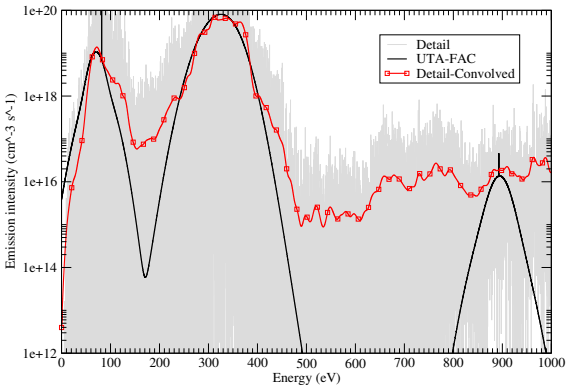

Figure 2: Spectres d'émission détaillés et UTA : transitions M_1 du complex $3*14$ dans W^{50+}, à la densité $n_e = 10^{14}\text{cm}^{-3}$, la température effective $T_{\text{eff}} \approx 200\text{eV}$. Distribution Gaussienne construite avec ses 2 premiers moments statistiques.

Procédure pseudo-UTA numérique

Afin d'élucider la disparité observée entre les spectres M_1 détaillés et UTA, deux hypothèses sont émises : la disparité est lié

- soit au choix de profil statistique, notamment à l'absence des moments d'ordre élevé;
- soit au manque de raies prises en compte dans les formules UTA du code.

Pour les vérifier, nous avons implémenté une procédure numérique de pseudo-UTA qui consiste à post-traiter les données de sortie détaillées – en regroupant des niveaux en configurations et des raies en UTAs, permettant ainsi de fabriquer numériquement des moments d'ordre quelconque

$$\mu_{\alpha\beta}^{(k)} = \left\langle (E - E_{\alpha\beta})^k \right\rangle = \frac{\sum_{\substack{a\in\alpha \\ b\in\beta}} g_a f_{ab} \left(E_{ab} - E_{\alpha\beta}\right)^k}{\sum_{\substack{a\in\alpha \\ b\in\beta}} g_a f_{ab}}. \tag{11}$$

Comme montre la Fig. 3, l'excellent accord a été constaté entre les spectres détaillé et pseudo-UTA Gaussien, i.e. construit à partir de 2 moments seulement. Ainsi pouvons-nous éliminer l'hypothèse liée à l'absence des moments d'ordre élevé.

En effet, dans le cas de W^{50+}, les 18513 raies calculées par FAC correspondent aux 91 UTAs selon l'option UTA du code, alors qu'elles se regroupent en 649 pseudo-UTA selon notre post-processeur. En comparant avec les données de sortie UTA de FAC, nous avons constaté que seule une partie de raies résultant des transitions entre 2 configurations C_r différentes, notées par $InterL$, a été prise en compte par l'option UTA de FAC. Parmi les données de sortie détaillées de FAC, il s'avère que 2 catégories de raies sont négligées par les formules UTA implémentées :

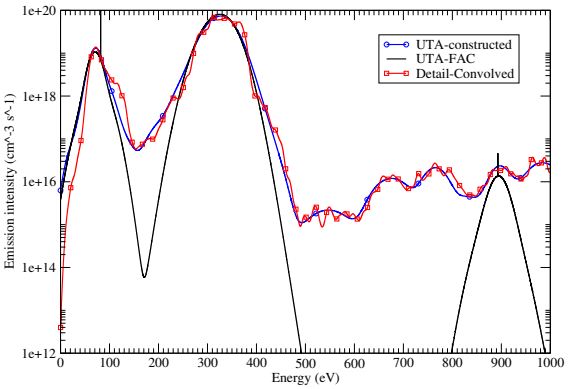

Figure 3: Spectres d'émission détaillés, pseudo-UTA, UTA : transitions M_1 du complex $3*14$ dans W^{50+}. Excellent accord entre spectres détaillé et pseudo-UTA Gaussien, i.e. construit avec seulement 2 moments.

- $InterNL$ = une partie de transitions inter-configurationnelles; il s'agit essentiellement des transitions multi-électroniques, par ex. $3d^2_{3/2} \rightarrow 3d^2_{5/2}$, rendues possible par l'effet des *interactions de configuration*.
- $Intra$ = toutes les transitions intra-configurationnelles, i.e. ayant lieu au sein d'une même configuration, permises par les règles de sélection des transitions M_1 (contrairement à celles des E_1).

W^{50+}(3*14)	Nombre	Emissivité
Inter L	5124	2,74(9)
Inter NL	12462	1,32(8)
Intra	927	5,65(5)
Totale	18513	2,87(9)

Table 2: Nombre de raies et leurs contributions intégrées aux spectres des transitions M_1 du complex $3*14$ dans W^{50+}. Émissivité=$\sum_{ab} p_b E_{ab} A_{ba}$. La notation 2,74(9) signifie $2,74 \times 10^9$.

L'ensemble des 3 catégories de raies ainsi que leurs contributions respectives en termes de nombre et d'émissivité sont représentées dans la Fig. 4 et la Table 2, en prenant toujours le cas des transitions M_1 du complex $3*14$ dans W^{50+}. Malgré le nombre relativement faible des raies $InterL$, leur contribution spectrale reste majoritaire parmi les 3 catégories, ce qui est rassurant.

0.3 Calcul des moyennes

Problématique étudiée

Dans cette section, nous explorons une autre caractéristique des plasmas hautement ionisés, qui est l'importance croissante de l'effet spin-orbite $V_{\rm so}$ par rapport à l'effet Coulombien $V_{\rm ee}$.

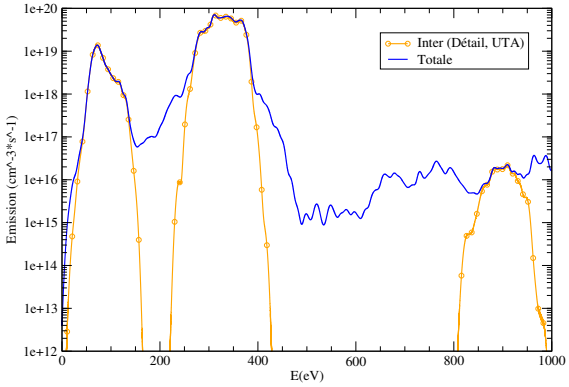

(a) *InterL* : transitions détaillées Inter-configurationnelles Listées parmi les données de sortie UTA de FAC.

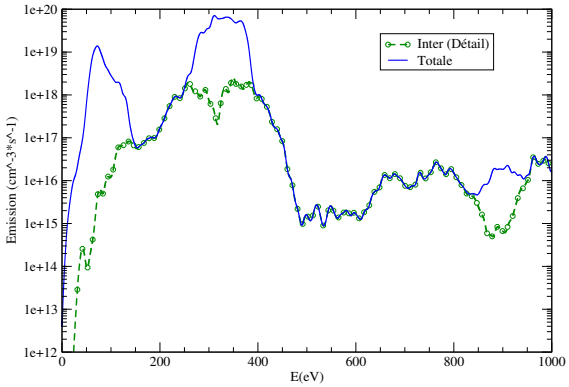

(b) *InterNL* : transitions détaillées Inter-configurationnelles Non Listées

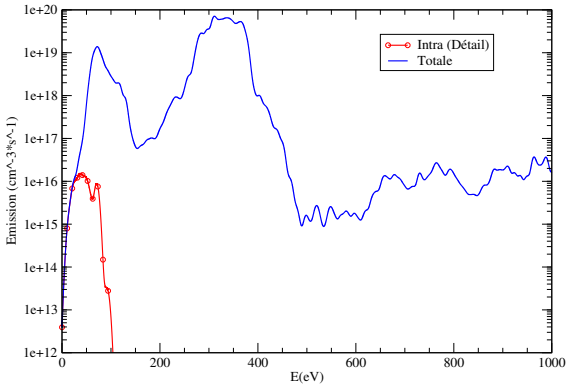

(c) *Intra* : transitions détaillées Intra-configurationnelles manquantes (spécificité des transitions M_1 par rapport à celles de E_1)

Figure 4: Spectres d'émission détaillés des transitions M_1 du complex $3*14$ dans W^{50+} : 3 catégories de raies ainsi que leurs contributions respectives à l'émissivité totale.

Rappelons que l'Hamiltonien perturbatif dans l'approximation semi-relativiste s'écrit

$$H = \sum_{i=1,N} \left(\frac{p_i^2}{2} - \frac{Z}{r_i} \right) + V_{\text{ee}} + V_{\text{so}}, \tag{12}$$

en nous plaçant dans la situation où le numéro Z du plasma considéré est élevé, l'effet spin-orbite V_{so} l'emporte sur l'effet Coulombien V_{ee}.

L'étude des moments $\mu_n(V_{\text{so}})$ des énergies spin-orbite dans une configuration multi-électronique nous amène au calcul des moyennes de type $\left\langle C \mid V_{\text{so}}^k \mid C \right\rangle \equiv \left\langle V_{\text{so}}^k \right\rangle_N$ où la configuration peut être relativiste ou non, i.e. $C \equiv C_{\text{nr}} = (nl)^N$ ou $C \equiv C_{\text{r}} = (nlj_-)^\nu (nlj_+)^{N-\nu}$. L'opérateur V_{so} peut s'écrire préférentiellement de deux façons, selon la base utilisée:

- soit en termes d'opérateurs $l_\pm, l_z$ dans la base non couplée $|lm_l s\sigma\rangle$

$$V_{\text{so}} = \sum_p \xi(r_p) \left[\frac{1}{2}(l_{p+} s_{p-} + l_{p-} s_{p+}) + l_{pz} s_{pz} \right], \tag{13}$$

- soit en fonction des j, l, s dans la base couplée $|lsjm\rangle$

$$V_{\text{so}} = \sum_p \xi(r_p) \frac{j_p^2 - l_p^2 - s_p^2}{2}. \tag{14}$$

Or, dans la base $|lsjm\rangle$, la matrice de V_{so} est diagonale, en considérant $C \equiv C_{\text{r}}$ par exemple, l'expression analytique de $\left\langle V_{\text{so}}^k \right\rangle_N$ s'écrit

$$\left\langle V_{\text{so}}^k \right\rangle_N = 2^{-k} \langle \xi \rangle^k \binom{4l+2}{N}^{-1} \sum_\nu \binom{2l}{\nu} \binom{2l+2}{N-\nu} (Nl - (2l+1)\nu)^k. \tag{15}$$

De manière générale, bien qu'il existe une base dans laquelle la matrice d'un opérateur hermitien est diagonale, il n'est pas forcément aisé de déterminer cette base que ce soit analytiquement (ex. dans le cas de couplage intermédiaire) ou numériquement (ex. la taille de la base élevée), la méthode des moyennes s'avère nécessaire. Nous allons l'illustrer par un exemple qui peut être traité de manière complètement analytique, qu'est le calcul du moment de l'opérateur spin-orbite à l'ordre 3, soit $\left\langle V_{\text{so}}^k \right\rangle_N, k = 3$.

Méthode du calcul des moyennes

La moyenne $\langle O \rangle$ d'un opérateur O est reliée à sa *trace* $Tr(O)$ et au facteur de dégénérescence g selon la relation

$$\langle O \rangle = \frac{Tr(O)}{g}, \tag{16}$$

où, sur une configuration à N électrons équivalents,

$$Tr(O) = \frac{1}{N!} \sum_{q_1 \cdots q_N} \sum_{\tau \in \mathcal{S}_N} \varepsilon_\tau \left\langle q_1 \cdots q_N \left| O \right| q_{\tau(1)} \cdots q_{\tau(N)} \right\rangle \tag{17}$$

avec

- q_i = nombres quantiques de l'électron i ;
- τ = permutation, ε_τ = signature de permutation.

La double-somme $\sum_{q_1\cdots q_N}\sum_{\tau\in\mathcal{S}_N}$ dans Eq. (17) peut contenir un nombre important de termes, ce qui présente une difficulté non négligeable pour mener à bien le calcul en pratique. L'une des astuces consiste à appliquer le *théorème d'Uylings* [1], qui stipule que si $O\equiv O_k$ est un opérateur à k-électron, alors sa moyenne $\langle O_k\rangle_N$ sur $C=(nl)^N$ est reliée à sa moyenne $\langle O_k\rangle_k$ sur $C=(nl)^k$ par

$$\langle O_k\rangle_N = \binom{N}{k}\langle O_k\rangle_k\,. \tag{18}$$

De ce fait, la double-somme se simplifie en $\sum_{q_1\cdots q_k}\sum_{\tau\in\mathcal{S}_k}$, souvent $k\ll N$. Concrètement, si O est une somme d'opérateurs à 1-, 2- et 3-électron, i.e. $O=O_1+O_2+O_3$, alors sa moyenne sur une configuration à N-électron se décompose comme

$$\langle O\rangle_N = \binom{N}{1}\langle O_1\rangle_1 + \binom{N}{2}\langle O_2\rangle_2 + \binom{N}{3}\langle O_3\rangle_3\,. \tag{19}$$

Illustrons la méthode des moyennes dans le cas du calcul de $\left\langle V_{\rm so}^k\right\rangle_N, k=3$.

1. Dans un premier temps, l'opérateur $V_{\rm so}^3$ s'écrit comme une décomposition de trois types d'opérateurs
$$V_{SO}^3 = \left(\sum_{q=1}^{N} l_q s_q\right)^3 = V_1 + 3V_2 + 6V_3 \tag{20}$$
respectivement à 1-, 2- et 3-électron, avec
   - $V_1=\sum_i^N (l_i s_i)^3$
   - $V_2=\sum_{i<j}(l_i s_i)^2(l_j s_j)$
   - $V_3=\sum_{i<j<p}(l_i s_i)(l_j s_j)(l_p s_p)$.

2. Puis, prenons l'exemple du calcul de moyenne $\langle V_3\rangle$ de l'opérateur à 3 électrons. En notant $f=(l_1s_1)(l_2s_2)(l_3s_3)$ et en tenant compte des permutations des 3 électrons en 2 catégories
   - permutations circulaires $((-1)^P=+1):\quad (i,j,p);\quad (j,p,i);\quad (p,i,j)$
   - permutations d'échange $((-1)^P=-1):\quad (j,i,p);\quad (i,p,j);\quad (p,j,i)$

   nous obtenons la moyenne de V_3 sur une configuration à 3 électrons $\langle V_3\rangle_3$
$$\langle V_3\rangle_3 = \frac{1}{6g_3}\sum_{i,j,p}(\langle\psi|f|ijp\rangle+\langle\psi|f|jpi\rangle+\langle\psi|f|pij\rangle-\langle\psi|f|jip\rangle-\langle\psi|f|ipj\rangle-\langle\psi|f|pji\rangle) = -\frac{\langle\xi\rangle^3}{16}\frac{l+1}{4l+1}, \tag{21}$$

[1] Démontrable en 2nd quantification.

où $\langle\psi| \equiv \langle ijp|$.

En outre, avec le théorème d'Uylings et $g_3 = \binom{4l+2}{3}$,

$$\langle V_3 \rangle_N = -\frac{\langle\xi\rangle^3}{16}\frac{l+1}{4l+1}\frac{N(N-1)(N-2)}{6}. \tag{22}$$

3. Enfin, ensemble avec $\langle V_1\rangle$ et $\langle V_2\rangle$ calculables de la même façon, nous avons

$$\left\langle V_{SO}^3 \right\rangle_N = -\langle\xi\rangle^3 \frac{(1+l)(1+2l-N)(2+4l-N)N}{16(1+4l)}. \tag{23}$$

Comparaison des expressions analytiques avec le code Cowan

Les expressions analytiques des moyennes $\mu_n(V_{\rm so})_a$ sont comparées aux résultats numériques du code Cowan, fournis par J.-C. Pain et F. Gilleron. Le code Cowan est un code semi-relativiste, doté d'une option d'annuler le terme Coulombien de l'Hamiltonien perturbatif pour étudier l'effet spin-orbite de façon séparée.

Pour exemples, nous prenons 2 configurations de l'ion d'or (Au,$Z = 79$) :

- $3d^6$ de l'ion Au^{55+}, soit une sous-couche composée de 6 électrons équivalents;
- $3p^2 3d^6$ de l'ion Au^{59+}, deux sous-couches électroniques distinctes.

Dans le cas de la configuration $3d^6$, d'après Cowan, l'intégral spin-orbite $\langle\xi\rangle_{3d}(Au^{55+}) = 39,865$ eV, et les résultats analytique et numérique des moments d'énergies perturbatives – $\mu_n(V_{\rm so})$ et $\mu_n(V_{\rm ee}, V_{\rm so})$ pour $n = 2,3,4$ – sont récapitulés dans la Table 3. Focalisons sur cette table, nous notons

- en comparant les 2 premières lignes $\mu_n(V_{\rm so})_a \leftrightarrow \mu_n(V_{\rm so})_C$, qu'il y a un bon accord entre les résultats à l'issue des expressions analytiques et les valeurs numériques de Cowan;
- à la 3ème ligne sur $\mu_n(V_{\rm ee}, V_{\rm so})_a$: $\mu_2(V_{\rm ee}, V_{\rm so})_a$ est basée sur la formule de variance publiée dans la Table 3.2 du livre des Bauche et de Peyrusse (2015), $\mu_3(V_{\rm ee}, V_{\rm so})_a$ provient d'une formule publiée par Kucĉas et Karazija (1993) que nous avons vérifié en utilisant les techniques de seconde quantification et d'algèbre angulaire, et qu'il n'y a pas de formules analytiques disponibles lorsque $n > 3$;
- à la colonne $n = 3$, en comparant $\mu_3(V_{\rm so}) \leftrightarrow \mu_3(V_{\rm ee}, V_{\rm so})$, nous en déduisons que l'effet $V_{\rm ee}$ contribue plus à la dissymétrie de la structure d'énergie que l'effet $V_{\rm so}$.

n	2	3	4
$\mu_n(V_{\rm so})_a$	6356,87	3,168(4)	1,110(8)
$\mu_n(V_{\rm so})_C$	6357	3,168(4)	1,11(8)
$\mu_n(V_{\rm ee}, V_{\rm so})_a$	6691.6	8111	X
$\mu_n(V_{\rm ee}, V_{\rm so})_C$	6692	8111	1,195(8)

Table 3: Comparaison des résultats analytique et numérique des moments d'énergies perturbatives dans la configuration $3d^6$ de l'ion Au^{55+}. Les indexes a =analytique, C =Cowan.

Dans le cas de $3p^2 3d^6$, nous pouvons étudier les *cumulants* κ_n, qui sont adéquats pour des phénomènes statistiquement indépendants en raison de leur propriété d'additivité. Un cumulant est relié au moment par relation de récurrence

$$\kappa_n = \mu_n - \sum_{m=1}^{n-1} \binom{n-1}{m-1} \kappa_m \mu_{n-m}. \tag{24}$$

D'après Cowan, $\langle \xi \rangle_{3p}(\mathrm{Au}^{59+}) = 326,842$ eV, $\langle \xi \rangle_{3d}(\mathrm{Au}^{59+}) = 42,261$ eV. En constatant la Table 4, outre que le bon accord confirmé entre résultats analytique et numérique $\kappa_n(V_{\mathrm{so}})_a \leftrightarrow \kappa_n(V_{\mathrm{so}})_C$, les 3 premières lignes permettent de vérifier l'additivité des cumulants des deux sous-couches indépendantes en terme d'énergie spin-orbite $\kappa_n(3p^2) + \kappa_n(3d^6) = \kappa_n(V_{\mathrm{so}})$. Remarquons que l'additivité ne sera plus vérifiée si nous considérons l'effet Coulombien qui implique les paires de sous-couches distinctes.

n	2	3	4
$\kappa_n(3p^2)_a$	8,546(4)	-6,983(6)	-4,793(9)
$\kappa_n(3d^6)_a$	7,144(3)	3,774(4)	-1,287(7)
$\kappa_n(V_{\mathrm{so}})_a$	9,260(4)	-6,945(6)	-4,806(9)
$\kappa_n(V_{\mathrm{so}})_C$	9,26(4)	-6,945(6)	-4.804(9)

Table 4: Comparaison des résultats analytique et numérique des cumulants d'énergies spin-orbite dans la configuration $3p^2 3d^6$ de l'ion Au^{59+}.

En plus d'intérêt méthodologique et fondamental, les méthodes des moyennes pourraient servir aux futures études des UTAs de transitions M_1 intra-configurationnelles évoquées dans la section précédente.

0.4 Conclusion

Résumé

Dans le cadre de la spectroscopie statistique, deux études ont été menées durant cette thèse.

- Modélisation des spectres M_1 des plasmas de tungstène, en utilisant les codes comme FAC et FLYCHK et par implémentation d'un post-processeur. Bien que l'option UTA du code FAC reproduise la majorité d'émissivité des structures spectrales, les formules analytiques du modèle UTA restent à compléter dans le cas des transitions M_1.
- Calcul analytique des moments d'énergies spin-orbite en utilisant les méthodes de calcul de moyennes, une formule de la littérature a été corrigée.

Cette synthèse a pour but d'être résolument pédagogique, les lecteurs intéressés sont invités à lire nos 2 articles dans lesquels plus de cas d'études sont présentés pour la partie de la modélisation des spectres M_1 des plasmas de tungstène, et le problème de convergence de distribution Gram-Charlier est discutée pour la partie des moments d'ordre élevé d'énergies spin-orbite.

Perspectives

Concernant les perspectives, on pourra envisager sur le plan théorique

- étudier les transitions M_1 intra- et inter-configurationnelles manquantes,
- approfondir l'étude des UTA, par exemple, examiner les propriétés des faisceaux, l'effet des différentes fonctions de distribution;

et sur le plan numérique

- mener à brève échéance un calcul de spectre UTA dans le tungstène hors ETL (sans utiliser de théorie de température effective);
- implémenter d'autres modèles statistiques dans le code, par exemple les modèles STA et mixtes;
- paralléliser le code FAC, par exemple par ion ou par configuration.

Part II

English version

Chapter 1

Introduction

> The journey of a thousand miles begins with a single step.
>
> Lao Tzu

Plasma state

Besides the states of solid, liquid and gas, plasma is often referred to as the 4th state of matter, in which probably up to 99% of the matter exists naturally in the universe [1] At first sight, plasma is similar to an ionized gaseous mixture of charged and neutral particles whose dynamics are dominated by electromagnetic forces. Hence the term *plasma* was first used to describe the ionized regions in gas discharges by I. Langmuir in the 1920's. While stars and interstellar space provide examples of plasmas, the Earth and its lower atmosphere form an exception of the 1% plasma-free oasis. On the Earth, aurora borealis and lightning storms are natural phenomena generating plasmas on one hand. On the other hand, the laboratory plasmas constitute a large-scale research subject involving various domains of applications, such as in the investigation of beta cepheid pulsation and convection limit in star interiors, for resolving the problem of plasma heating and confinement in controlled thermonuclear fusion devices, etc. Examples of plasmas belonging to different temperature and density regimes are gathered and shown on Fig. 1.1, see also [W2][B1]. Densities vary roughly over 30 orders of magnitude from 10^5 to 10^{35} electrons per m^3, and temperatures over 7 orders from 10^2 to 10^9 K.

Despite the extremely wide range of temperatures and densities covered by the plasma state, one notable feature concerning the nature of the plasma is its ability to maintain a state of *quasi-neutrality*

$$n_e = Z \times n_i \tag{1.1}$$

where Z is the mean ionization charge of the plasma, n_e stands for electronic density and n_i ionic density. In response to a potential charge imbalance, say resulting from introduction of an electric field or from local concentrations of positive and negative charges generated by charge motions, a phenomenon called *Debye shielding* sets up providing that the external influence is

[1] According to Empedocles, fire was the plasma-representative element which together with earth, water and air made up the elements of Greek cosmology [B1].

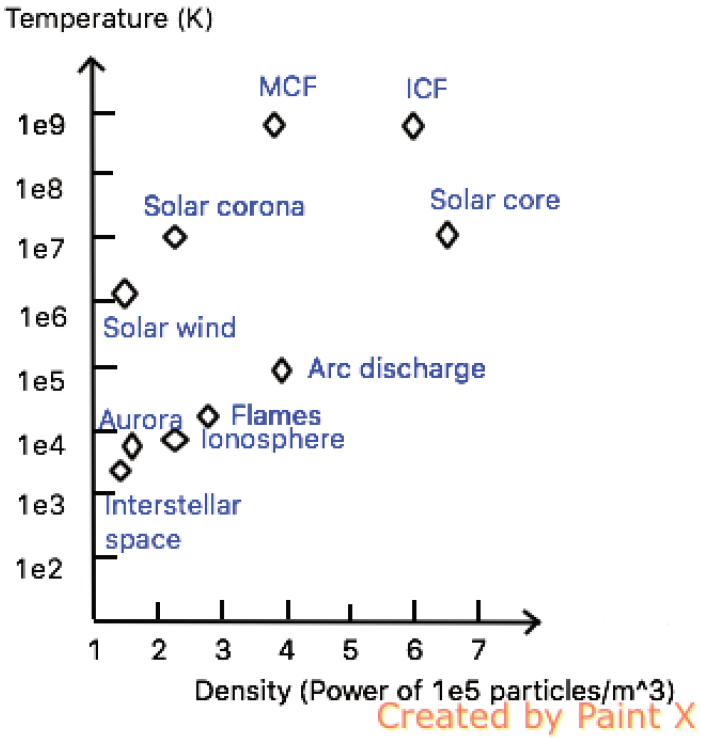

Figure 1.1: Plasmas in temperature-density diagram.1e5 stands for 10^5, MCF for Magnetic Confinement Fusion, ICF Inertial Confinement Fusion. The density scale on the horizontal axis is represented as powers of 10^5, for instance 3 means $(10^5)^3 = 10^{15}$ particles per m^3.

restricted within a finite range. Beyond the *Debye length* [B1],

$$\lambda_D = \sqrt{\frac{\epsilon_0 k_B T_e}{n_e e^2}}, \quad \lambda_D(\mathrm{m}) = 7.43 \times 10^3 \sqrt{\frac{T_e(\mathrm{eV})}{n_e(\mathrm{m}^{-3})}} \tag{1.2}$$

where 1eV $\approx$ 11604K, the plasma remains effectively neutral. Actually, in the presence of strong electrostatic fields, elements of plasma are related even at large distances by the long-ranged Coulomb force and can exhibit collective behaviour such as *plasma oscillations* when re-establishing neutrality, with electrons and ions oscillating respectively at the frequencies

$$\omega_{pe} = \frac{\sqrt{k_B T_e / m_e}}{\lambda_D} = \sqrt{\frac{n_e e^2}{m_e \epsilon_0}}, \quad \omega_{pe}(s^{-1}) = 56.4\sqrt{n_e} \tag{1.3a}$$

$$\omega_{pi} = \sqrt{\frac{n_i (Ze)^2}{m_i \epsilon_0}}, \quad \omega_{pi}(s^{-1}) = 1.32 \times Z \sqrt{\frac{n_i}{A}} \tag{1.3b}$$

where Z denotes the charge state of the plasma and A the atomic number of the ion considered. [B1] For example, a plasma is not transparent to electromagnetic radiation of frequency $\omega < \omega_{pe}$, since the more rapid electron response will neutralize the field and stop its propagation into the plasma.

More quantitatively speaking, to be qualified plasma, an ionized gas must satisfy the following three criteria [B3].

- The Debye length λ_D should be negligible versus the dimension of the system L

  $$\lambda_D \ll L \tag{1.4}$$

  to ensure the quasi-neutrality.

- The number N_D of particles in a "Debye sphere"

  $$N_D = \frac{4\pi}{3} n_e \lambda_D^3, \quad N_D = 1.38 \times \sqrt{T^3(\mathrm{K})/n_e} \gg 1 \tag{1.5}$$

  should be large enough that the collective interactions rule over resultant force on any given particle due to binary collisions.

- The frequency of plasma oscillations ω_{pe} should be higher than the collision rate with neutral atoms. With τ standing for the mean time between collisions, it reads

  $$\omega_{pe} \tau > 1. \tag{1.6}$$

  As a counter-example, if the charged particles collide so frequently with neutral atoms that their motion is dictated by hydrodynamic forces (rather than by electromagnetic ones), it turns out that such gas is too weakly ionized to behave like a plasma.

Depending on density and temperature parameters, the plasma physics can be roughly divided into different regimes :

- In terms of density, low density plasmas correspond to ionic densities $n_i < 10^{17}\text{cm}^{-3}$ [B4] which include plasmas in astrophysics and magnetic confinement devices. Whereas high density regions $n_i > 10^{19}\text{cm}^{-3}$ can be found in inertial confinement plasmas and in star cores.

- In terms of temperature, hot plasmas [O5] may refer to those being nearly fully ionized. Since the degree of ionization α in a plasma, defined as

$$\alpha = \frac{n_i}{n_i + n_a}, \quad (n_a = \text{density of neutral atoms}) \tag{1.7}$$

  is mostly controlled by temperature (rather weakly by density) [W6]. Approximatively, high-temperature plasmas correspond to $T_i \sim T_e \gtrsim 10^7\text{K}$. Whereas low-temperature plasmas (LTP) [O7] can be subdivided into two types: thermal LTP with $T_i \sim T_e \lesssim 2 \times 10^4\text{K}$, and nonthermal LTP with $T_i \sim 300\text{K}$, $T_i \ll T_e \lesssim 10^5\text{K}$, $\alpha = 10^{-6} - 10^{-4}$.

Other parameters have been defined to describe plasma features, such as optically thin or thick, degenerate or non-degenerate, weakly or strongly coupled, etc. When needed, they will be recalled in their respective contexts throughout the manuscript.

Optical atomic spectroscopy

Spectroscopy represents an essential tool to probe the radiative properties of plasmas. Among the various subjects where atomic physics is relevant for plasmas, one may mention three general topics [B4]: the influence of the plasma environment on ionic potential (thus on bound electrons wave functions and energy levels), the study of collisional and radiative processes among electrons and ions inside plasmas and the investigation of emission and absorption spectra of plasmas. This thesis belongs to the 3rd topic and deals with statistical methods applied in the interpretation of emission and absorption spectra with respect to detailed approach.

Concerning the study of emission and absorption in plasmas, a wide literature is available [A8][A9][A10][A11][A12], covering large ranges of atomic elements as well as of plasma (n_e, T_e) regimes. For examples,

- measurement of iron Fe opacity in the Sun for stellar interior energy transport calculations [A13], production of spectroscopic data for the calculation of radiative accelerations in stellar envelopes [A14][A15][A16][A17];

- spectroscopic investigations of tungsten W as tokamak divertor [B18], X opacity measurements in mid Z – like copper Cu, aluminium Al – dense plasmas in order to enhance plasma diagnostics and target design in inertial confinement fusion development [P19].

Detailed and statistical approaches

When the experimental spectra are composed by well-separated lines, the *detailed* approach represents an appropriate tool of interpretation, which is based on line-by-line accounting. Nevertheless, in complex spectra arising from highly ionized plasmas, where atoms are often present in multiple ionization stages with several open subshells, there may be millions of emission or

absorption individual lines which, besides, often gather in coalescent structures.[2] *Statistical* methods are required to identify and analyze essential spectral features in a more efficient way, whose main idea consists in considering *transition arrays* between configurations (cf. Fig.1.2).

Since the first observation of unresolved transition arrays (UTA) in atomic spectroscopy tracing back to the 1940s [A21] and the pioneering analysis by Moszkowski in the 1960s[A22], a special attention has been paid to averaging procedures devoted to the analysis of complex spectra, avoiding the very costly procedure of computing spectra involving thousands of levels and millions of lines in a detailed way. Within the framework of the theory of transition arrays, different statistical models are available. When considering highly charged ions, spin-orbit effect may become dominant and the observed transition arrays connecting pairs of *relativistic* configurations are named Spin-Orbit-Split Arrays (SOSA) [A23]. The averaging procedure has been even more generalized by gathering configurations into super-configurations which leads one to consider super-transition arrays (STA) [A24].

Such statistical description is nowadays included in atomic physics packages such as SCO-RCG [A25] [A26][P27], HULLAC [A28][W29], FAC [A30][O31] which are widely used in atomic spectroscopy. Freely distributed and endowed with a flexible Python interface, the Flexible Atomic Code (FAC) has been used for numerical work in this thesis.

Scope of the manuscript

This manuscript is composed of three chapters and organized as follows.

In chapter 2, general concepts of atomic physics in hot plasmas are introduced. While energy levels and radiative transitions in an isolated atom can be described by quantum mechanics, the computation of emission and absorption spectra requires one to consider the thermodynamic conditions in plasmas.

The chapter 3 is devoted to statistical description of unresolved spectra. The model of UTA is firstly presented, highlighting the use of distribution moments and the choice of distribution function. Then, using the FAC code, numerical construction of transition arrays is made explicit and illustrated by some empirical analysis.

The chapter 4 focuses on moments computations, performed in two cases. On one hand, compact formulas for high-order moments of spin-orbit energies are derived in analytical way, which deal with distribution of degeneracy-weighted *level* energies. On the other hand, magnetic dipole transitions in tungsten plasmas are investigated numerically through distribution moments of *transition* energies weighted by line oscillator force. The two cases respectively echo back to the two articles [A32] [A33] published during the thesis.

[2] A relevant example can be found on Figure 2.2 of the book [B20], which shows the coalescent structures observed in an experimental Lanthanum (Z=57) spectrum of laser-produced plasma. The spectral lines arising from transitions $3d^{N-1}4f \rightarrow 3d^N$ overlap for the consecutive values of N, for instance, in the case of the Cr-like (N=6) ions, the transition array $3d^5 4f \rightarrow 3d^6$ contains 5470 lines.

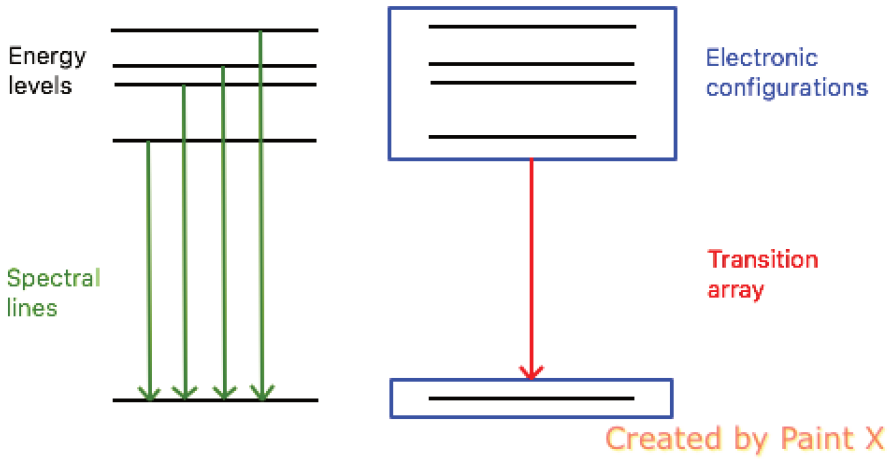

Figure 1.2: Illustration of detailed and statistical descriptions. On the left hand side, a transition between levels $\alpha J \rightarrow \alpha' J'$ gives rise to a spectral line. On the right hand side, a transition between configurations $C \rightarrow C'$ results in a transition array. Two levels or configurations are separated by a hyphen, the first one being lower (resp. higher) in energy in absorption (resp. emission) process.

Chapter 2

Atomic physics in hot plasmas

2.1 N-fermion structure

Regarding quantum behaviour exhibited experimentally on atomic scale, a suitable description of N-electron systems requires mathematical formulations of quantum mechanics, according to which a physical *observable* (eg. energy, position, angular momentum, etc.) can be represented by an *operator* A and a particle (eg. electron, ion, atom, etc.) by a wave function Ψ. One aspect of the complexity in the many-body problem consists of the indistinguishability of identical particles, which involves the *symmetry* [1] concept. For instance, any exchange of identical particles should not modify the wave function modulus.

Since the introduction of the central field scheme by Slater [A35], a large amount of effort has been made to keep track of the symmetry of the states of N-electron systems in simple and elegant ways. Namely, Condon and Shortley establish matrix building method in N-electron atom study [B36], which consists in evaluating matrix elements of the form

$$\langle \Psi \mid A \mid \Psi' \rangle = \int\int\int \Psi^*(r) A \Psi'(r) d^{3N} r \tag{2.1}$$

Later, using the tensor-operator techniques [A37] [A38], Racah's algebra enables to reduce the difficulties in matrix element calculation by writing down formulae for the direct evaluation of matrix elements for coupled basis functions, which bypasses explicit use of Slater determinantal functions. After extending the tensor-operator techniques applicable to all types of operators and configurations in 1962, Judd developed the second quantization method [B39] – firstly introduced and applied on boson-nature photons in the 30s – for fermion-nature electrons in atomic spectroscopy. Comparing to the 1st quantization calculation which requires notably cumbersome anti-symmetrization of wave functions, the 2nd quantization method corresponds to a different labelling of the state basis together with introduction of creation a^+, annihilation a operators and the vacuum state $|0\rangle$.

Except where explicitly noted, Hartree atomic units (cf. Appendix A) are used throughout this section.

[1] For example, the invariance of translation in time (resp. in space) gives rise to conservation law of energy (resp. linear momentum), and the rotational symmetry of a closed system gives rise to the angular momentum conservation law [B34].

N-electron Hamiltonian H

In the atomic structure study, the general operator A in Eq.(2.1) mostly refers to the hermitian Hamiltonian H of the N-fermion system considered.

H as sum of one- and two-electron Hamiltonians :

$$H = \sum_{i=1}^{N} H(i) + \frac{1}{2} \sum_{\substack{i,j=1 \\ i \neq j}}^{N} \frac{1}{r_{ij}}, \tag{2.2}$$

where H denotes either the Schrödinger Hamiltonian, known as nonrelativistic model, or the relativistic Dirac Hamiltonian. The difference between Schrödinger and Dirac approaches departs from the one-electron Hamiltonians $H(i)$. Omitting quantum electrodynamic effects,

$$H(i) = \begin{cases} H^S(i) = H_{\text{elec-nucl}}(i) + H_{\text{kinet}}(i) + H_{\text{spin-orb}}(i) = -\dfrac{Z}{r_i} - \dfrac{1}{2}\nabla_i^2 + \xi(r_i) l_i s_i \\ H^D(i) = -\dfrac{Z}{r_i} + c\alpha(i) \cdot p_i + \beta(i) mc^2 \end{cases} \tag{2.3}$$

with Z denoting the nuclear charge, r_i the radial coordinates, ξ_i the spin-orbit parameter, cf. Eq. (2.34c), c the light velocity, $\alpha(i), \beta(i)$ the 4x4 Dirac matrices for the ith-electron and p_i its 3-momentum. The Schrödinger Hamiltonian for the ith-electron is constituted by 3 components [B40], whereas the kinetic and spin-orbit effects are not considered separately in the Dirac Hamiltonian [B41]. Accordingly, in the 2nd quantization formalism, H can be expressed as sum of one- and two-electron operators F, G [B20], which correspond respectively to the one-electron Hamiltonians $H(i)$ and the Coulomb interaction $\frac{1}{r_{ij}}$ between pairs of electrons of the Eq.(2.2),

$$F = \sum_{i=1}^{N} f_i \equiv \sum_{\epsilon,\phi} \langle \epsilon \mid f \mid \phi \rangle \, a_\epsilon^+ a_\phi, \tag{2.4a}$$

$$G = \sum_{i<j=1}^{N} g_{ij} \equiv \frac{1}{2} \sum_{\alpha\beta\epsilon\eta} \langle \alpha\beta \mid g_{12} \mid \epsilon\eta \rangle \, a_\alpha^+ a_\beta^+ a_\eta a_\epsilon. \tag{2.4b}$$

More details about the formalism will be given later, see for example Eq.(2.21).

Because of the mutual electrostatic repulsion $1/r_{ij}$ on the r.h.s in Eq.(2.2), only the $N = 1$ cases – i.e. for hydrogen atom and H-like ions – can be fully solved in analytical way, with the symmetry of the central Coulomb potential $1/r$ enabling the separation of radial and angular solutions. In order to circumvent the inter-dependence problems in the calculations of N-electron structures, the starting point for most resolution methods in nonrelativistic quantum mechanics as well as in relativistic atomic model is to define an averaged effective potential $U(r)$ following the H-like independent particle central field scheme. In such a way, the state of each electron in a N-electron system is governed by a mean potential $U(r)$ on one hand, and the residual electronic correlations of the other (N-1) electrons on the other hand. In other words, the N-electron system Hamiltonian defined in Eq.(2.2) is partitioned in a new way.

H involving separable mean field $U(r)$:

$$H = H_0 + H^{'}. \tag{2.5}$$

The central term H_0 is invariant with respect to rotation of the frame of reference

$$H_0 = \sum_{i=1}^{N} (t_i + U(r_i)) \tag{2.6}$$

with

$$t_i = \begin{cases} -\frac{1}{2}\nabla_i^2 & \text{in the non-relativistic scheme,} \\ c\alpha(i)\cdot p_i + \beta(i)mc^2 & \text{in the relativistic scheme.} \end{cases} \tag{2.7}$$

and $U(r)$ fulfilling the following boundary conditions [B41]

$$U(r) = \begin{cases} -\frac{Z}{r} + \text{const.} & r \to 0 \\ -\frac{(Z-N+1)}{r}, & r \to \infty \end{cases} \tag{2.8}$$

The residual term $H^{'}$

$$H^{'} = \sum_{i=1}^{N} \left(-\frac{Z}{r_i} - U(r_i) \right) + H_1 + H_2 + ... \tag{2.9}$$

may regroup various correlation effects H_1, H_2, etc. See eg. Eq.(2.39). In the central-field model, operators H_0 and $H^{'}$ are defined according to the 2nd quantization formalism by [B42] :

$$H_0 = \sum_i E_i a_i^+ a_i = \sum_i \langle i|H(i)|i\rangle\, a_i^+ a_i \tag{2.10}$$

$$H^{'} = \frac{1}{2} \sum_{i,j,k,l} g_{ijkl} a_i^+ a_j^+ a_l a_k - \sum_{ik} U_{ik} a_i^+ a_k \tag{2.11}$$

where E_i is the eigenvalue of the one-electron Hamiltonian (See Eq. (2.12))– Schrödinger or Dirac one – in the potential $U(r_i)$,g_{ijkl} is a 2-electron matrix of the Coulomb potential $1/r_{12}$ evaluated with Schrödinger or Dirac orbitals, U_{ik} is the one-electron integral of the central potential U such as $U_{ik} = \int d^3r \psi_i^+(r) U(r) \psi_k(r)$.

Up to now, the introduction of the central field $U(r)$ only leads to a different partition of the system Hamiltonian. However, when neglecting $H^{'}$ in Eq.(2.5), an *approximation* is made for the resolution of the N-electron problem.

2.1.1 Central field approximation

By analogy with the hydrogen case, the central field approximation may consist of two following points :

- since $H \approx H_0$, particle inter-dependence problem of N-electron systems is solved ;
- the central potential $U(r)$ used in H_0 is assumed to be spherically symmetric, so that radial and spin-angular variables of a N-electron wave function are separable.

Finding the most accurate form of $U(r)$ is an uneasy issue and out of the scope of this thesis. Only a succinct summary of approximation methods will be given in Sec.2.1.2.

One-electron central field orbitals

Assuming a suitably defined $U(r)$, a complete set of central field orbitals ψ_i can be generated as eigenfunctions of one-electron (N=1) stationary equation

$$H_0\psi_i(\zeta) = E_i\psi_i(\zeta), \tag{2.12}$$

where the subscript i stands for a quantum state characterized by an ordered but non uniquely defined set of quantum numbers, ζ an electron identified by its spherical coordinates and spin variable (r,θ,ϕ,σ), and H_0 is whether Schrödinger or Dirac Hamiltonian (cf.Eqs.(2.6)(2.7)) for one electron, i.e. $H_0 = t + U(r)$.

In the nonrelativistic model, a one-electron central field orbital $\psi_i(\zeta) = \psi_{nlm_lm_s}(r,\theta,\phi,\sigma)$ is named *spin-orbital* and has the form [B40]

$$\psi_{nlm_lm_s}(r,\theta,\phi,\sigma) = \frac{1}{r}P_{nl}(r)\cdot Y^{(l)}_{m_l}(\theta,\phi)\cdot\chi^{(s)}_{m_s}(\sigma). \tag{2.13}$$

where $R_{nl}(r) = P_{nl}(r)/r, Y^{(l)}_{m_l}(\theta,\phi)$ and $\chi^{(s)}_{m_s}(\sigma)$ are its respectively radial, angular, spin parts.

In the relativistic model, a *spinor* $\psi_i(\zeta) = \psi_{n\kappa m}(r,\theta,\phi,\sigma)$ is characterized by the quantum number set $(n\kappa m \equiv m_j)$ or equivalently $(nljm_j)$ and reads [B41]

$$\psi_{n\kappa m}(r,\theta,\phi,\sigma) = \frac{1}{r}\begin{bmatrix} P_{n\kappa(r)} & \chi_{\kappa m}(\theta,\phi) \\ iQ_{n\kappa(r)} & \chi_{-\kappa m}(\theta,\phi)\end{bmatrix} \tag{2.14}$$

where $P_{n\kappa(r)}, Q_{n\kappa(r)}$ are purely radial amplitudes, and κ is related to l, j as

$$\kappa = \begin{cases} -l-1 & \text{if } j = l+1/2, \\ l & \text{if } j = l-1/2. \end{cases} \tag{2.15}$$

The angular dependent spin-orbit function $\chi_{\kappa m}(\theta,\phi)$ is given by

$$\chi_{\kappa m}(\theta,\phi) = \sum_{\sigma=\mp 1/2} Y^{(l)}_{m-\sigma}(\theta,\phi)\cdot\mu^{\sigma}\cdot\left\langle l\tfrac{1}{2}m-\sigma\sigma|l\tfrac{1}{2}jm\right\rangle \tag{2.16}$$

where μ^{σ} is a spin eigenvector, $Y^{(l)}_{m-\sigma}(\theta,\phi)$ a spherical harmonic and $\left\langle l\frac{1}{2}m-\sigma\sigma|l\frac{1}{2}jm\right\rangle$ a Clebsch-Gordan coefficient. Clebsch-Gordan coefficients as well as relations between different quantum numbers are presented in Appendix B.

One-electron state $|i\rangle$ in the second quantization is represented by the creation operator a_i^+ operating on the vacuum state $|0\rangle$

$$|i\rangle = a_i^+|0\rangle, \tag{2.17a}$$

whose adjoint is defined through the annihilation operator a_k such as

$$\langle i| = \langle 0|a_i. \tag{2.17b}$$

Furthermore, as a rule,

$$\langle 0|a_k^+ = 0, \quad a_k|0\rangle = 0, \quad \langle i|a_k^+ = \delta_{ik}\langle 0|, \quad a_k|i\rangle = \delta_{ik}|0\rangle. \tag{2.17c}$$

N-electron wave functions

Based on fundamental postulate of quantum mechanics, a N-electron (N>1) wave function Ψ should exhibit *anti-symmetric* characteristics upon interchange of any two electrons, the *Pauli exclusion principle* states that two electrons can not occupy the same spin-orbital. More precisely, it means that :

1. for an arbitrary N-electron product state $\Psi(\zeta_1,...,\zeta_N)=\sum_i C(k_1,...,k_N)\cdot\psi_{k_1}(\zeta_1)...\psi_{k_N}(\zeta_N)$, the coefficients $C(k_1,...,k_N)$ must be anti-symmetric under the exchange $k_i \leftrightarrow k_j$ as $\Psi(\zeta_1,...,\zeta_N)$ is anti-symmetric under an arbitrary exchange $i \leftrightarrow j$;

2. $\Psi \equiv 0$ if any two spin-orbitals (or spinors) are identical, for instance $(n_i l_i m_{l_i} m_{s_i})=(n_j l_j m_{l_j} m_{s_j})$, or two electrons have the same coordinates $\zeta_i=\zeta_j$.

In the central field model, a typical wave function describing a N-electron system is made up of appropriate linear combinations of one-electron orbitals products

$$\Psi=\frac{1}{\sqrt{N!}}\sum_{\sigma(P)}(-1)^{\epsilon(P)}\psi_{\sigma(1)}(\zeta_1)...\psi_{\sigma(N)}(\zeta_N), \tag{2.18}$$

where anti-symmetrization of the wave function is carried out by the sum running over all possible electron permutations $\sigma(P)$, with the permutation signature, labelled $\epsilon(P)$, representing the *parity* of the permutation [2],

$$\epsilon(P)=\begin{cases}1, & \text{if even permutation,}\\ -1, & \text{if odd permutation.}\end{cases} \tag{2.19}$$

The anti-symmetric properties together with Pauli's exclusion principle are more easily taken into account by building N-electron wave functions with *Slater determinant*. A N-electron determinantal function writes as

$$\Psi(\zeta_1,...,\zeta_N)=\frac{1}{\sqrt{N!}}\begin{vmatrix}\psi_1(\zeta_1) & \psi_1(\zeta_2) & ... & \psi_1(\zeta_N)\\ \psi_2(\zeta_1) & \psi_2(\zeta_2) & ... & \psi_2(\zeta_N)\\ ... & & & \\ \psi_N(\zeta_1) & \psi_N(\zeta_2) & ... & \psi_N(\zeta_N)\end{vmatrix} \tag{2.20}$$

where $\psi_i(\zeta_i)$ can be either spin-orbital or spinor, $\psi_i(\zeta_j)=\langle\zeta_j|i\rangle$. One can notice that the determinant vanishes if two rows are identical (i.e. two spin-orbitals are identical) or two columns are identical (i.e. two electrons have the same coordinates). The anti-symmetrization is automatically ensured, since the summation over permutations is implicitly accounted for through interchanges of rows and columns.

In the 2nd quantization formalism, a normalized N-electron determinantal state $|\alpha\beta...\nu\rangle$, is regarded as a sequence of operators $a_\alpha^+, a_\beta^+...$ acting on a vacuum state $|0\rangle$

$$|\alpha\beta...\nu\rangle \equiv a_\alpha^+ a_\beta^+ ... a_\nu^+ |0\rangle \tag{2.21}$$

where each Greek symbol stands for a quantum-number set, eg. $(nlm_l m_s)$. $|\alpha\beta...\nu\rangle$ is anti-symmetric under permutation of one-electron quantum numbers, whose ordering is indicated by

[2] For example, in the case of 3 electrons (i,j,p), the circular permutations $\{(i,j,p);\quad (j,p,i);\quad (p,i,j)\}$ correspond to $\epsilon(P)=+1$, and the exchange permutations $\{(j,i,p);\quad (i,p,j);\quad (p,j,i)\}$ are odd.

the sign of the wave function. Furthermore, Pauli exclusion principle stems automatically from the anti-commutation relations [3] between operators [B34] :

$$\{a_\alpha, a_\beta^+\} \equiv a_\alpha a_\beta^+ + a_\beta^+ a_\alpha = \delta_{\alpha\beta}, \tag{2.23a}$$

$$\{a_\alpha^+, a_\beta^+\} \equiv a_\alpha^+ a_\beta^+ + a_\beta^+ a_\alpha^+ = 0, \tag{2.23b}$$

$$\{a_\alpha, a_\beta\} \equiv a_\alpha a_\beta + a_\beta a_\alpha = 0. \tag{2.23c}$$

Indeed, the fundamental idea of the second quantization method is to transfer to operators – a^+, a, etc. the tensorial proprieties characteristic of wave functions.

As example, an anti-symmetrized two-electron state $|\Psi(1,2)\rangle$ can be built out of two one-particle states ψ such as

$$|\Psi(1,2)\rangle = \frac{1}{\sqrt{2}}\begin{vmatrix}\psi_1(\zeta_1) & \psi_1(\zeta_2)\\ \psi_2(\zeta_1) & \psi_2(\zeta_2)\end{vmatrix} = \frac{1}{\sqrt{2}}\left(\psi_1(\zeta_1)\psi_2(\zeta_2) - \psi_1(\zeta_2)\psi_2(\zeta_1)\right) = a_1^+ a_2^+ |0\rangle. \tag{2.24}$$

Electron configuration

As a consequence of the central field approximation, a *configuration* is defined by means of a list of occupied orbitals in an anti-symmetric N-electron wave function [B41]. The energy of an atom in the central field approximation is independent of the z-projection (magnetic) quantum numbers [4] it means that the energy level is characterized by the quantum numbers (n,l) in nonrelativistic cases,

$$\mathcal{C}_{\rm nr} = (n_1 l_1)^{\nu_1}(n_2 l_2)^{\nu_2}...(n_p l_p)^{\nu_p} \tag{2.25a}$$

and by (n,κ) or equivalently (n,l,j) in relativistic cases,

$$\mathcal{C}_{\rm r} = (n_1 l_1 j_1)^{\omega_1}(n_2 l_2 j_2)^{\omega_2}...(n_q l_q j_q)^{\omega_q} \tag{2.25b}$$

where the orbitals sharing the same values of (n,l) or (n,l,j) are identical and form respectively a nonrelativistic (nr) or a relativistic (r) *subshell*. The ν_i or ω_i – called the *occupation numbers* – electrons are said to be *equivalent*, with

$$\sum_{i=1}^{p}\nu_p = \sum_{i=1}^{q}\omega_q = N. \tag{2.25c}$$

Given the equivalence, nr- as well as r-configurations are usually specified by the occupation numbers ν_i or ω_i of each subshell i, which give rise to *spectroscopic labels*.

[3] By the way, the orthonormality of one-electron states $\langle\psi_{nlm_l m_s}|\psi_{n'l'm'_l m'_s}\rangle = \delta_{nn'}\delta_{ll'}\delta_{m_l m'_l}\delta_{m_s m'_s}$, written in the 2nd quantization formalism,

$$\langle\alpha|\beta\rangle = \langle 0|a_\alpha a_\beta^+|0\rangle = \int \alpha^*\beta d\tau = \delta_{\alpha\beta} \tag{2.22}$$

can be proved by the relation (2.23a), and the anti-commutation relations in Eqs. (2.23b)(2.23c) ensure the anti-symmetry of the state $|\alpha\beta\rangle$ and its adjoint $\langle\alpha\beta|$ respectively [B42].

[4] For a pure Coulomb field, there exists additional (hydrogenic) degeneracy: the energy of such atom does not depend on the orbital quantum number l.

n-value	shell	l-value	nr-subshell	j-value	r-subshell	full shell composition
1	K	0	s	0	s	$(1s)$
2	L	1	p	$\frac{1}{2},\frac{3}{2}$	p_-,p_+	$(2s+2p)$
3	M	2	d	$\frac{3}{2},\frac{5}{2}$	d_-,d_+	$(3s+3p+3d)$
4	N	3	f	$\frac{5}{2},\frac{7}{2}$	f_-,f_+	$(4s+4p+4d+4f)$
5	O	4	g	$\frac{7}{2},\frac{9}{2}$	g_-,g_+	$(5s+5p+5d+5f+5g)$
6	P	5	h	$\frac{9}{2},\frac{11}{2}$	h_-,h_+	$(6s+6p+6d+6f+6g+6h)$

Table 2.1: Spectroscopic labels illustrated for the first 6 shells. Non-relativistic and relativistic subshells are respectively denoted by nr-subshell and r-subshell. For a given l-value (except $l=0$), a nr-subshell corresponds to two r-subshells, characterized by $j_-=|l-1/2|, j_+=|l+1/2|$ and denoted respectively by the subscripts $-,+$. For example, a full L-shell includes subshells of types $(2s+2p)$ or $(2s+2p_-+2p_+)$ depending on whether non-relativistic or relativistic model is considered.

Due to the Pauli exclusion principle, the occupation numbers ν_i,ω_i of each subshell i is limited to a maximum, defined by

$$\begin{cases} \nu_i^{max} = 2(2l_i+1) & \text{for a nr-subshell} \\ \omega_i^{max} = 2j_i+1 & \text{for a r-subshell,} \end{cases} \tag{2.26}$$

with $\nu_i^{max} \leq 2n^2$ and $\omega_i^{max} \leq 2n^2$, where $2n^2$ is the maximum number of electrons occupying the same n-shell. A fully occupied subshell is qualified *closed* whereas a *open* subshell is a partially filled one. Closed subshells in a configuration are of practical interest, since the state of a closed subshell must be invariant under axis rotation, only one Slater determinant exists corresponding to a total angular momentum $J=0$ and degeneracy $g=1$, cf. Eq.(2.28). Therefore, a closed subshell is often omitted in the spectroscopic label of a configuration, eg. $1s^22s^22p^63s3p^4$ is usually denoted by $3s3p^4$.

For an arbitrary subshell $(n_il_i)^{\nu_i}$ or $(n_il_ij_i)^{\omega_i}$, the *degeneracy* [5] or statistical weight g_i is equal to

$$g_{i,\text{nr}} = \binom{\nu_i^{max}}{\nu_i}, \quad g_{i,\text{r}} = \binom{\omega_i^{max}}{\omega_i}. \tag{2.28}$$

The configurational degeneracies of (2.25a)(2.25b) can be deduced from subshell ones by product,

$$g = \prod_{i=1}^{p} g_{i,\text{nr}} = \prod_{i=1}^{q} g_{i,\text{r}}. \tag{2.29}$$

Taking the example of $3s3p^4$, two subshells $-s(l=0), p(l=1)$ with respectively one and 4 electrons. Applying Eqs. (2.28)(2.29), the configurational degeneracy is derived as

$$g_{\text{nr}}(3s3p^4) = \binom{2}{1}\binom{6}{4} = 2\times 15 = 30 \tag{2.30}$$

[5] The degeneracy of a subshell g_i corresponds to the number of micro-states it covers such as

$$\begin{aligned} &\{(m_s\sigma_s)\} \in \mathcal{C}_{\text{nr}} \text{ with } 1\leq s\leq \nu_i, 1\leq \alpha \leq g_{i,\text{nr}} \\ &\{(l_sj_sm_s)\} \in \mathcal{C}_{\text{r}} \text{ with } 1\leq s\leq \omega_i, 1\leq \alpha \leq g_{i,\text{r}}. \end{aligned} \tag{2.27}$$

in nonrelativistic consideration. In relativistic model, $p^4 = p_-^{\omega_-} p_+^{\omega_+}$ with $\omega_- + \omega_+ = 4$. Since $\omega^{max}(j_- = \frac{1}{2}) = 2$ and $\omega^{max}(j_+ = \frac{3}{2}) = 4$, $\omega_- = \{0,1,2\}$ and $\omega_+ = \{0,1,2,3,4\}$. The different population repartitions involved give rise to 3 possible relativistic configurations, each with its degeneracy written as

$$g(p_+^4) = \binom{2\cdot\frac{3}{2}+1}{4} = 1 \tag{2.31a}$$

$$g(p_- p_+^3) = \binom{2\cdot\frac{1}{2}+1}{1} \cdot \binom{2\cdot\frac{3}{2}+1}{3} = 8 \tag{2.31b}$$

$$g(p_-^2 p_+^2) = \binom{2\cdot\frac{1}{2}+1}{2} \cdot \binom{2\cdot\frac{3}{2}+1}{2} = 6 \tag{2.31c}$$

and the total statistical weight

$$g_{\mathrm{r}}(3s3p^4) = 2 \times (1+8+6) = 30 \tag{2.31d}$$

is equal to the result in nonrelativistic model, as expected.

2.1.2 Configuration structure

Empirical energy ordering

As seen in Table 2.1, spectroscopic notation of a configuration is closely related to angular momentum quantum numbers. Qualitatively speaking, atomic energy levels in a energy-level diagram can be roughly estimated as classified according to their angular momenta [B40]. In general, the energy ordering of neutral atoms in their ground state follow the $n+l$ *rule* [W43], which states that orbitals with a lower $n+l$ value are filled before those with higher $n+l$ ones, cf. the Fig.2.1. However, when highly charged ions are considered, the ordering of energies is

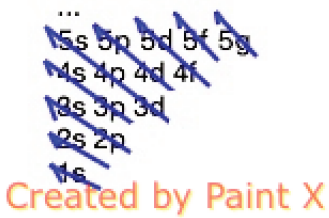

Figure 2.1: Scheme of the $n+l$ rule in orbital filling. The energies of subshells (nl) increase following the direction of arrows from the bottom right to the top left.

firstly defined by the increasing principal quantum number n, then by the increasing orbital quantum number l. The comparison of energy orderings between $3d$ and $4s$ orbitals is carried out through two alkali elements – neutral potassium K (Z=19) and highly ionized caesium Cs^{36+} (Z=55), based on the on-line computation of NIST atomic database [W44]. The output values are gathered in the Table 2.2. While the configuration $3p^6 3d$ lies higher than $3p^6 4s$ in energy-level diagram of neutral K, crossover between $3d$ and $4s$ orbitals is observed in highly charged Cs^{36+} ions.

	K (Z=19), K I	Cs^{36+} (Z=55), Cs XXXVII
E($3p^6 4s,^2S$) (eV)	0	980.68
E($3p^6 3d,^2D$) (eV)	2.66996 (5/2)	18.41 (5/2)
	2.67025 (3/2)	0 (3/2)

Table 2.2: Illustration of energy ordering in neutral atom and highly charged ion. Levels energies are output values from NIST atomic database. Two alkali elements of the Mendeleev's table – potassium K (Z=19) and caesium Cs (Z=55) are considered, with the first neutral and the second highly ionized, so that both configurations are composed by 19 electrons. Crossover between $3d$ and $4s$ orbitals occurs in Cs^{36+} ions.

Single configuration basis

A more rigorous treatment of energy level structures was provided by the Slater-Condon theory, namely through matrix method as briefly mentioned in Eq.(2.1). For instance, the energy of spherically averaged atom reads [B40]

$$E = \frac{\sum_\Psi \langle \Psi | H | \Psi \rangle}{\text{number of basis functions}}. \tag{2.32}$$

The basic procedure of the matrix method consists in expanding the unknown wave function $|\Psi\rangle$ in terms of judiciously truncated basis functions. Setting up an appropriate set of basis functions is crucial in matrix elements evaluation and represents an important difficulty of the method. It has been found out that [B40] one configuration constitutes generally a suitable grouping of nearly-spaced energy levels which set of functions, for instance $\sum_\Psi \in \mathcal{C}$ in Eq.(2.32), can be used as configurational basis functions to evaluate the matrix elements.

In the *single configuration approximation*, the energies of the various states of a field-free atom are given by the eigenvalues of matrices, one matrix for each possible J value [A45]. The matrix elements connecting two states b, b' are in the form

$$H_{bb'} = \delta_{bb'} E_{\text{av}} + \sum_{ijk} \Big[f_k F^k(l_i, l_j) + g_k G^k(l_i, l_j) \Big] + \sum_i d_i \xi_i. \tag{2.33}$$

- The configurational average E_{av} is given by the diagonal matrix elements H_{bb}.
- The parameters F^k, G^k, ξ_i are the Slater integrals arising from the calculation of the radial part of wave functions. Actually, the integrals $R^k(ij,pq)$ appear when evaluating the matrix element $\langle ij|2/r_{12}|pq\rangle$, the direct $F^k(ij)$ and exchange $G^k(ij)$ Slater integrals are particular cases of the integrals $R^k(ij,pq)$ such as $F^k(ij) \equiv R^k(ij,ij), G^k(ij) \equiv R^k(ij,ji)$. Together with the spin-orbit integral $\xi(i)$ [A46], they are related to the radial wave functions $P_{nl}(r)$ as

$$F^k(ij) = \int_0^\infty \int_0^\infty \frac{2r_<^k}{r_>^{k+1}} |P_i(r_1)|^2 |P_j(r_2)|^2 dr_1 dr_2, \tag{2.34a}$$

$$G^k(ij) = \int_0^\infty \int_0^\infty \frac{2r_<^k}{r_>^{k+1}} P_i(r_1) P_j(r_1) P_i(r_2) P_j(r_2) dr_1 dr_2, \tag{2.34b}$$

$$\xi(i) = \frac{\alpha^2}{2} \int_0^\infty \frac{1}{r} \frac{dU}{dr} |P_i(r)|^2 dr. \tag{2.34c}$$

- The parameters (f_k, g_k, d_i) are angular coefficients that depend only on the angular quantum numbers of the basis states $b, b^{'}$ in the chosen coupling scheme, say LS- or jj-couplings, they are independent of the atom or ion which exhibits the configuration. Analytical expressions of (f_k, g_k, d_i) can readily be derived using Racah's algebra of *irreducible tensor operators*[6] in terms of three types of *reduced matrix elements*[7],

$$\left\langle l||C^{(k)}||l^{'}\right\rangle \tag{2.37a}$$

$$\left\langle l^n \alpha LS||U^{(k)}||l^n \alpha^{'} L^{'} S^{'}\right\rangle \tag{2.37b}$$

$$\left\langle l^n \alpha LS||V^{(k1)}||l^n \alpha^{'} L^{'} S^{'}\right\rangle \tag{2.37c}$$

  for details, see Eqs. (20)(21)(22) in [A45].

Approximation methods of resolution

The evaluation of matrix elements $H_{bb'}$ requires one to determine $P_{nl}(r)$ of one-electron wavefunction $\psi_i(r)$, cf. Eq.(2.13) and set up a potential $U(r_i)$ in the system Hamiltonian, cf. Eq.(2.6). Two approximation approaches are of great interest, namely the perturbational procedure and self-consistent field method.

Perturbational procedure

The basic idea of the perturbational procedure is to start with the central part H_0 of the system Hamiltonian, cf. Eq.(2.5), and add the perturbative part $H^{'}$ as corrections to H_0 assuming $H^{'} \ll H_0$, cf. Eqs.(2.6)(2.9). The perturbed quantity is approximated by a n-th order power expansion in parameter λ,

$$H\psi = E\psi \text{ with } \begin{cases} H = H_0 + \lambda H^{'} \\ \psi = \psi^{(0)} + \lambda\psi^{(1)} + \lambda^2\psi^{(2)} + ... \\ E = E^{(0)} + \lambda E^{(1)} + \lambda^2 E^{(2)} + ... \end{cases} \tag{2.38}$$

[6] When dealing with evaluating angular portion of matrix calculation, Racah's algebra of irreducible tensor operators turn out to be efficient. An irreducible tensor $T_q^{(k)}$ of k-rank has $2k+1$ components $q = -k, ..., k$, whose commutation relations with the angular momentum operators read

$$\left[j_{\pm}, T_q^{(k)}\right] = \sqrt{(k \mp q)(k \pm q + 1)}\, T_{q\pm1}^{(k)}, \tag{2.35a}$$

$$\left[j_z, T_q^{(k)}\right] = q T_q^{(k)}. \tag{2.35b}$$

For example, a set of spherical functions $C_m^{(l)}$ $(m = -l, -l+1, ...0, ...l-1, l)$ composes an irreducible tensor; the position vector r may be considered as $r^{(1)} = rC^{(1)}$.

[7] It is worth mentioning the Wigner-Eckart theorem

$$\left\langle \alpha jm \mid T_q^{(k)} \mid \alpha' j' m' \right\rangle = C(jm; j'km'q)(\alpha j||T^{(k)}||\alpha' j') \tag{2.36}$$

which enables the separation between geometrical properties and physical nature of the operator. The geometrical properties are linked to k, q and contained in the $3j$ symbol (related to the coupling of angular momenta). The physical nature (in the sense of interaction) is found in the reduced matrix element, independent of the quantum numbers appearing in the $3j$ symbol.

where the 1st-order energy shift is given by $E^{(1)} = \left\langle \psi^{(0)} | H' | \psi^{(0)} \right\rangle$ for instance. When applying on atomic structure, for example with the perturbative terms as

$$H_1 = \frac{1}{2} \sum_{\substack{i,j=1 \\ i \neq j}}^{N} \frac{1}{r_{ij}} \tag{2.39a}$$

$$H_2 = \xi(r_i) l_i s_i \tag{2.39b}$$

in the nonrelativistic scheme, [O47]

- the 0th order Hamiltonian H_0 determines the energy level structure specified by n, l or n, l, j (eg. in a Grotrian diagram) ;
- the Coulomb term H_1 splits the energy levels into different *terms*;
- the spin-orbit term H_2 splits the terms, leading to fine structure of the energy levels;
- other effects (eg. nuclear effect, external field) H_3 may lead to hyperfine structures of the levels, etc.

Variational principle

Among the most commonly used methods, the Hartree-Fock (HF) numerical resolution scheme represents a self-consistent method which optimizes potential $U^{(i)}(r)$ and wave functions $P_{nl}^{(i)}(r)$ through iterative process with i.

For example, in a nonrelativistic single-configuration basis $\mathcal{C}_{\rm nr}$, the Hartree-type wave functions are solutions of a set of p differential equations [B40]

$$\begin{cases} \left(-\dfrac{d^2}{dr^2} + \dfrac{l_1(l_1+1)}{r^2} + U(r) \right) P_1(r) = E_1 P_1(r) \\ \quad \cdots \\ \left(-\dfrac{d^2}{dr^2} + \dfrac{l_i(l_i+1)}{r^2} + U(r) \right) P_i(r) = E_i P_i(r) \\ \quad \cdots \\ \left(-\dfrac{d^2}{dr^2} + \dfrac{l_p(l_p+1)}{r^2} + U(r) \right) P_p(r) = E_p P_p(r) \end{cases} \tag{2.40}$$

where each equation to one of the subshells $(n_i l_i)^{\nu_i}$ composing $\mathcal{C}_{\rm nr}$. At the initial stage, a set of suitably defined "test" wave functions $(P_1^{(1)}(r), ..., P_i^{(1)}(r), ...P_p^{(1)}(r))$ is used to derive the potential $U^{(1)}(r)$. Then, with $U^{(1)}(r)$, $(P_1^{(2)}(r), ..., P_i^{(2)}(r), ...P_p^{(2)}(r))$ can be performed which give in turn the potential $U^{(2)}(r)$, etc. At each iteration j, the optimized $P^{(j)}(r)$ should satisfy two criteria : minimize the calculated energy of the atom, cf. Eq. (2.32) and ensure orthonormalization relation, cf. Eq.(2.22). The procedure repeats until $U^{(n)}(r) = U^{(n-1)}(r)$.

Notice that the presentation of approximation methods above is very simplified, focusing more on general procedures rather than resolution details. A rigorous discussion on the choice and derivation of different potentials in use in various atomic codes would require more advanced knowledge on purely atomic structure. Here, we are content with showing the form of the potential in FAC [A30], the code based on which the numerical work was done in this thesis.

Potential $U(r)$ in FAC

The atomic structure calculation in FAC [A30] is based on the relativistic configuration interaction, see next paragraph, with independent particle basis wave-functions. These basis wave-functions are derived from a local central potential $V(r)$, which is self-consistently determined to represent electronic screening of the nuclear potential.[O31]

The local central potential $V(r)$ includes contributions from the nuclear charge $V^N(r)$ and the electron-electron interaction $V^{ee}(r)$.

- The nuclear contribution part is defined regarding to the statistical model radius R_N of the nucleus such as $R_N = 2.2677 \times 10^{-5} A^{1/3}$ with A the atomic mass,

$$V^N(r) = \begin{cases} \dfrac{Z}{2R_N}\left[3 - \left(\dfrac{r}{R_N}\right)^2\right], & \text{if } r \le R_N, \\ Z/r, \quad \text{elsewhere.} \end{cases} \tag{2.41}$$

- And the expression of $V^{ee}(r)$ is given by

$$V^{ee}(r) = \frac{1}{r\sum_a \omega_a \rho_a(r)} \times \sum_{ab} \omega_a(\omega_b - \delta_{ab}) Y^0_{bb}(r)\rho_a(r) + \sum_a \omega_a(\omega_a - 1)\sum_{k>0} f_k(a,a) Y^k_{aa}(r)\rho_a(r) + \sum_{a\neq b}\sum_k \omega_a\omega_b g_k(a,b) Y^k_{ab}(r)\rho_{ab}(r) \tag{2.42}$$

  where

  - a, b denote two sub-shells $n\kappa, n'\kappa'$, with ω_a, ω_b their occupation numbers ;
  - $\rho_{ab} = P_a(r)P_b(r) + Q_a(r)Q_b(r)$, cf. Eq.(2.14) ;
  - $Y^k_{ab}(r) = r\int \frac{r^k_<}{r^{k+1}_>}\rho_{ab}(r')dr'$, with $r_<$ =min(r, r') and $r_>$ =max(r, r') ;
  - f_k and g_k are respectively the direct and exchange coefficients, defined as a function of the Wigner $3j$ coefficient $\begin{pmatrix} j_1 & j_2 & j_3 \\ m_1 & m_2 & m_3 \end{pmatrix}$, cf. Appendix B,

$$f_k(a,b) = -\left(1 + \frac{1}{2j_a}\right)\begin{pmatrix} j_a & k & j_b \\ -\frac{1}{2} & 0 & \frac{1}{2} \end{pmatrix}^2 \tag{2.43a}$$

$$g_k(a,b) = -\begin{pmatrix} j_a & k & j_b \\ -\frac{1}{2} & 0 & \frac{1}{2} \end{pmatrix} \tag{2.43b}$$

Based on the Dirac-Fock-Slater method [A48], which is the relativistic version of the Hartree-Fock-Slater method, the effective potential used in code FAC is defined as

$$U(r) = V(r) - \frac{\alpha^2}{2}\{[V(r) - \epsilon_a]^2 - W(r)\}, \tag{2.44}$$

where $W(r)$ is a function of $V(r)$, defined in [A30].

Configuration mixing

When accurate calculations are no longer made within the single-configuration approximation, especially in the case of highly excited configurations overlapping each other in energy, it would be necessary to include functions from two or more configurations in the basis set. When each computed wave function $|\Psi\rangle$ results in a mixture of basis functions from several configurations, there is *configuration mixing*.

For example, considering a tractable case of $3d^2$ of a W^{54+} ion, using the code FAC, mixing among the relativistic configurations $\{3d_-^2, 3d_-3d_+, 3d_+^2\}$ is illustrated in Table 2.3. As shown in the last column, three relativistic configuration mixing groups–$(0,3,7)_{J=2}$, $(1,8)_{J=0}$, $(4,6)_{J=4}$ and two configurations without mixing–$2,5$ are identified. Because of J-value conservation, configuration mixing occurs only within configurations with the same J.

Moreover, in the basis (0,3,7,1,8,4,6,2,5), the "block-diagonal" matrix $M = m_{ij}$ reads

$$M = \begin{pmatrix} -0.9975 & -0.0686 & 0.0146 & 0 & 0 & 0 & 0 & 0 & 0 \\ -0.0681 & 0.9972 & 0.0328 & 0 & 0 & 0 & 0 & 0 & 0 \\ 0.0168 & -0.0313 & 0.9937 & 0 & 0 & 0 & 0 & 0 & 0 \\ 0 & 0 & 0 & -0.9945 & -0.1050 & 0 & 0 & 0 & 0 \\ 0 & 0 & 0 & 0.1050 & -0.9945 & 0 & 0 & 0 & 0 \\ 0 & 0 & 0 & 0 & 0 & -0.9927 & 0.1205 & 0 & 0 \\ 0 & 0 & 0 & 0 & 0 & -0.1205 & -0.9927 & 0 & 0 \\ 0 & 0 & 0 & 0 & 0 & 0 & 0 & 1 & 0 \\ 0 & 0 & 0 & 0 & 0 & 0 & 0 & 0 & 1 \end{pmatrix} \tag{2.45}$$

where the non-zero off-diagonal coefficients are mixing coefficients, and inside each configuration mixing group, the matrix is diagonal. The diagonal matrix elements in Eq.(2.45) are near 1, it means the mixing effect is relatively small, a matrix without configuration mixing would be diagonal with matrix elements $m_{ij} = \delta_{ij}$.

2.2 Emission and absorption spectra

Although it is a very good approximation to assume that the atom interacts weakly with the electromagnetic radiation [B40], an atom in an excited level 2 of energy E_2 can be found in a lower-energy level 1 ($E_1 < E_2$) through a *spontaneous emission* of a photon of energy

$$h\nu_{12} = E_2 - E_1, \tag{2.46}$$

which results in a spectrum line at the frequency ν_{12}. Together with the spontaneous emission, the formation of an atomic spectrum occurring in plasmas may arise from other emission or absorption processes, between bound-bound levels as well as between bound-free or free-free ones, cf. Table 2.4. All lines together form a radiative spectrum, whose properties depend on the collective behaviours of the atoms in a plasma.

Thermodynamics – for instance, through the electron density n_e and temperature T_e – are involved in order to account for the distribution of atoms among the various ionization stages and populations of different states on one hand, and line shapes as a result of broadening effects on the other hand. Unless otherwise noted, temperature T stands for energy $T \equiv k_B T$ and is in units of eV.

LS-level	jj-level	Index	Mixing
$^3F_2$	$(3d_-^2)_{J=2}$	0	+3, +7
$^3P_0$	$(3d_-^2)_{J=0}$	1	+8
$^3F_3$	$(3d_-3d_+)_{J=3}$	2	Non
$^3P_2$	$(3d_-3d_+)_{J=2}$	3	+0, +7
$^3F_4$	$(3d_-3d_+)_{J=4}$	4	+6
$^3P_1$	$(3d_-3d_+)_{J=1}$	5	Non
$^1G_4$	$(3d_+^2)_{J=4}$	6	+4
$^1D_2$	$(3d_+^2)_{J=2}$	7	+3, +0
$^1S_0$	$(3d_+^2)_{J=0}$	8	+1

Table 2.3: Configuration structure in the case of $3d^2$ of a W^{54+} ion. - stands for $j = 3/2$, + for $j = 5/2$. The 9 levels from FAC computation, which can be regrouped into 3 relativistic configurations $\{3d_-^2, 3d_-3d_+, 3d_+^2\}$, are indexed through 0 to 8 and sorted in the order of increasing energy, i.e. $E_0 < E_1 < ... < E_8$. One can identify three relativistic configuration mixing groups–$(0,3,7)_{J=2}$, $(1,8)_{J=0}$, $(4,6)_{J=4}$ and two configurations without mixing–2, 5. By the way, comparing energy levels arising from jj- and LS-couplings, one can notice that the Hund's rules are no longer fully respected because of the high atomic number Z of tungsten which leads to strong relativistic effect.

Free-free processes		
bremsstrahlung	$e \longleftrightarrow e + h\nu$	inverse brems
Bound-free processes		
collisional ionization	$(Z,N) + e \longleftrightarrow (Z,N-1) + 2e$	3-body recombination
photoionization	$(Z,N) + h\nu \longleftrightarrow (Z,N-1) + e$	radiative recombination
auto-ionization	$(Z,N)^* \longleftrightarrow (Z,N-1) + e$	dielectronic recombination
Bound-bound processes		
spontaneous (+induced) emission	$(Z,N)^* \longleftrightarrow (Z,N) + h\nu$	photoabsorption

Table 2.4: Chemical pictures of microscopic processes (not exclusive) in detailed balance. According to plasma (n_e, T_e) ranges, electron-atom collisional frequencies and radiative transition probability rates may be in competition with each other, resulting in various ionization as well as recombination processes [B40]. The balance between rates at which these processes take place may be studied by solving rate equations, required when plasmas are out of thermodynamic equilibrium. The symbol * stands for excited state lying above the ionization limit.

2.2.1 Thermodynamic equilibrium

When the rates of various ionization and recombination processes in a plasma are equal, the plasma is said to be in *steady state*, which is a necessary but not sufficient condition to define thermodynamic equilibrium. Under the assumption of thermodynamic equilibrium, the relative ions abundances and the distribution of populations over states can be determined by purely statistical considerations. Indeed, the thermodynamic equilibrium of a plasma may roughly cover 3 types of equilibria – the complete Thermodynamic Equilibrium (TE), the Local Thermodynamic Equilibrium (LTE) and the Partial Local Thermodynamic Equilibrium (PLTE).

Complete thermodynamic equilibrium

In a TE plasma, all 3 types of particles – ions, electrons and photons are in equilibrium, as a result of which the following conditions are satisfied.

- The *detailed balance* is fulfilled, meaning that the rate of each process equals exactly the rate of its inverse [B4].
- The radiation is assimilated to a black-body radiation, i.e. photon energy distribution obeys the Planck's law,
$$B_\nu(\nu,T) = \frac{2h\nu^3}{c^2}\frac{1}{\exp\left(\frac{h\nu}{T}\right)-1} \tag{2.47}$$
which shows the spectral radiance B_ν for the frequency ν at the temperature T.
- Electron and ion velocity and energy distributions follow Maxwell-Boltzmann functions,
$$f_v(v)dv = n_e\left(\frac{m_e}{2\pi T_e}\right)^{3/2} 4\pi v^2 \exp\left(-\frac{m_e v^2}{2T_e}\right)dv \tag{2.48a}$$
$$f_\varepsilon(\varepsilon)d\varepsilon = \frac{2}{\sqrt{\pi}} n_e\left(\frac{\varepsilon}{T_e}\right)^{1/2}\exp\left(-\frac{\varepsilon}{T_e}\right)\frac{d\varepsilon}{T_e} \tag{2.48b}$$
where $f_v(v)dv$ (resp. $f_\varepsilon(\varepsilon)d\varepsilon$) is the density of free electrons whose velocity (resp. kinetic energy) is between v and $v+dv$ (resp. between ε and $\varepsilon+d\varepsilon$). The normalization is done so that the integrals of such distributions are equal to n_e. [8]
- Within one charge state Z, distribution of populations over two levels $(i,j) \in J_Z$ is given by Boltzmann law,
$$\frac{n_i}{n_j} = \frac{g_i}{g_j}\exp\left(-\frac{E_i - E_j}{T}\right) \tag{2.49}$$
When an arbitrary number of charge states are present in the plasma, the relative ions abundances of two successive charge states n_{Z+1}, n_Z follow Saha-Boltzmann law,
$$\frac{n_{Z+1}}{n_Z} = \frac{2}{n_e\lambda_{th}^3}\exp\left(-\frac{E^0_{Z+1}-E^0_Z}{kT}\right)\left[\sum_{p\in J_{Z+1}} g_p \exp\left(-\frac{E_p - E^0_{Z+1}}{kT}\right) \Big/ \sum_{q\in J_Z} g_q \exp\left(-\frac{E_q - E^0_Z}{kT}\right)\right] \tag{2.50}$$

[8] Whether in equilibrium or not, $f_v(v)dv = f_\varepsilon(\varepsilon)d\varepsilon$.

where E_Z^0 stands for the energy of the ion with net charge Z at its ground state, and $\lambda_{th} \equiv \lambda_{dB}$ is the De Broglie thermal wave length,

$$\lambda_{th} = \frac{\hbar}{\sqrt{2m_e T}} \tag{2.51}$$

These equations assume that the free electrons are non-degenerate and treated as ideal gas. [9]

Local thermodynamic equilibrium

Compared to a TE plasma, which represents almost an ideal system, radiation may escape from real plasmas so that the detailed balance can be disturbed. In other words, photons in LTE plasmas are not necessarily in equilibrium with electrons and ions whose distributions of velocities, energies and excited states remain the same as for the TE conditions [10]. Actually,

[9] Two parameters [W49] are worth mentioning here which, by the way, give more insight into plasma regimes.

- The ideal gas limit corresponds to a null value $\Gamma = 0$ for the *Coulomb coupling parameter*, which is defined as the ratio of the potential energy to the kinetic energy of plasma particles $\Gamma =< E_{pot} > / < E_{kine} >$ and measures the degree to which many-body interactions affect the dynamics of particles. $\Gamma \ll 1$ corresponds to a weakly coupled system, whereas $\Gamma \gg 1$ reveals strong interparticle interactions. Moreover, for a system of ions of charge Ze at density n and temperature T,

$$\Gamma = \frac{(Ze)^2}{\left(\frac{4}{3}\pi n\right)^{1/3} T} \tag{2.52}$$

- Whether describing the energy distribution of electrons in a plasma by classical or quantum statistics depends on λ_{th} with respect to the interparticle distance $\sim n_e^{-1/3}$. Quantitatively, the *quantum degeneracy parameter* is defined as the ratio of thermal energy to Fermi energy $T_F = \frac{\hbar^2}{2m_e}(3\pi^2 n_e)^{2/3}$,

$$\theta = \frac{T_e}{T_F} \sim \left(\frac{\lambda_{th}}{n_e^{-1/3}}\right)^2 . \tag{2.53}$$

  If $\theta \ll 1$, the plasma is said to be *degenerated*, Fermi-Dirac statistics should be used to describe the dynamics of electrons and account for their fermionic nature,

$$n_{\mathrm{FD}}(\varepsilon) = \frac{1}{1 + \exp\left(-\frac{\mu - \varepsilon}{T_e}\right)} \tag{2.54}$$

  with μ is the chemical potential, $\varepsilon = p^2/(2m_e)$ the electron energy. If $\theta \gg 1$, quantum effects can be neglected, so that electrons in the non-degenerated plasma can be described by classical point particles. The Boltzmann statistics of one-particle states assess

$$n_{\mathrm{B}}(\varepsilon) = \exp\left(\frac{\mu - \varepsilon}{T_e}\right). \tag{2.55}$$

  The classical/quantum limit is set by $\theta = 1$, where $\frac{\mu}{T_e} \longrightarrow -\infty$ and $n_{\mathrm{FD}} \longrightarrow n_{\mathrm{B}}$.
  The quantum degeneracy ought to occur at high n_e where electrons get close to each other and at low T_e so that λ_{th} increases and wave packets increasingly overlap. It doesn't concern the plasma regime ($T_e \gg T_F$) studied in this thesis.

[10] Remind that the charge state distribution in LTE plasmas can be derived by minimizing the Helmholtz free energy F, defined in terms of the temperature and the partition function $Z(T)$ of the system

$$F = -T \log(Z(T)) \tag{2.56}$$

"local" can be interpreted as bounded by the mean free path (mfp) of photons emitted from the plasma λ_{mfp} and the collision length of electrons and ions. The crucial condition underlying the validity domain of LTE is that the rate of the energy-conserving collisional processes in the plasma is much higher than the rate of energy-dissipating radiative processes, predicting that the LTE condition is ensured at rather high electron densities. Rather high electron densities are therefore required by TE and LTE, but TE also implies reabsorption of emitted photons by the plasma when λ_{mfp} is large, i.e. the *optically thick* plasma. A rough criterium for the validity of the LTE between two levels i, j is estimated [B50] to be

$$n_e \geq 1.8 \times 10^{14} \sqrt{T_e} E_{ji}^3 \tag{2.57}$$

with n_e is in units of cm^{-3}, T_e and E_{ji} in eV.

Partial local thermodynamic equilibrium

Up to now, no specification has been provided to the temperature T – whether it's about electronic temperature T_e or ionic temperature T_i. The reason is that in TE and LTE plasmas, it is assumed that $T_e = T_i$. Nevertheless, in a PLTE plasma, $T_i \neq T_e$, so that it can no longer be described by a single temperature. The energy difference between the ground state and the first excited state is normally large, whereas the energy difference between the excited states is small [W51]. If n_e is high enough, the excited states can be in equilibrium among each other, excluding ground states, thus the "partial" LTE.

Non-LTE description and effective temperature

In non-equilibrium plasmas, statistical distributions are no longer applicable, various elementary processes cross sections should be taken into account to determine the population distribution of different levels according to a given model, such as the collisional-radiative model. Nevertheless, rather than accounting for kinetic effects, simpler approaches like the theory of *effective temperature* T_{eff} [A52][A53] can be used when suitable for spectral analysis, which is implicitly given by [A53]

$$\exp\left(-\frac{\Delta E}{T_{\mathrm{eff}}}\right) = \exp(-\beta) / \left[1 + \frac{2.75 \times 10^{12}}{0.15 + 0.28\chi(\beta)} \left(\frac{\Delta E^3 T_e^{1/2}}{n_e}\right)\right] \tag{2.58a}$$

with

$$\beta = \Delta E / T_e \tag{2.58b}$$

$$\chi(\beta) = \ln\left(1 + \frac{0.562 + 1.4\beta}{\beta + 1.4\beta^2}\right), \tag{2.58c}$$

n_e in units of cm^{-3} and ΔE in eV. For example, in tokamaks, tungsten impurities are present in different regions for which the temperatures and density vary significantly. As reported in the literature [A54] in ITER core plasma, the electronic temperature will reach 10–25 keV with charge states in the W^{57+}–W^{65+} range, while towards the edge of the main plasma column the expected temperature is much lower, the charge states being about W^{44+}–W^{50+}. The average electron density $\sim 10^{14}$ cm^{-3} is too low to ensure LTE. An analysis of ion and level populations as obtained from NLTE databases [A55][A56] and a calculation shown on Fig. 2.2 using the

online version of the FLYCHK code [A57] indicates that the "average" conditions of 8.8 keV and 10^{14} cm^{-3} may be modelled by an effective temperature in the 150–250 eV range, keeping the same electron density.

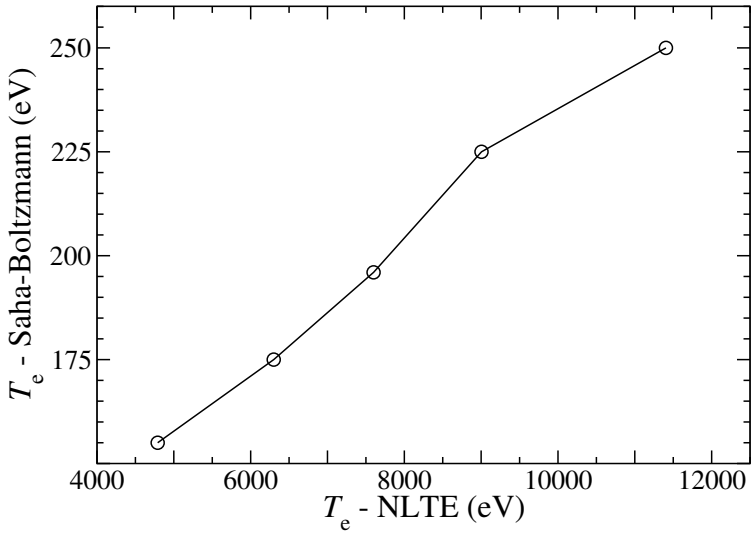

Figure 2.2: Effective temperature as a function of electron temperature for a 10^{14} e.cm^{-3} tungsten plasma as obtained by FLYCHK. The T_{eff} is the temperature which, assuming Saha-Boltzmann law, would give the same average charge as the non-LTE calculation from FLYCHK.

2.2.2 Spectral emissivity and opacity

Since the work of this thesis, both analytical and numerical parts (cf. chapter 4), involves only bound-bound transitions in LTE plasmas, neither the bound-free and free-free processes nor their contributions to the computation of emission and absorption spectra are discussed here.

The Einstein coefficients

The bound-bound processes, as shown in the Table 2.4, can be characterized by their respective Einstein coefficients, namely the spontaneous emission coefficient A_{21}, the induced (or stimulated) emission coefficient B_{21} and the photon absorption coefficient B_{12}. A schematic illustration is given in the Fig. 2.3 based on a 2-level system, denoted accordingly by 1 and 2.

- The Einstein spontaneous emission coefficient A_{21} (in units of s^{-1}) provides the rate of change of $n_2(t)$ atoms in 2 due to spontaneous transition to 1 such as

$$\frac{dn_2(t)}{dt} = -n_2(t)A_{21} \tag{2.59}$$

  and defines the *natural lifetime* of the atom in 2

$$\Delta t_2 = \frac{1}{A_{21}} \tag{2.60}$$

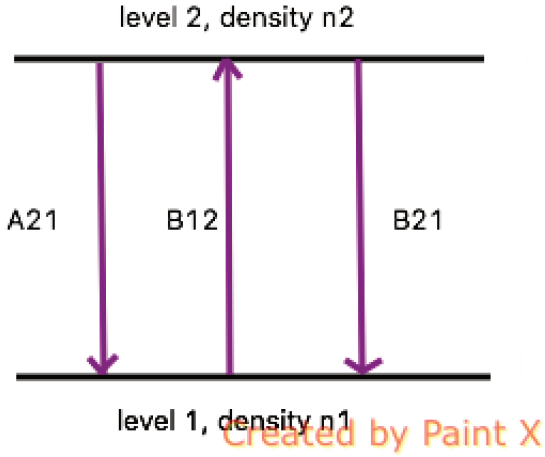

Figure 2.3: The three Einstein coefficients in a two-level system. The energy difference is given by $E = h\nu_{12}$.

meaning that if there is no other excitation nor de-excitation processes involved, $n_2(t) = n_2(0)\exp(-t/\Delta t_2)$.

- The Einstein absorption B_{12} and stimulated emission B_{21} coefficients (having dimensions of volume · angular frequency / (energy · time)[A58], in units of $J^{-1}\cdot m^3\cdot s^{-2}$ or equivalently $s^{-1}\cdot erg^{-1}\cdot cm^2\cdot sterad$) are related to the spectral energy density $\rho(\nu)$ of the radiation field assuming isotropic at frequency ν_{12}, which is the electromagnetic energy per unit volume and per unit frequency, such as

$$\begin{cases} \dfrac{dn_2(t)}{dt} = -n_2(t)B_{21}\rho(\nu) \\ \dfrac{dn_1(t)}{dt} = -n_1(t)B_{12}\rho(\nu) \end{cases} \tag{2.61}$$

  These equations are applicable if $\rho(\nu)$ does not change significantly over the line width.[11]

It is noteworthy that the Einstein coefficients arise from the intrinsic properties of each atom, whose mutual relationships are [A58]

$$\frac{B_{21}}{B_{12}} = \frac{g_1}{g_2}; \quad \frac{A_{21}}{B_{21}} = F(\nu) \text{ with } F(\nu) = \frac{8\pi h}{c^3}\nu^3. \tag{2.62}$$

Thus, the kinetic equation set giving the total variation of the system simplifies to

$$\begin{cases} \dfrac{dn_1(t)}{dt} = n_2(t)A_{21} - n_1(t)B_{12}\rho(\nu) + n_2(t)B_{21}\rho(\nu) = 0 \\ \dfrac{dn_2(t)}{dt} = -n_2(t)A_{21} + n_1(t)B_{12}\rho(\nu) - n_2(t)B_{21}\rho(\nu) = 0 \end{cases} \tag{2.63}$$

[11] In the opposite situation, for example under a strictly monochromatic laser radiation, the on-resonance excitation would produce *Rabi oscillations*, i.e. the population difference between 2 states (or 2 non-degenerated levels) oscillates in time with the Rabi frequency $\omega_R = \mu_{21}E/\hbar$, where E stands for the electric field amplitude of a linearly polarized light field and μ_{21} the transition dipole moment.

where the steady state is ensured under the assumption of plasmas in LTE condition. Using the mutual relationships of the Einstein coefficients in Eq. (2.62), one may solve one of Eq. (2.63) leading to the density ratio of level 1 to level 2 as

$$\frac{n_1}{n_2} = \frac{g_1}{g_2}\frac{F(\nu)+\rho(\nu)}{\rho(\nu)}. \tag{2.64}$$

Based on the Einstein coefficients, customary spectroscopic parameters such as

- emission oscillator strength f_{21} and its related absorption one f_{12}, where $|g_1 f_{12}| = |g_2 f_{21}| = |gf|$
- the absorption cross section σ_0 ;
- the transition dipole moment μ_{21} ;
- the line strength S_{21} of a transition, etc.

can be defined. For instance,

$$\frac{f_{12}}{A_{21}} = \frac{g_2}{g_1}\frac{2\pi\epsilon_0 mc^3}{\omega_{21}^2 e^2}, \quad \frac{S_{21}}{B_{12}} = 6g_1\epsilon_0\hbar^2, \quad \text{etc.} \tag{2.65}$$

The relationships between these parameters are well tabulated in [A58].

With the induced emission B_{21} being seen as the negative absorption, Einstein coefficients can be used to characterize emission and absorption of one atomic line radiation through coefficients such as

$$\begin{cases} \epsilon = \dfrac{h\nu}{4\pi} n_2 A_{21} & \text{for emission} \\ \kappa' = \dfrac{h\nu}{4\pi}(n_1 B_{12} - n_2 B_{21}) & \text{for absorption} \end{cases} \tag{2.66}$$

Concerning the interpretation of spectra in practice, emission intensity and (absorption) opacity are key quantities to study, which can be derived by radiative transfer equation given by the Kirchhoff law of thermal radiation in the framework of LTE condition. [12]

Zero-dimensional emission $\mathscr{E}^{0d}$

The spectral emission arising from a point-like source, which involves only bound-bound transitions and assumes that the reabsorption can be neglected [13], is given by

$$\mathscr{E}^{0d}(E) = n_i \sum_{ab} p_b A_{ba} E_{ba} \mathscr{S}_{ab}(E) \tag{2.69}$$

[12] The Kirchhoff law of thermal radiation reads

$$I_\nu = B_\nu \cdot (1 - \exp(-KL)) \tag{2.67}$$

where B_ν follows Planck's law, K denotes the absorption coefficient and L the thickness of the system. The spectral intensity B_ν is related to the spectral energy density ρ_ν by $B_\nu = \frac{c}{4\pi}\rho_\nu$.

[13] Otherwise, the bound-free spectral emission for a dimensionless source under the LTE assumption reads

$$\mathscr{E}^{0d}_{\text{b-f}}(E) = \frac{4\pi}{c^2} N_{\text{ions}} N_{\text{e}} E^3 \sum_{ab} \frac{p_b g_a}{g_b} \sigma_{ab}(E) \frac{\exp\left(-(E-E_{ba})^2/T\right)}{(2\pi m T)^{3/2}} \tag{2.68}$$

where N_{e} is the free-electron density, $\sigma_{ab}(E)$ the photo-ionization cross-section from a to b, and T the thermal energy.

where n_i denotes the ionic density, p_a the normalized a-level population ($\sum_a p_a = 1$) and $\mathscr{S}_{ab}(E)$ the normalized line shape ($\int dE\, \mathscr{S}_{ab}(E) = 1$).

Opacity κ

The spectral opacity at energy E is defined as

$$\kappa(E) = \frac{K}{\rho_m} \equiv \frac{\sigma(E)\mathscr{N}_{\mathrm{Av}}}{M}, \tag{2.70}$$

where ρ_m denotes the mass density of ions, $\mathscr{N}_{\mathrm{Av}}$ the Avogadro number, $\sigma(E)$ the absorption cross-section, and M the molar mass of the considered atom. K and ρ_m are related to n_i such as

$$K = n_i\sigma(E) \text{ and } \rho_m = \frac{n_i M}{\mathscr{N}_{\mathrm{Av}}}, \tag{2.71}$$

whereas the opacity $\kappa(E)$ does not depend on n_i. The total bound-bound contribution to the absorption cross-section involves a sum over transitions $a \to b$

$$\sigma(E) = \frac{h^3c^2}{8\pi}\sum_{ab} p_a \frac{g_b A_{ba}}{g_a E_{ba}^2}\mathscr{S}_{ab}(E) = 2\pi^2\alpha e^2 a_0 \sum_{ab} p_a f_{ab}\mathscr{S}_{ab}(E). \tag{2.72}$$

Line shape $\mathscr{S}_{ab}$

For non-hydrogenic highly ionized plasmas, a suitable approximation for $\mathscr{S}_{ab}(E)$ turns out to be Gaussian shape [B4], which reads

$$\mathscr{D}_{ab}(E) = \frac{1}{(2\pi)^{1/2}\sigma}\exp\left(-\frac{(E-E_{ba})^2}{2\sigma^2}\right) \tag{2.73a}$$

with variance σ^2 and half-width at half-maximum $hwhm$ given by

$$\sigma^2 = E_{ba}^2\frac{T}{Mc^2}, \quad hwhm = \sigma\sqrt{2\ln 2} \propto \sqrt{T}. \tag{2.73b}$$

The effect of ions' motion in the plasma is the broadening of the emission line into such Doppler profile. One may notice that the width of the Doppler broadening depends on the plasma temperature only– the higher the temperature, the larger is the line width. The relative Doppler line width, however, is very small.

Related to the natural lifetime Δt of a level, as defined in Eq. (2.60), the *Heisenberg uncertainties* state that the natural energy width of a level is of the order of $\hbar/\Delta t$. Therefore, the natural $fwhm$ (full-width at half-maximum) of a line ab is

$$fwhm = \hbar\left(\frac{1}{\Delta t_a} + \frac{1}{\Delta t_b}\right). \tag{2.74}$$

The natural broadening of a line ab is usually assumed to be described by a Lorentzian profile $\mathscr{L}_{ab}(\omega)$

$$\mathscr{L}_{ab}(\omega) = \frac{\Gamma_{ab}}{2\pi}\frac{1}{(\omega-\omega_0)^2 + (\Gamma_{ab}/2)^2} \tag{2.75}$$

with its $fwhm$ denoted by Γ_{ab} [B4].

In cases that the natural width is much less than the Doppler width, Gaussian profiles are preferred. However, if both widths must be accounted for, the resulting convolved profile is the Voigt function

$$\mathscr{V}_{ab}(E) = \frac{1}{(2\pi)^{1/2}\sigma_{\mathrm{D}}} V\left(\frac{E-E_{ba}}{2^{1/2}\sigma_{\mathrm{D}}}, \frac{\Gamma_{ab}}{2^{1/2}\sigma_{\mathrm{D}}}\right) \tag{2.76a}$$

where

$$V(A,B) = \frac{B}{\pi}\int_{-\infty}^{+\infty} dt \frac{\exp(-t^2)}{(t-A)^2+B^2} \tag{2.76b}$$

$$= \frac{1}{2}\left(\exp\left((-iA+B)^2\right)\mathrm{erfc}(-\mathrm{iA}+\mathrm{B}) + \exp\left((\mathrm{iA}+\mathrm{B})^2\right)\mathrm{erfc}(\mathrm{iA}+\mathrm{B})\right) \tag{2.76c}$$

where erfc stands for the complementary error function [B59]. Voigt function can be obtained numerically using fast and reasonably accurate methods [A60].

Line width is an important issue, especially for absorption spectra when Rosseland or the Planck mean is calculated. It may result from various broadening effects in plasmas, collisional as well as radiative. However, when individual lines gather into coalescent features, their line shapes are mostly hidden under the UTA width.

Chapter 3

Statistical description of unresolved transition arrays

In highly ionized plasmas, except some individual lines observed in the case of ions whose ground configuration only contains one electron out of a closed shell [B20], the numerous radiative lines generally gather into broad features, which may be studied as *Unresolved Transition Arrays* (UTA) according to the UTA model. It is well suited to describe transitions between configurations which contain large number of levels, for example configurations with open d or f shells. In fact, contrary to the detailed computation which requires the Hamiltonian diagonalization to obtain the N-electron quantum states, the statistical method consists in averaging the perturbative Hamiltonian (cf. Eq.(4.2)) using the invariance of its trace so that the average values can be expressed as compact analytical formulas [P61]. For instance, Bauche *et al* have thoroughly investigated the UTA model in a series of papers and derived formulas for the variance and shift of the distribution of array energies [A62][A63].

According to Condon and Shortley [B36], a transition array is defined as the totality of lines resulting from transitions between two configurations $C - C'$, characterized by its successive orders of *distribution moments* μ_n. For example, denoting E the energy of an array and $I(E)$ its emission intensity, cf. eg. Eq.(2.69), the distribution moments $\mu_n[I]$ such as

$$\mu_n[I] = \frac{\int_{-\infty}^{+\infty} I(E) E^n dE}{\int_{-\infty}^{+\infty} I(E) dE} \tag{3.1}$$

are of great interest. Within the framework of statistical spectroscopy, one may be led to evaluate distribution moments of various quantities, such as M_J values, level energies and radiative lines.

The UTA model is an *approximation* which consists in assuming a specific analytical shape $P(E)$, such as Gaussian or skewed Gaussian functions, assumed to be the same for all the transitions of the array, $I(E)$ is actually a convolution product

$$I(E) = P(E) * A(E) \quad \text{where} \quad A(E) = \sum_{ab} n_a A_{ab} \delta(E_{ab} - E). \tag{3.2}$$

In terms of distribution moments,

$$\mu_n[I] = \mu_n[P] + \mu_n[A], \tag{3.3a}$$

the approximation on $P(E)$ yields

$$\mu_n[I] \simeq \mu_n[A]. \tag{3.3b}$$

3.1 Elements of distribution theory

3.1.1 Moments

Definitions

As a mathematical concept, distribution moments represent a quantitative measure of the shape of a statistical distribution, whether continuous or discrete. The nth-order moment μ_n of a N-value quantity $X = \{X_i, i = 1..N\}$ is defined by

$$\mu_n[X] = \frac{\sum_{i=1}^{N}(X_i)^n \omega_i}{\sum_{i=1}^{N}\omega_i}, \quad n \geq 0, \tag{3.4}$$

where ω_i stands for the weight of the X_i value, $\sum_{i=1}^{N}\omega_i$ the total weight of the quantity. The moments are said to be unweighted, in case $\forall i, \omega_i = 1$.

The 0th-order moment μ_0 represents the total probability density (normalized to 1). The 1st-order moment μ_1 is the *mean* of the distribution, about which the *centered* moment μ_n^c can be defined

$$\mu_n^c[X] = \frac{\sum_{i=1}^{N}(X_i - \mu_1)^n \omega_i}{\sum_{i=1}^{N}\omega_i} \quad n \geq 1. \tag{3.5}$$

With respect to the *raw* moments μ_n – defined about the value 0, the centered moments μ_n^c focus more on the shape of the distribution independently of its localisation. The centered moments μ_n^c may also be expressed in terms of μ_n, for instance

$$\mu_2^c = \mu_2 - (\mu_1)^2 \tag{3.6a}$$

$$\mu_3^c = \mu_3 - 3\mu_2\mu_1 + 2(\mu_1)^3 \tag{3.6b}$$

$$\mu_4^c = \mu_4 - 4\mu_3\mu_1 + 6\mu_2(\mu_1)^2 - 3(\mu_1)^4 \tag{3.6c}$$

For example, a N-mass mechanical system in rotation around a given axis $\{(m_i, R_i), i = 1..N\}$ can be studied through the m_i-weighted distribution moments of R. According to the Eq. (3.4),

$$\mu_n[R] = \frac{\sum_{i=1}^{N}(R_i)^n m_i}{M_t}, \text{ with } M_t = \sum_{i=1}^{N} m_i \tag{3.7}$$

where M_t is the total mass of the system and R_i denotes the radius at which m_i rotates from the rotation axis. The 0th-order moment μ_0, representing M_t, is normalized to 1. The 1st-order moment $\mu_1 = (R_1 m_1 + R_2 m_2 + ... + R_N m_N)/M_t$ yields the center of mass. And the 2nd-order moment $\mu_2 = (R_1^2 m_1 + R_2^2 m_2 + ... + R_N^2 m_N)/M_t$ provides the rotational inertia.

Moments up to the 4th-order of the probability distribution are often denoted by their traditional names

- μ_1= the mean or the average.
- μ_2^c= the *variance* $v \equiv \sigma^2$, whose positive square root is the standard deviation σ. Based on the variance, it is possible to construct *normalized* nth-order centered moment α_n as

nth-order centered moment divided by σ^n

$$\alpha_n = \mu_n^c/(\sigma^n) \quad n \geq 2. \tag{3.8}$$

These dimensionless quantities have advantages to represent the distribution independently of any linear change of scale.

- α_3=the *skewness*, which represents a measure of the asymmetry of the distribution (with respect to a Gaussian shape). A symmetric (Gaussian) distribution corresponds to $\alpha_3 = 0$, whereas a skewed distribution can be specified whether by $\alpha_3 < 0$ (skewed to the left) or $\alpha_3 > 0$ (skewed to the right).
- α_4=the *kurtosis*, it provides a measure of the flattening of the distribution, compared to the normal distribution ($\alpha_4 = 3$) of the same variance [1]. So that a distribution having heavy tails ($\alpha_4 > 3$) corresponds to high kurtosis (leptokurtic) and a distribution having light tails ($\alpha_4 < 3$) corresponds to low kurtosis (platykurtic).

Usually, moments beyond the 4th-order are qualified high-order moments. High-order statistics, involving non-linear combination of data, can be used for description or estimation of further shape parameters [2][W64].

Moments of level energies and transition lines

When considering energy distribution of levels in a configuration or radiative line distribution in a transition array, the computation of their correspondant moments turn out to be essential. The importance of the calculation of such quantities in spectroscopic analysis has been stressed decades ago by Moszkowski [A22]. For example, application of averaging techniques to the computation of opacity of a high-temperature and high-density gold plasma has been proposed by Nardi and Zinamon [A65].

Distribution moments of quantum states in one configuration C reads

$$\mu_n(C) = \sum_{m \in C} \frac{(E_m)^n}{g_C}, \tag{3.9}$$

where $E_m = \langle m \mid H \mid m \rangle$, with H the atomic Hamiltonian, $\mid m >\equiv\mid \alpha JM >$ its eigenstates, and the sum runs over all states $\mid m >$ of configuration C; g_C=the total number of states, defined for example by a list of magnetic quantum numbers (m_l, m_s) of each electron. The knowledge of energy moments is essential when considering plasmas at LTE, being involved for instance in quantities like partition functions, or in the Saha-Boltzmann equation. [A32] Beyond the average energy of a configuration [B40] given by the moment μ_1, expressions have been published for the variance ($n = 2$)[A63][B20]. Concerning higher-order moments, formal methods have been proposed [A66], and explicit expressions given for the third-order moment [A67]. However, for $n \geq 4$ the available literature is rather scarce.

[1] Some references define the kurtosis coefficient as $\alpha_4 - 3$.

[2] As an example, in the same way that the kurtosis can be interpreted as the relative importance of tails versus shoulders in causing dispersion, the 5th-order moment provides the relative importance of tails versus center (mode, shoulders) in causing skew. For a given skew, high 5th-order moment corresponds to heavy tails and little movement of mode, whereas low 5th-order moment reveals more change in shoulders.

Distribution moments of radiative transitions between 2 configurations C and C' writes

$$\mu_n(C-C') = \sum_{mm'} \frac{(E_{m'}-E_m)^n w_{mm'}}{W} \tag{3.10}$$

with $E_{m'} = \langle m' \mid H \mid m' \rangle$, $E_m = \langle m \mid H \mid m \rangle$, the sum runs over all states $\mid m\rangle, \mid m'\rangle$ of configurations C, C' respectively; $w_{mm'}$=the strength of the $m-m'$ transition such as $w_{mm'} = \langle m \mid A \mid m' \rangle^2$ where A can be electric-dipole, magnetic-dipole operators, etc. cf. Eq.(4.42), $W = \sum_{mm'} w_{mm'}$.

The sums over states in the above equations can be limited to relativistic configurations in $j-j$ coupling, or to a single Russell-Saunders term. They can also be extended to more than two configurations in case of configuration mixing. These moments – shown in Eqs.(3.9)(3.10) – can be evaluated by means of the second quantization [3] and the tensor-operator formalisms, according to the procedure indicated in [B20] :

1. applying the second quantization methods, sums of products of matrix elements to calculate can be transformed into a small number of N-electron operators ;

2. then, the matrix elements of these operators are computed using Racah's tensor-operator techniques [A37][A38] as sums of product of Wigner $n-j$ coefficients.

Cumulants κ_r

As a set of descriptive constants of a distribution, cumulants can be more useful than moments from the theoretical standpoint to measure the properties of the distribution or to specify it [B68][B69][B70]. The interest of these quantities versus the ordinary moments is that the cumulants are additive if two phenomena are statistically independent. For example, for complex configurations with several open subshells $(n_1 l_1)^{p_1}(n_2 l_2)^{p_2}\cdots$, the total configurational cumulant of spin-orbit energies can be obtained by summing up cumulants of each subshells.

Unlike moments μ_n where $n \geq 0$, cumulants κ_r are defined from $r = 1$. The formal definition of the cumulant of order $r (r > 0)$ is given by [B68]

$$\exp\left(\sum_{r=1}^{\infty} \frac{\kappa_r t^r}{r!}\right) = \sum_{r=0}^{\infty} \frac{\mu_r t^r}{r!}. \tag{3.11}$$

In practice, it follows that the cumulants are related to the moments by the recursion formula [W71]

$$\kappa_n = \mu_n - \sum_{m=1}^{n-1} \binom{n-1}{m-1} \kappa_m \mu_{n-m}. \tag{3.12}$$

For instance, cumulants of up to the 10-th order are applied in the study of high order moments of spin-orbit energies in Chapter 4 whose expressions as a function of centered moments $\mu_n \equiv \mu_n^c$

[3] In general, the second quantization formalism is convenient for the distribution moments of the eigenvalues of any operator commuting with the Hamiltonian.

are as follows,

$$\kappa_2 = \mu_2 \tag{3.13a}$$
$$\kappa_3 = \mu_3 \tag{3.13b}$$
$$\kappa_4 = \mu_4 - 3\mu_2^2 \tag{3.13c}$$
$$\kappa_5 = \mu_5 - 10\mu_3\mu_2 \tag{3.13d}$$
$$\kappa_6 = \mu_6 - 15\mu_4\mu_2 - 10\mu_3^2 + 30\mu_2^3 \tag{3.13e}$$
$$\kappa_7 = \mu_7 - 21\mu_5\mu_2 - 35\mu_4\mu_3 + 210\mu_3\mu_2^2 \tag{3.13f}$$
$$\kappa_8 = \mu_8 - 28\mu_6\mu_2 - 56\mu_5\mu_3 - 35\mu_4^2 + 420\mu_4\mu_2^2 + 560\mu_3^2\mu_2 - 630\mu_2^4 \tag{3.13g}$$
$$\kappa_9 = \mu_9 - 36\mu_7\mu_2 - 84\mu_6\mu_3 - 126\mu_5\mu_4 + 756\mu_5\mu_2^2 + 2520\mu_4\mu_3\mu_2 + 560\mu_3^3 - 7560\mu_3\mu_2^3 \tag{3.13h}$$
$$\begin{aligned}\kappa_{10} = {} & \mu_{10} - 45\mu_8\mu_2 - 120\mu_7\mu_3 - 210\mu_6\mu_4 + 1260\mu_6\mu_2^2 - 126\mu_5^2 + 5040\mu_5\mu_3\mu_2 + 3150\mu_4^2\mu_2 \\ & + 4200\mu_4\mu_3^2 - 18900\mu_4\mu_2^3 - 37800\mu_3^2\mu_2^2 + 22680\mu_2^5.\end{aligned} \tag{3.13i}$$

3.1.2 Examples of distribution function

Whereas distribution moments of various orders are *exact* quantities, the choice of a particular distribution function is to some extent arbitrary, resulting mostly from computation tests [B20]. Independently of arbitrary choices, all distribution functions ought to converge to the same behaviour when moments of high enough orders are used.

Beyond the Gaussian assumption, i.e. in cases of moments other than average and variance are not insignificant the modelling of UTA different from "bell curved" shapes requires one to consider distributions including moments of orders higher than 2. For instance, the effect of the 3rd and the 4th reduced centered moments – representing respectively the skewness and the kurtosis of a distribution – on the statistical modelling of transition lines in complex atomic spectra has been investigated through the use of Gram-Charlier (GC), Generalized Gaussian (GG) and Normal Inverse Gaussian (NIG) distributions [A72].

Gram-Charlier function

Quite popular among statisticians, the Gram-Charlier (GC) type A distribution [B69] of variable X truncated at index p reads

$$\mathrm{GC}(X) = \frac{\Omega}{(2\pi)^{1/2}\sigma} \exp\left(-\frac{(X-\mu_1)^2}{2\sigma^2}\right)\left[1 + \sum_{n=3}^{p} c_n \mathrm{He}_n\left(\frac{X-\mu_1}{\sigma}\right)\right], \tag{3.14}$$

- The above distribution is normalized to the total area of the distribution Ω. For instance, if one analyzes the energy distribution of levels inside a configuration, Ω will be the configuration degeneracy $\Omega = g_C$, and $X = E$, $\mu_1 = E_{\mathrm{av}}$.
- The Gram-Charlier coefficients c_n are related to the scaled centered moments

$$\alpha_n = \mu_n/\sigma^n \text{ with } \sigma^2 := \mu_2 \text{ (or } \alpha_2 := 1) \tag{3.15a}$$

by

$$c_n = \sum_j \frac{(-1)^j \alpha_{n-2j}}{2^j j!(n-2j)!}. \tag{3.15b}$$

- He_n is the Hermite polynomial defined as [B59]

$$\mathrm{He}_n(X) = n! \sum_m \frac{(-1)^m X^{n-2m}}{2^m m!(n-2m)!} \tag{3.16}$$

  with the summation being restricted to m values for which the inverse factorials do not cancel.[4]

It is noteworthy that GC expansion represents probably the most intuitif choice of distribution when going beyond Gaussian assumption. Actually, as shown in Eq.(3.14), GC function is defined as a product of a normal distribution with a polynomial accounting for corrections departing from Gaussian form (corresponding to $\alpha_3 = 0$ and $\alpha_4 = 3$). Whereas GC expansion involves in a simple way moments of *any order*, it may exhibit negative features in certain circumstances which is quite bothersome.

Generalized Gaussian function

$$\mathrm{GG}(X) = \frac{\Omega p}{\sigma} \exp\left(- \mid \frac{(X-\mu_1)}{\sigma\lambda} \mid^p \right) \left[2\lambda\Gamma\left(\frac{1}{p}\right) \right]^{-1}, \quad \lambda = \sqrt{\Gamma\left(\frac{1}{p}\right) / \Gamma\left(\frac{3}{p}\right)} \tag{3.18}$$

where

- $\Gamma(X)$ is the ordinary gamma function ;
- p is a positive real parameter, which can be approximated by the following fitting function when constraining the kurtosis α_4 such as $\alpha_4 = \Gamma(\frac{1}{p})\Gamma(\frac{5}{p})/(\Gamma(\frac{3}{p}))^2$,

$$p = 1.62796 \left[\ln(\alpha_4 - 0.783143) \right]^{\frac{0.796349}{\alpha_4^2} - 1}. \tag{3.19}$$

Unlike GC expansions, GG functions do not have negative values. Furthermore, GG functions are symmetric (increasing for $\frac{X-\mu_1}{\sigma} < 0$ and decreasing for $\frac{X-\mu_1}{\sigma} > 0$), with the odd-order moments null.

[4] By the way, the Hermite polynomial of order n obeys the recursion relation

$$\mathrm{He}_{n+1}(X) = X\mathrm{He}_n(X) - n\mathrm{He}_{n-1}(X), \tag{3.17a}$$

where for examples, polynomials of up to the 4th-order have the following explicit expressions

$$\mathrm{He}_0(X) = 1, \tag{3.17b}$$
$$\mathrm{He}_1(X) = X, \tag{3.17c}$$
$$\mathrm{He}_2(X) = X^2 - 1, \tag{3.17d}$$
$$\mathrm{He}_3(X) = X^3 - 3X, \tag{3.17e}$$
$$\mathrm{He}_4(X) = X^4 - 6X^2 + 3. \tag{3.17f}$$

Normalized Inverse Gaussian function

Another example of distribution function without negative values, but accounts for both symmetric and asymmetric effects is the NIG distribution :

$$\mathrm{NIG}(X) = \frac{\Omega\left(ca\sqrt{a^2-b^2}\exp(c)+b(X-d)\right)}{\pi\sqrt{c^2+(X-d)^2}} K_1\left(a\sqrt{c^2+(X-d)^2}\right) \tag{3.20}$$

with K_1 is a modified Bessel function of the 3rd kind, and (a,b,c,d) are parameters of the distribution expressed as functions of moments of the first orders, cf. Table 1 in [A72].

In this thesis, only the GC expansions have been used, serving mainly for the convergence test of the distribution related to the analytical calculation of high-order moments of spin-orbit energies (cf. Sec.4.1.2.2), however, more details about the three distributions as well as their comparisons can be found in the referent paper [A72].

3.2 Computation of transition arrays by FAC

In order to illustrate the UTA concept, emission intensities arising from point-like plasmas are computed in both detailed and UTA approaches for comparison using the FAC code. As shown in Sec.3.2.1 below, spectra computed using UTA formulas are consistent with detailed ones in the case of electric dipole (E_1) transitions. In contrast, the numerical tests on magnetic dipole (M_1) transitions exhibit significant discrepancies, cf. Sec.4.2, leading us to develop a pseudo-UTA computation method explained in Sec.3.2.2.

3.2.1 Numerical example

$3d^24p-3d^24s$ transitions in KrX and ZrXIV plasmas

An empirical analysis is performed in the case of $3d^24p-3d^24s$ transitions in KrX and ZrXIV plasmas, cf. Fig. 3.1, using the FAC code.

In addition to the ability to calculate various radiative and collisional processes, as shown in Table 2.4, the atomic calculations in FAC [A30] can be carried out either in the configuration average approximation or using the detailed term accounting method, easily by calling the function *SetUTA*. In fact, the numerical subroutines implemented in FAC are exported through several Python modules. The computation task can therefore be completed in a flexible way by programming in the scripting language Python.[O31]. For instance, the radiative transition rates $A_{\alpha\beta}$ outputs from UTA computation provide the transition energy $E_{\alpha\beta}$ including the UTA shift, the Gaussian standard deviation, and the correction to the line strengths due to the configuration interaction within the same non-relativisitic configurations.

For the transition $3d^24p-3d^24s$, 61 levels and 359 lines are computed in the detailed approach, whereas 9 relativistic configurations and 6 arrays result from the UTA option. The UTA output is regrouped in Table 3.1.

The atomic data from FAC are then post-processed under the assumption of plasmas at LTE, with the populations n_a obtained from Saha-Boltzmann law shown in Eq.(2.50). Moreover, line shape is assumed to be normalized Doppler profile, cf. Eq.(2.73) and Gaussian distribution is

Configuration	Relativistic configuration	Index	Transition
$3d^2 4p$	$3d_+^2 4p_+$	8	$\rightarrow 2$
	$3d_- 3d_+ 4p_+$	7	$\rightarrow 1$
	$3d_+^2 4p_-$	6	$\rightarrow 2$
	$3d_-^2 4p_+$	5	$\rightarrow 0$
	$3d_- 3d_+ 4p_-$	4	$\rightarrow 1$
	$3d_-^2 4p_-$	3	$\rightarrow 0$
$3d^2 4s$	$3d_+^2 4s$	2	
	$3d_- 3d_+ 4s$	1	
	$3d_-^2 4s$	0	

Table 3.1: Configuration and array structures from UTA computation of the FAC code. For d-subshells, - stands for $j = 3/2$, + for $j = 5/2$; for p-subshells, - stands for $j = 1/2$, + for $j = 3/2$. The 9 relativistic configurations are indexed through 0 to 8 and sorted in the order of increasing energy, i.e. $E_0 < E_1 < ... < E_8$. The 6 relativistic transition arrays computed are listed in the upper part of the Table.

used for UTA profile.

$$P_{UTA} = \frac{1}{\sqrt{2\pi}\sigma_T} e^{-\frac{(E-\mu_1)^2}{2\sigma_T^2}} \quad \text{where} \quad \sigma_T^2 = \sigma_D^2 + \mu_2^c \tag{3.21}$$

As shown on Fig. 3.1,

- the constructed spectrum of Kr^{9+}(Z=36) consists of one Unresolved Transition Array (UTA), in agreement with the convolved spectrum. The array is characterized by an average of $\mu_1 = 21.03eV$ and a width $FWHM \simeq 2.35\sqrt{\mu_2^c} \simeq 3.5eV$. Percent error of UTA is estimated as $\delta \simeq 0.20\%$.

- The constructed spectrum of Zr^{13+}(Z=40) consists of two Spin-Orbit-Split Arrays (SOSA) as in the convolved spectrum. When Z increases, the spin-orbit integral begins to dominate over the inter-electronic ones. As a consequence, spin-orbit split gives rise to 2 relativistic sub-arrays, $3d^2 4p_{1/2} \longrightarrow 3d^2 4s$ and $3d^2 4p_{3/2} \longrightarrow 3d^2 4s$ whose average transition energies are 26.9 eV and 30.2 eV respectively.

3.2.2 High-order UTA construction

In order to test high-order moments in a spectral distribution, or to analyze the detailed spectra as provided numerically by the FAC code, a "constructed" or pseudo-UTA computation method was developed and designed in the following way.[A33] The various detailed transitions are sorted, so that all lines connecting a pair of given relativistic configurations (α, β) are collected in this pseudo-UTA structure. Since the oscillator strengths are known from the detailed transition list, we may compute the average energies and centered moments for each pair of

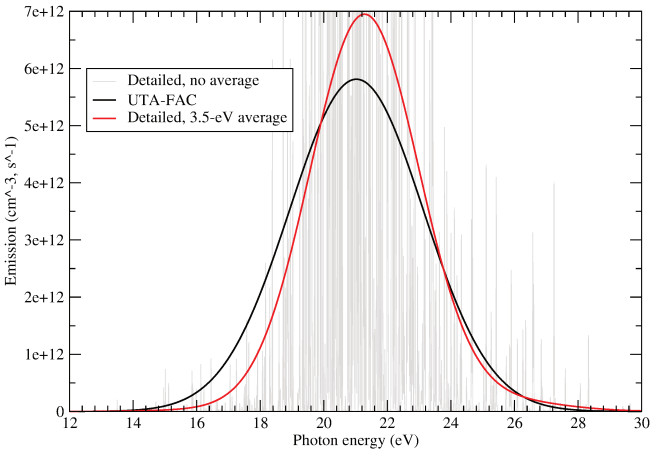

(a) $3d^2 4p - 3d^2 4s$ in Kr^{9+}(Z=36)

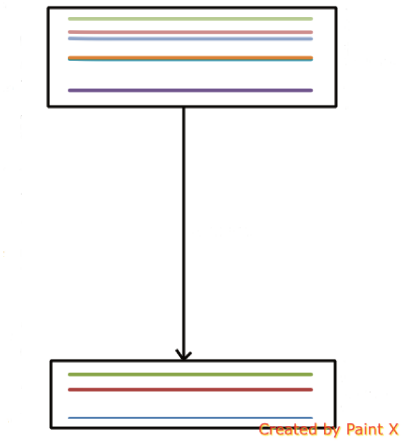

(b) The 359 lines gather into 1 UTA.

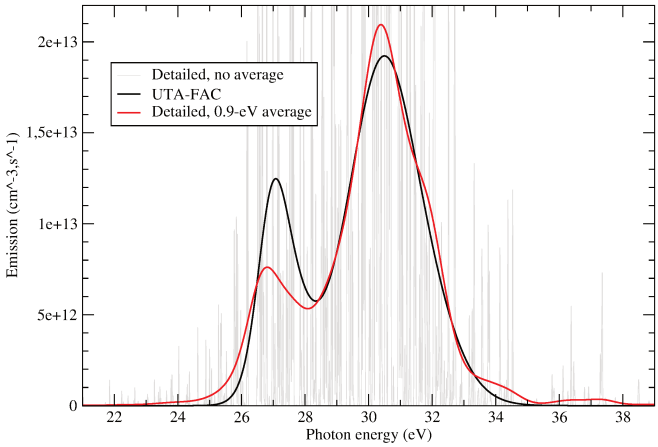

(c) $3d^2 4p - 3d^2 4s$ in Zr^{13+}(Z=40)

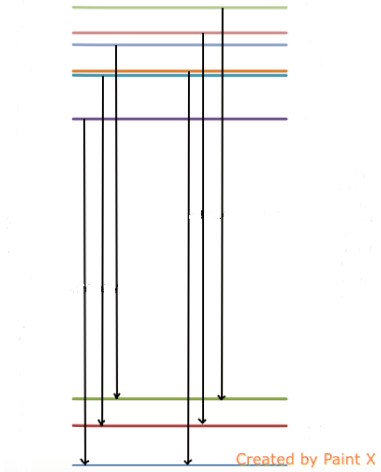

(d) The 359 lines gather into 2 groups of SOSAs.

Figure 3.1: Detailed and UTA zero-dimensional emission spectra accounting for electric dipole E_1 transitions $3d^2 4p - 3d^2 4s$ in two plasmas of different atomic numbers Z: Krypton X (Z=36) and Zirconium XIV (Z=40), on subfigures 3.1a and 3.1c respectively. The horizontal lines on subfigures 3.1b and 3.1d stand for the configurational energies $E_0, E_1, ...E_8$ listed in Table 3.1, from the bottom to the top, whose differences are vertically scaled. FAC output is post-processed assuming an electron temperature of 5000 eV and density of 10^{23} cm^{-3}. The grey lines result from the detailed computation including Doppler line shapes. The red curves are derived from the detailed computation after convolution by a 3.5 eV-FWHM response function in the case of Krypton X and a 0.9 eV-FWHM response function in the case of Zirconium XIV. The purple curves are the spectra obtained using the UTA formulas as provided by FAC and Gaussian profile.

relativistic configurations α, β using the relations

$$E_{\alpha\beta} = \sum_{\substack{a\in\alpha \\ b\in\beta}} g_a f_{ab} E_{ab} \Big/ \sum_{\substack{a\in\alpha \\ b\in\beta}} g_a f_{ab} \tag{3.22a}$$

$$\mu^{(k)}_{\alpha\beta} = \Big\langle (E - E_{\alpha\beta})^k \Big\rangle = \sum_{\substack{a\in\alpha \\ b\in\beta}} g_a f_{ab} \, (E_{ab} - E_{\alpha\beta})^k \Big/ \sum_{\substack{a\in\alpha \\ b\in\beta}} g_a f_{ab} \tag{3.22b}$$

where the sums run over detailed levels pairs ab, g_a being the degeneracy of level a, f_{ab} the absorption oscillator strength for the $a \to b$ transition, and E_{ab} is the level energy difference. Of course the pseudo-UTA $\alpha\beta$ exists provided that the detailed computation involves at least one level-level transition ab associated to it. Using these transition-array moments, we may construct new "pseudo-UTA" spectra through the averaged formulas

$$\mathscr{E}^{0d}_{\text{pU b-b}}(E) = \sum_{\alpha\beta} U_{\alpha\beta} \mathscr{S}_{\alpha\beta}(E) \tag{3.23a}$$

where the source term in this collecting scheme is given by

$$U_{\alpha\beta} = \sum_{\substack{a\in\alpha \\ b\in\beta}} p_b A_{ba} E_{ab}. \tag{3.23b}$$

As in Eq. (2.73) the lineshape can be assumed to be Gaussian

$$\mathscr{S}_{\alpha\beta}(E) = \frac{1}{(2\pi)^{1/2}\sigma_{\alpha\beta}} \exp\left(-\frac{(E - E_{\alpha\beta})^2}{2\sigma^2_{\alpha\beta}} \right) \tag{3.23c}$$

$$\text{with } \sigma^2_{\alpha\beta} = E^2_{\alpha\beta} k_B T/(Mc^2) + \mu^{(2)}_{\alpha\beta} \tag{3.23d}$$

the variance (3.23d) including Doppler effect and the energy dispersion as given by Eq. (3.22b).

As seen by comparing these relations with Eq. (2.69) the pseudo-UTA (3.23) is defined so that the integral of the spectrum is conserved, notably

$$\int dE \, \mathscr{E}^{0d}_{\text{b-b}}(E) = \int dE \, \mathscr{E}^{0d}_{\text{pU b-b}}(E) = \sum_{ab} p_b A_{ba} E_{ba}. \tag{3.24}$$

Such numerical techniques will be illustrated in the case of tungsten plasmas in Sec.4.2.

Chapter 4

Computation of distribution moments

In this chapter, the theoretical methods and numerical procedure (cf. Sec.3.2.2) exposed previously will be applied to two cases : one consists of high-order moments computation of spin-orbit energies inside a multi-electron configuration, and the other deals with transition arrays of magnetic-dipole type in tungsten plasmas. The present writing uses material from two papers [A32] [A33] published during the thesis.

4.1 High-order moments of spin-orbit energies

The non-central Hamiltonian $H^{'}$, cf. Eq.(2.5), in a semi-relativistic approximation [B40] is composed by an electron-electron V_{ee} part[1], and a spin-orbit V_{so} one[2]

$$H^{'} = \sum_{p<q} \frac{1}{r_{pq}} + \sum_{k} \xi(r_k) l_k s_k = V_{\text{ee}} + V_{\text{so}}. \tag{4.2}$$

[1] Contrary to the one-electron spin-orbit operator V_{so}, the inter-electronic Coulomb energy operator V_{ee} involves two electrons, where 1,2 represent electrons 1 and 2 indistinguishably. Through multiple expansion of $1/r_{12}$ [B40]:

$$\frac{1}{r_{12}} = \frac{1}{\sqrt{r_1^2 + r_2^2 - 2r_1 r_2 \cos\omega}} = \sum_{k=0} \frac{r_<^k}{r_>^{k+1}} P_k(\cos\omega) \tag{4.1a}$$

where $r_< = \min(r_1, r_2)$, $\quad r_> = \max(r_1, r_2)$ and $P_k(\cos\omega)$ is the Legendre polynomial, defined as

$$P_l(\cos\omega) = \frac{4\pi}{2l+1} \sum_{m=-l}^{l} (-1)^m Y_{l,-m}(\theta_1, \phi_1) Y_{l,m}(\theta_2, \phi_2), \tag{4.1b}$$

the Coulomb operator V_{ee} can be expressed as a composition of a radial part and an angular part

$$\frac{1}{r_{12}} = \sum_{k=0} \frac{r_<^k}{r_>^{k+1}} \sum_{q=-k}^{k} (-1)^q C_{-q}^{(k)}(\theta_1, \phi_1) C_q^{(k)}(\theta_2, \phi_2), \quad C_q^{(k)} = \sqrt{\frac{4\pi}{2k+1}} Y_{kq} \tag{4.1c}$$

where the angular part is given by a function of spherical harmonics. Quantities $C_q^{(k)}$, usually called "special" spherical harmonics in theoretical atomic spectroscopy, are used when a spherical function plays the role of an operator.

[2] Notice that $[\xi(r_k), l_k s_k] = 0$.

The purpose of this section is to consider high-order moments of energy distribution, cf. Eq.(3.9), related to the spin-orbit interaction – the interaction between the orbital momentum and the spin of an electron – considering mostly highly-charged ions for which this interaction rules the electron-electron interaction $V_{\rm so} > V_{\rm ee}$. More precisely, moments $\left\langle V_{\rm so}^k \right\rangle$ for a series of k values are obtained in both coupled and uncoupled schemes.

The operator $V_{\rm so}$ can be preferably expressed in terms of raising and lowering operators $l_\pm$, cf. Eq.(B.7),

$$V_{\rm so} = \sum_p \xi(r_p) \left[\frac{1}{2}(l_{p+} s_{p-} + l_{p-} s_{p+}) + l_{pz} s_{pz} \right]. \tag{4.3a}$$

or in terms of j, l, s

$$V_{\rm so} = \sum_p \xi(r_p) \frac{j_p^2 - l_p^2 - s_p^2}{2}, \tag{4.3b}$$

according to whether an uncoupled basis $|l m_l s \sigma\rangle$ or a coupled one $|l s j m\rangle$ is used.

Averaging method

The calculation of the average of the k-th power of the atomic Hamiltonian on a N-electron configuration relies on the use of the *Uylings theorem* [A73] (see also Appendix in [A63]), which states that the average of a k-particle operator $O^{(k)}$ on a N-electron configuration may be derived from the average computed on the k-electron configuration through a binomial factor $\binom{N}{k}$

$$\left\langle O^{(k)} \right\rangle_N = \binom{N}{k} \left\langle O^{(k)} \right\rangle_k. \tag{4.4}$$

When dealing with average matrix element determination of a sub-shell $(nl)^N$ occupied by N electrons, it means that the number of electrons to be taken into account in a configuration – depending on operator's "nature"– can be minimized to k (usually less than 3 in atomic spectroscopy). Thus, an arbitrary sub-shell $(nl)^N$ can be studied with a reduced configuration $|\mathcal{C}\rangle = (nl)^k, k \ll N$. Then, the average values in Eq.(4.4) are obtained by summing the expression $\langle \phi_k | O_k | \phi_k \rangle$ over all antisymmetric states ϕ_k in the configuration $(nl)^k$ and divided by the degeneracy g_k of the configuration, whether relativistic or not. The numerator is the *trace* of the operator [A74] and therefore may be computed in any basis.

If the quantum numbers of the j-th electron are denoted by q_j, the g_k elements involved in the trace are defined by the set $(q_1, q_2 \cdots q_k)$ where all q_j are different and ordered. Accounting for anti-symmetrization of wave functions, the trace is

$$\mathrm{Tr} O_k = \binom{4l+2}{k} \left\langle O^{(k)} \right\rangle_k = \sum_{q_1 < \cdots < q_k} f(q_1 \cdots q_k), \tag{4.5a}$$

$$\text{with} \quad f(q_1 \cdots q_k) = \sum_{\tau \in \mathcal{S}_k} \varepsilon_\tau \left\langle q_1 \cdots q_k | O_k | q_{\tau(1)} \cdots q_{\tau(k)} \right\rangle \tag{4.5b}$$

where $\mathcal{S}_k$ is a permutation group[3]. among k elements and ε_τ the signature of the permutation τ.

It is noteworthy that

- the sum index $q_1 < \cdots < q_k$ in Eq.(4.5a) means that each set is counted only once ;
- the trace computation is significantly simplified by noting that the summed quantity f is fully symmetric in the exchange of any pair of indexes $f(q_1, q_2 \cdots) = f(q_2, q_1 \cdots)$;
- because of the sum $\sum_{\tau \in \mathcal{S}_k} \varepsilon_\tau$, f vanishes if two indexes are equal $f(q_1, q_1 \cdots) = 0$.

As a result,

$$\mathrm{Tr} O_k = \frac{1}{k!} \sum_{q_1 \cdots q_k} f(q_1 \cdots q_k), \tag{4.6}$$

the sum over non-repeated indexes may be replaced by the sum where $q_1 \cdots q_k$ vary freely, which is much more convenient to perform. [4]

[3] Regarding the *class* structure of the symmetric group S_n [B69], the number of classes of S_n is the number of ways in which the integer n can be partitioned into a sum of positive integers. For examples, if $n = 3$, the number of classes of S_3=3:

- $3 = 3$: cyclic permutations (123)
- $3 = 2 + 1$: transpositions (12)(13)(23)
- $3 = 1 + 1 + 1$: identity

where *canonical* notations (ijp) are adopted, and which mean that the i-th position value is replaced by j-th position value, the j-th position value is replaced by the p-th one, and p-th one is replaced by the i-th. If $n = 4$, the number of classes of S_4=5:

- $4 = 4$: no object remains in its own place, nor do any 2 objects undergo a single transposition (6x)
- $4 = 3 + 1$: cyclic permutations on 3 objects leaving the 4th unchanged (8x)
- $4 = 2 + 2$: 2 interchanges in pairs (3x)
- $4 = 2 + 1 + 1$: 1 transposition leaving the remaining 2 objects unchanged (6x)
- $4 = 1 + 1 + 1 + 1$: identity (1x)

where there are au total 4!=24 permutations to consider. Besides, the number of k-particle permutations is $k!$, whose list can be found with *Mathematica* (command line: "Permutations[list, {k}]").

[4] For example, in the case of trace calculation over inter-dependent double $\sum_{i<j}$ and triple sums $\sum_{i<j<p}$

$$\sum_{i<j} f_{ij} \Rightarrow \frac{1}{2} \sum_i \sum_j f_{ij} - \frac{1}{2} \sum_{i=j} f_{ij} \tag{4.7a}$$

$$\sum_{i<j<p} f_{ijp} \Rightarrow \left(\frac{1}{6} \sum_{i,j,p} - \frac{1}{6} \sum_{i=j,p} - \frac{1}{6} \sum_{i=p,j} - \frac{1}{6} \sum_{p=j,i} + \frac{1}{3} \sum_{i=j=p} \right) f_{ijp} \tag{4.7b}$$

4.1.1 Analytical formulas for spin-orbit moments

Average values over one-electron configuration

As will be shown later, moments $\left\langle V_{\mathrm{so}}^k \right\rangle$ for a series of k values can be expressed as functions of one-electron average values $\left\langle (\boldsymbol{l.s})^k \right\rangle$ such as

$$\left\langle (\boldsymbol{l.s})^k \right\rangle \equiv \left\langle (nl)^1 | V_{\mathrm{so}}^k | (nl)^1 \right\rangle, \tag{4.8a}$$

which, dropping the constant radial factor $\xi(r)$,

$$\left\langle (\boldsymbol{l.s})^k \right\rangle = \frac{1}{2(2l+1)} \sum_{\mu\sigma} \left\langle \mu\sigma \left| (\boldsymbol{l.s})^k \right| \mu\sigma \right\rangle = \frac{1}{2(2l+1)} \sum_{jm} \left\langle jm \left| (\boldsymbol{l.s})^k \right| jm \right\rangle. \tag{4.8b}$$

The most straightforward method lies in using the coupled basis jm, where the spin-orbit term is diagonal. Generally, when the basis used makes an Hamiltonian term diagonal, the average determination can be largely simplified. For $j = l \pm 1/2$, the level degeneracies are $2l$ and $2l+2$ and the spin-orbit energies $-(l+1)/2$ and $l/2$ respectively, so that

$$\left\langle (\boldsymbol{l.s})^k \right\rangle = \frac{1}{2(2l+1)} \sum_j \left(j(j+1) - l(l+1) - 3/4 \right)^k \Big/ 2^k \tag{4.9a}$$

$$= \frac{l(l+1)}{2^k(2l+1)} \left[(-1)^k (l+1)^{k-1} + l^{k-1} \right]. \tag{4.9b}$$

This provides the average values for the first k values, with $X = l(l+1)$,

$$\langle \boldsymbol{l.s} \rangle = 0 \tag{4.10a}$$

$$\left\langle (\boldsymbol{l.s})^2 \right\rangle = \frac{X}{4} \tag{4.10b}$$

$$\left\langle (\boldsymbol{l.s})^3 \right\rangle = -\frac{X}{8} \tag{4.10c}$$

$$\left\langle (\boldsymbol{l.s})^4 \right\rangle = \frac{X}{16}(X+1) \tag{4.10d}$$

$$\left\langle (\boldsymbol{l.s})^5 \right\rangle = -\frac{X}{32}(2X+1) \tag{4.10e}$$

$$\left\langle (\boldsymbol{l.s})^6 \right\rangle = \frac{X}{64}(X^2+3X+1) \tag{4.10f}$$

$$\left\langle (\boldsymbol{l.s})^7 \right\rangle = -\frac{X}{128}(X+1)(3X+1) \tag{4.10g}$$

$$\left\langle (\boldsymbol{l.s})^8 \right\rangle = \frac{X}{256}(X^3+6X^2+5X+1) \tag{4.10h}$$

$$\left\langle (\boldsymbol{l.s})^9 \right\rangle = -\frac{X}{512}(2X+1)(2X^2+4X+1) \tag{4.10i}$$

$$\left\langle (\boldsymbol{l.s})^{10} \right\rangle = \frac{X}{1024}(X+1)(X^3+9X^2+6X+1) \tag{4.10j}$$

A direct inspection of these equations shows that these average values follow the relation

$$\left\langle (\boldsymbol{l}.\boldsymbol{s})^k \right\rangle = \left(-\frac{1}{2}\right)^k X \sum_{j=0}^{\mathrm{int}(k/2)-1} \binom{k-j-2}{j} X^j \tag{4.11}$$

where $\mathrm{int}(k/2)$ is the integer part of $k/2$.

4.1.1.1 Spin-orbit moments in uncoupled scheme

Concerning the first 2 moments, the moment $k=1$ is clearly null, and the variance ΔV_{so}^2 is well known (see, e.g. [B20])

$$\kappa_2(\mathrm{so}) = \left\langle V_{\mathrm{so}}^2 \right\rangle = \frac{l(l+1)}{4(4l+1)} N(4l+2-N) \left\langle \xi \right\rangle^2 . \tag{4.12}$$

A simple expression can be provided for the moment $k=3$ called "skewness".

Skewness

The cube of the spin-orbit interaction involves three terms

$$V_{\mathrm{so}}^3 = S_1 + S_2 + S_3 \tag{4.13a}$$

$$S_1 = \sum_i (\xi_i \boldsymbol{l_i}.\boldsymbol{s_i})^3 \tag{4.13b}$$

$$S_2 = 3 \sum_{i<j} \left[(\xi_i \boldsymbol{l_i}.\boldsymbol{s_i})^2 \xi_j (\boldsymbol{l_j}.\boldsymbol{s_j}) + i \leftrightarrow j \right] \tag{4.13c}$$

$$S_3 = 6 \sum_{i<j<k} (\xi_i \boldsymbol{l_i}.\boldsymbol{s_i} \, \xi_j \boldsymbol{l_j}.\boldsymbol{s_j} \, \xi_k \boldsymbol{l_k}.\boldsymbol{s_k}) . \tag{4.13d}$$

The radial part for the considered sub-shell $\langle \xi_i \rangle^3 = \langle nl \,|\xi(r)|\, nl \rangle^3$ is a common factor in all these formulas and will be dropped unless mentioned. One may obtain the average values or traces of each of these operators using Uylings' theorem, cf. Eq. (4.4). For instance, the S_1 average value will be calculated for $N=1$. One first computes the trace, then divides it by $2(2l+1)$ to get $\langle S_1 \rangle_1$. If $N=1$ the uncoupled basis states are $nl\mu_1\sigma_1$ where the magnetic quantum numbers verify $-l \le \mu_1 \le l$, $-1/2 \le \sigma_1 \le +1/2$. From the average value in Eq. (4.10c), one gets immediately

$$\mathrm{Tr}(S_1) = \sum_{\mu_1\sigma_1} \left\langle \mu_1\sigma_1 \left| (\boldsymbol{l_1}.\boldsymbol{s_1})^3 \right| \mu_1\sigma_1 \right\rangle = -2(2l+1)\frac{l(l+1)}{8}. \tag{4.14}$$

The trace of 2-particle operator is calculated accordingly. For symmetry reasons both terms inside the brackets give the same contribution. The $1/k!$ factor in Eq.(4.6) compensates this factor 2, so that, writing explicitly the permutations τ and dropping unneeded single-electron

indexes,

$$\mathrm{Tr}(S_2) = 3(d_2 - e_2) \tag{4.15a}$$

$$d_2 = \sum_{\substack{\mu_1\sigma_1\\ \mu_2\sigma_2}} \left\langle \mu_1\sigma_1 \left| (\boldsymbol{l}.\boldsymbol{s})^2 \right| \mu_1\sigma_1 \right\rangle \langle \mu_2\sigma_2 \left| \boldsymbol{l}.\boldsymbol{s} \right| \mu_2\sigma_2 \rangle \tag{4.15b}$$

$$e_2 = \sum_{\substack{\mu_1\sigma_1\\ \mu_2\sigma_2}} \left\langle \mu_1\sigma_1 \left| (\boldsymbol{l}.\boldsymbol{s})^2 \right| \mu_2\sigma_2 \right\rangle \langle \mu_2\sigma_2 \left| \boldsymbol{l}.\boldsymbol{s} \right| \mu_1\sigma_1 \rangle . \tag{4.15c}$$

The direct term d_2 is, up to a constant, the product of average values $\langle (\boldsymbol{l}.\boldsymbol{s})^2 \rangle \langle \boldsymbol{l}.\boldsymbol{s} \rangle$ the second of which vanishes. The exchange term e_2 is easily derived from the closure relation

$$\sum_{\mu\sigma} |\mu\sigma\rangle\langle\mu\sigma| = 1 \tag{4.15d}$$

and, using again the average value in Eq. (4.10c), one gets the trace

$$\mathrm{Tr}(S_2) = -3e_2 = -3 \sum_{\mu_1\sigma_1} \left\langle \mu_1\sigma_1 \left| (\boldsymbol{l}.\boldsymbol{s})^3 \right| \mu_1\sigma_1 \right\rangle = \frac{3}{4}(2l+1)l(l+1). \tag{4.15e}$$

In the computation of the trace of the operator S_3, one has to perform the sum over the 3! permutations of $\mathcal{S}_3$. If any permutation lets one index invariant, e.g. $\tau(3) = 3$, its contribution to the trace cancels since it involves the sum $\langle \mu_3\sigma_3 \left| \boldsymbol{l}.\boldsymbol{s} \right| \mu_3\sigma_3 \rangle$. Therefore, only the two third-order cycles contribute to $\mathrm{Tr}(S_3)$, and for symmetry reasons their contributions are equal. One readily gets

$$\mathrm{Tr}(S_3) = 2 \sum_{\substack{\mu_1\mu_2\mu_3\\ \sigma_1\sigma_2\sigma_3}} \langle \mu_1\sigma_1 \left| \boldsymbol{l}.\boldsymbol{s} \right| \mu_2\sigma_2 \rangle \langle \mu_2\sigma_2 \left| \boldsymbol{l}.\boldsymbol{s} \right| \mu_3\sigma_3 \rangle \langle \mu_3\sigma_3 \left| \boldsymbol{l}.\boldsymbol{s} \right| \mu_1\sigma_1 \rangle \tag{4.16a}$$

$$= 2 \sum_{\mu_1\sigma_1} \left\langle \mu_1\sigma_1 \left| (\boldsymbol{l}.\boldsymbol{s})^3 \right| \mu_1\sigma_1 \right\rangle \tag{4.16b}$$

$$= 4(2l+1) \left\langle (\boldsymbol{l}.\boldsymbol{s})^3 \right\rangle = -\frac{1}{2} l(l+1)(2l+1) \tag{4.16c}$$

which show that all elements of $\langle V_{\mathrm{so}}^3 \rangle$ are reducible to the single-electron average.

According to Uylings theorem

$$\left\langle V_{\mathrm{so}}^3 \right\rangle = \sum_{j=1}^{3} \binom{N}{j} \mathrm{Tr}(S_j) \Big/ \binom{4l+2}{j} \tag{4.17}$$

and from 3 previous expressions of trace, one gets the contribution of spin-orbit interaction to the configuration skewness

$$\left\langle V_{\mathrm{so}}^3 \right\rangle_N = \langle \xi \rangle^3 \, \frac{(l+1)}{16(4l+1)} N(4l+2-N)(N-2l-1). \tag{4.18}$$

This expression agrees with the result from Kučas and Karazija [A67]. The skewness vanishes for an empty or closed subshell as well as for a half-filled one. It depends on $M = N - 2l - 1$ as $M(M^2 - (2l+1)^2)$. More generally one may easily check that V_{so}^{2k+1} (resp. V_{so}^{2k}) is an odd (resp. even) function of M.

Kurtosis

Expanding the fourth power of the spin-orbit interaction one gets

$$V_{\rm so}^4 = K_1 + K_2 + K_2' + K_3 + K_4 \tag{4.19a}$$
$$K_1 = \sum_i (\xi_i \boldsymbol{l_i.s_i})^4 \tag{4.19b}$$
$$K_2 = 4\sum_{i<j} \left[(\xi_i \boldsymbol{l_i.s_i})^3 \xi_j (\boldsymbol{l_j.s_j}) + i \leftrightarrow j \right] \tag{4.19c}$$
$$K_2' = 6\sum_{i<j} (\xi_i \boldsymbol{l_i.s_i})^2 (\xi_j \boldsymbol{l_j.s_j})^2 \tag{4.19d}$$
$$K_3 = 12 \sum_{i<j<k} \left[(\xi_i \boldsymbol{l_i.s_i})^2 \xi_j \boldsymbol{l_j.s_j} \xi_k \boldsymbol{l_k.s_k} + (ijk) + (ikj) \right] \tag{4.19e}$$
$$K_4 = 24 \sum_{i<j<k<m} \xi_i \boldsymbol{l_i.s_i} \xi_j \boldsymbol{l_j.s_j} \xi_k \boldsymbol{l_k.s_k} \xi_m \boldsymbol{l_m.s_m} \tag{4.19f}$$

where in (4.19e) $(ijk), (ikj)$ stands for the cyclic permutations of indexes. Using the same techniques as above, one gets, after computing the sum over the permutations in $\mathcal{S}_k$,

$$\mathrm{Tr}(K_1)/\binom{4l+2}{1} = \langle K_1 \rangle_1 = m_4 \tag{4.20a}$$
$$\mathrm{Tr}(K_2)/\binom{4l+2}{2} = \langle K_2 \rangle_2 = -\frac{8m_4}{4l+1} \tag{4.20b}$$
$$\mathrm{Tr}(K_2')/\binom{4l+2}{2} = \langle K_2' \rangle_2 = \frac{6}{4l+1}\left(2(2l+1)m_2^2 - m_4\right) \tag{4.20c}$$
$$\mathrm{Tr}(K_3)/\binom{4l+2}{3} = \langle K_3 \rangle_3 = \frac{18}{l(4l+1)}\left(-(2l+1)m_2^2 + m_4\right) \tag{4.20d}$$
$$\mathrm{Tr}(K_4)/\binom{4l+2}{4} = \langle K_4 \rangle_4 = \frac{36}{l(4l-1)(4l+1)}\left((2l+1)m_2^2 - m_4\right) \tag{4.20e}$$

where the one-electron average values

$$m_n = \langle (\boldsymbol{l.s})^n \rangle \tag{4.21}$$

are detailed previously. After some algebra, the expression of the fourth moment reads

$$\left\langle V_{\rm so}^4 \right\rangle_N = \langle \xi \rangle^4 \frac{(l+1)N(4l+2-N)}{32(4l-1)(4l+1)} f_4 \tag{4.22a}$$
$$\text{with } f_4 = 2l(2l+1)^2(3l^2+l-1) - 3(2l^3+2l^2-1)(N-2l-1)^2 \tag{4.22b}$$
$$= 2l(4l-1)(l^2+l+1) + 3(2l^3+2l^2-1)(N-1)(4l+1-N). \tag{4.22c}$$

The 4th-order cumulant, sometimes called "excess" measuring the sharpness of the distribution, is defined as

$$\kappa_4(\mathrm{so}) = \left\langle V_{\rm so}^4 \right\rangle - 3\left\langle V_{\rm so}^2 \right\rangle^2. \tag{4.23}$$

Using the known value of the variance, one gets

$$\kappa_4(\mathrm{so}) = -\frac{(l+1)N(4l+2-N)}{32(4l-1)(4l+1)^2}k_4 \tag{4.24a}$$

with

$$k_4 = \left[2l(2l+1)^2(2l^2+1) + c_4(N-2l-1)^2\right] \tag{4.24b}$$

$$c_4 = 3(4l^3+4l^2-4l-1) \tag{4.24c}$$

and since $4l^3+4l^2-4l-1>0$ for $l>0$, the factor k_4 is also positive. This proves that the excess of the spin-orbit distribution is negative, which means it is flatter than a Gaussian profile.

Higher-order moments

Using the same techniques, calculations for the next average values can be performed. For instance, the result for $k=5$ is

$$\left\langle V_{\mathrm{so}}^5 \right\rangle_N = -\langle\xi\rangle^5 \frac{(l+1)(2l+1-N)N(4l+2-N)}{64(4l-1)(4l+1)}f_5 \tag{4.25a}$$

$$\text{with } f_5 = (2l+1)^2(10l^2+6l-1) - 2(5l^3+7l-3)(N-2l-1)^2. \tag{4.25b}$$

And for $k=6$,

$$\left\langle V_{\mathrm{so}}^6 \right\rangle_N = \langle\xi\rangle^6 \frac{(l+1)N(4l+2-N)}{128(4l-3)(4l-1)(4l+1)}f_6 \tag{4.26a}$$

$$\begin{aligned}\text{with } f_6 = {} & 2l(2l+1)^4(15l^4-14l^2-l+3) \\ & -5(2l+1)^2(12l^5+12l^4-6l^3-19l^2-5l+3)(N-2l-1)^2 \\ & +5(6l^5+12l^4+6l^3-13l^2-17l-6)(N-2l-1)^4.\end{aligned} \tag{4.26b}$$

However this method becomes cumbersome when dealing with high-order moments because it is necessary to account for k-particle interaction and for the whole set of permutations $\mathcal{S}_k$.

4.1.1.2 Spin-orbit moments in coupled scheme

General formulas

Using the eigenvectors of the operators j_i^2 and j_{iz} noted as $\{j_i m_i\}\,(i=1\ldots N)$, a N-electron state obeying Pauli principle is defined by the occupation number ν for the total angular momentum $j=l-1/2$, by the set of ν distinct values $m_1^-,\cdots m_\nu^-$ and by the set of $N-\nu$ distinct values $m_1^+,\cdots m_{N-\nu}^+$ for $j=l+1/2$. The number of allowed states is given by the possible choice of ν magnetic quantum numbers among $2l$ and $N-\nu$ magnetic quantum numbers among $2l+2$, i.e.,

$$g(N,\nu,l) = \binom{2l}{\nu}\binom{2l+2}{N-\nu}. \tag{4.27}$$

Since the spin-orbit Hamiltonian is diagonal in this basis, the energy of a relativistic configuration of populations $\nu, N-\nu$ is straightforwardly obtained as

$$E_{\mathrm{so}} = \frac{\langle\xi\rangle}{2}\left(Nl-(2l+1)\nu\right). \tag{4.28}$$

The radial term $\langle\xi\rangle$ identical for all states in a configuration will be omitted in the following formulas. The average k-th power of spin-orbit energy is therefore

$$\left\langle V_{\mathrm{so}}^k \right\rangle_N = \frac{1}{2^k \binom{4l+2}{N}} \sum_\nu \binom{2l}{\nu} \binom{2l+2}{N-\nu} (Nl-(2l+1)\nu)^k . \tag{4.29}$$

Such average values are computed using the identity

$$\sum_\nu \binom{M}{\nu} \binom{N}{k-\nu} \frac{\nu!}{(\nu-p)!} = \frac{M!}{(M-p)!} \binom{M+N-p}{k-p} \tag{4.30}$$

derived from the Taylor expansion of $M(M-1)\ldots(M-p+1)(1+X)^{M+N-p}$. In order to use this formula one has to express the term $[Nl-(2l+1)\nu]^k$ in (4.29) as a function of the polynomials

$$\phi_j(\nu) = \nu(\nu-1)\cdots(\nu-j+1), \text{ with } \phi_0(\nu) = 1. \tag{4.31}$$

Writing any k-th degree polynomial as

$$P_k(X) = \sum_{j=0}^{k} c_j^{(k)} \phi_j(X) \tag{4.32}$$

for $X = 0, 1 \cdots k$ successively, one gets a set of $k+1$ linear equations which can be readily solved for the $c_j^{(k)}$

$$c_j^{(k)} = \frac{1}{j!} \sum_{i=0}^{j} (-1)^{j-i} \binom{j}{i} P_k(i). \tag{4.33}$$

Identifying $P_k(X)$ with $[Nl-(2l+1)X]^k$, one can then write the moment (4.29) using its definition and (4.33)

$$\left\langle V_{\mathrm{so}}^k \right\rangle_N = \frac{2^{-k}}{\binom{4l+2}{N}} \sum_{j=0}^{j_{\max}} \frac{(2l)!}{(2l-j)!} \binom{4l+2-j}{N-j} \sum_{i=0}^{j} \frac{(-1)^{j-i}}{i!(j-i)!} [Nl-(2l+1)i]^k \tag{4.34a}$$

$$= 2^{-k} \sum_{j=0}^{j_{\max}} \frac{(2l)!(4l+2-j)!N!}{(2l-j)!(4l+2)!(N-j)!} \sum_{i=0}^{j} \frac{(-1)^{j-i}}{i!(j-i)!} [Nl-(2l+1)i]^k \tag{4.34b}$$

with

$$j_{\max} = \min(k, 2l, N). \tag{4.34c}$$

This expression is apparently more complex than (4.29) since it involves a double sum. In fact, since $0 \le i \le j \le k$, for the lowest k values very few terms have to be computed, and this number of terms — at maximum $k+1$ values for j and $(k+1)(k+2)/2$ values for i — is independent of the number of electrons N in the sub-shell. Besides this formula is easy to implement in a formal algebra software such as Mathematica. By the way, on the expression (4.29), one readily verifies that changing ν in $2l-\nu$ and $N-\nu$ in $2l+2-(N-\nu)$ and therefore N in $4l+2-N$, the contribution of this sub-shell to the moment is multiplied by $(-1)^k$. This shows that

$$\left\langle V_{\mathrm{so}}^k \right\rangle_{4l+2-N} = (-1)^k \left\langle V_{\mathrm{so}}^k \right\rangle_N \tag{4.35}$$

a property that was obviously verified on the various $\left\langle V_{\mathrm{so}}^k \right\rangle$ moments detailed in the previous sub-section.

Using the double sum formula (4.34b)for the moment $\left\langle V_{\mathrm{so}}^k \right\rangle$, and defining $M = N - 2l - 1$, one obtain easily analytical expressions for $k > 6$. Moments from the 7th to the 10th-order are listed below.

$$\left\langle V_{\mathrm{so}}^7 \right\rangle = \frac{(l+1)N(4l+2-N)(N-2l-1)}{512(4l-3)(4l-1)(4l+1)}[A_7(l) + B_7(l)M^2 + C_7(l)M^4] \tag{4.36a}$$

$$\text{with } A_7(l) = 2(2l+1)^4(105l^4 + 56l^3 - 55l^2 - 28l + 3) \tag{4.36b}$$

$$B_7(l) = -5(2l+1)^2(84l^4 + 140l^3 + 64l^2 - 21l - 18) \tag{4.36c}$$

$$C_7(l) = 3(70l^4 + 196l^3 + 234l^2 + 133l + 30), \tag{4.36d}$$

$$\left\langle V_{\mathrm{so}}^8 \right\rangle = \frac{(l+1)N(4l+2-N)}{1024(4l-5)(4l-3)(4l-1)(4l+1)}[A_8(l) + B_8(l)M^2 + C_8(l)M^4 + D_8(l)M^6], \tag{4.37a}$$

$$A_8(l) = 4l(2l+1)^6(105l^6 - 105l^5 - 147l^4 + 85l^3 + 87l^2 - 13l - 15) \tag{4.37b}$$

$$B_8(l) = -14(2l+1)^4(90l^7 + 30l^6 - 162l^5 - 248l^4 + 38l^3 + 182l^2 + 40l - 15) \tag{4.37c}$$

$$C_8(l) = 35(2l+1)^2(36l^7 + 60l^6 - 12l^5 - 196l^4 - 208l^3 - 20l^2 + 73l + 30) \tag{4.37d}$$

$$D_8(l) = -7(60l^7 + 180l^6 + 180l^5 - 280l^4 - 888l^3 - 932l^2 - 459l - 90), \tag{4.37e}$$

$$\left\langle V_{\mathrm{so}}^9 \right\rangle = \frac{(l+1)N(4l+2-N)(N-2l-1)}{1024(4l-5)(4l-3)(4l-1)(4l+1)} [A_9(l) + B_9(l)M^2 + C_9(l)M^4 + D_9(l)M^6] \tag{4.38a}$$

$$\text{with } A_9(l) = (2l+1)^6(1260l^6 - 252l^5 - 1770l^4 - 332l^3 + 564l^2 + 182l - 15) \tag{4.38b}$$

$$B_9(l) = -7(2l+1)^4(540l^6 + 684l^5 - 204l^4 - 886l^3 - 468l^2 + 43l + 60) \tag{4.38c}$$

$$C_9(l) = 7(2l+1)^2(540l^6 + 1476l^5 + 1530l^4 + 244l^3 - 786l^2 - 625l - 150) \tag{4.38d}$$

$$D_9(l) = -2(630l^6 + 2646l^5 + 5184l^4 + 5773l^3 + 3777l^2 + 1361l + 210), \tag{4.38e}$$

$$\left\langle V_{\mathrm{so}}^{10}\right\rangle = \frac{(l+1)N(4l+2-N)}{4096(4l-7)(4l-5)(4l-3)(4l-1)(4l+1)}[A_{10}(l)+B_{10}(l)M^2 + C_{10}(l)M^4+D_{10}(l)M^6+E_{10}(l)M^8] \tag{4.39a}$$

$$\text{with } A_{10}(l) = 4l(2l+1)^8\left(945l^8-2520l^7+3090l^5+226l^4-1594l^3 -484l^2+241l+105\right) \tag{4.39b}$$

$$B_{10}(l) = -6(2l+1)^6\left(2520l^9-2520l^8-7140l^7-4450l^6+13410l^5 +13126l^4-4286l^3-6819l^2-1051l+315\right) \tag{4.39c}$$

$$C_{10}(l) = 21(2l+1)^4\left(1080l^9+720l^8-3000l^7-9300l^6-3560l^5 +10564l^4+12051l^3+2459l^2-2074l-840\right) \tag{4.39d}$$

$$D_{10}(l) = -42(2l+1)^2\left(360l^9+840l^8+60l^7-4410l^6-8450l^5-4918l^4 +3083l^3+6007l^2+3243l+630\right) \tag{4.39e}$$

$$E_{10}(l) = 9\left(420l^9+1680l^8+2520l^7-3220l^6-18760l^5-33476l^4 -32829l^3-18951l^2-6074l-840\right). \tag{4.39f}$$

Following the computation of the analytical formulas above, a special emphasis can be put on the choice of an adequate basis beforehand when performing averaging techniques. In the case of high-order moments of spin-orbit energies, since the spin-orbit Hamiltonian is diagonal in the coupled basis, the averages computation in coupled scheme is more favourable than in uncoupled one.

4.1.2 Comparison of analytical expressions to numerical computations

The spin-orbit energy moments computed with the present analytical formulas are compared to the numerical results from Cowan's code [B40]. An option in Cowan's code allows one to cancel the electron-electron interaction, leading to an energy structure depending on spin-orbit interaction only. All the data from Cowan's code is kindly provided by J.C. Pain and F. Gilleron.

4.1.2.1 Analysis of moments for single and multiple open sub-shell

Two configurations are considered, one is composed by one sub-shell – $3d^6$ configuration in Au^{55+}, and the other of two open sub-shells – $3p^23d^6$ configuration in Au^{59+}.

Moments for a single open sub-shell

As a first example, the moments up to $n = 10$ for the $3d^6$ configuration in Au^{55+} with an Ar-like core are presented in Table 4.1. The Cowan's code provides the spin-orbit integral $\langle\xi\rangle_{3d} = 39.865$ eV. The variance derived from the analytical form in Eq. (4.12) is 6356.9 eV^2, which fairly agrees with the numerical determination from Cowan's code of 6357 eV^2. The various higher-order moments are listed as absolute values μ_n and as scaled values α_n, i.e., divided by σ^n, where σ^2 is the variance. The last two columns are obtained with the analytical expressions given above.

In Table 4.1, it appears that the spin-orbit moments computed with Cowan's code fairly agree with the present determination at any order, as absolute as well as scaled values. We note on columns 2-3 that including the electronic interaction mostly affect the low- and odd-order moments. We do not have a definite explanation for this feature, but we may empirically state that electron-electron interaction contributes more significantly than spin-orbit to the asymmetry of energy structure.

By the way, one may evaluate analytically the moments for n up to 3 in the case where electronic interaction is also accounted for. A relatively tractable example is shown in Appendix C, which consists of analytical calculations of $\langle V_{\rm ee} V_{\rm so}^2 \rangle$. And the analysis of third-order moment including electron-electron interaction is presented in Appendix B of [A32], where a sign error in a previously published asymmetry formula has been corrected and the agreement is reached when comparing the corrected expression $\mu_{\rm ee}^{(3)}$ to Cowan's numerical data. Limited to variance calculations, the Cowan's code provides for the Slater integrals the following values: $F^{(2)}(3d,3d) = 75.677$ eV and $F^{(4)}(3d,3d) = 48.937$ eV, inserting these values in the variance formulas available in the literature (Table 3.2 in Ref. [B20]), we get $\langle (V_{\rm ee} - \langle V_{\rm ee} \rangle)^2 \rangle = 334.7$ eV^2 and $\langle V_{\rm so}^2 \rangle = 6356.9$ eV^2, the total variance being 6691.6 eV^2, which fairly agrees with the one in Table 4.1. Nevertheless, the derivation of moments including both $V_{\rm ee}$ and $V_{\rm so}$ is outside the scope of our consideration and would be a tremendous task with probably page-long formulas if $n > 3$.

Table 4.1: Absolute and scaled centered moments of energy distribution for the $3d^6$ configuration in Au^{55+} with an Ar-like core. The results from Cowan's code are computed both with the complete interaction ($V_{\rm ee}, V_{\rm so}$) and with only spin-orbit terms ($V_{\rm so}$). The notation 1.195(8) stands for 1.195×10^8. Analytical values of moments including the whole interaction are not available at any order, however values for $n = 2$ and 3 are given in the main text.

	Cowan's code			This work	
	Centered moment		Scaled moment	Centered moment	Scaled moment
n	$\mu_n(V_{\rm ee}, V_{\rm so})$	$\mu_n(V_{\rm so})$	$\alpha_n(V_{\rm so})$	$\mu_n(V_{\rm so})$	$\alpha_n(V_{\rm so})$
2	6692	6357	1	6356.87	1
3	8111	3.168(4)	0.062500	3.16771(4)	0.0625
4	1.195(8)	1.11(8)	2.747768	1.11037(8)	2.7477679
5	7.187(8)	2.16(9)	0.670201	2.15930(9)	0.67020089
6	3.128(12)	2.929(12)	11.399971	2.92843(12)	11.399972
7	7.351(13)	1.427(14)	6.968505	1.42722(14)	6.9685059
8	1.002(17)	9.738(16)	59.621394	9.73590(16)	59.621399
9	6.277(18)	9.73(18)	74.722146	9.72849(18)	74.722153
10	3.824(21)	3.999(21)	385.137765	3.99792(21)	385.13780

Ion with two open sub-shells

As mentioned in the section 3.1, more complex configurations with multiple opened sub-shells $(n_1 l_1)^{p_1} (n_2 l_2)^{p_2} \cdots$ can be dealt with using cumulants, cf. Eq. (3.12). The cumulants computed for each sub-shell add up for the spin-orbit part, provided that the spin-orbit interaction does not couple different sub-shells. [5] In order to illustrate the case of two open sub-shells, we present

[5] This result does not apply to the electronic interaction $V_{\rm ee}$. For instance, the variance accounting for this interaction is a function of Slater integrals involving distinct sub-shells [B20].

in Table 4.2 the moments up to $n = 6$ for the $3p^2 3d^6$ configuration in Au^{59+} with a Mg-like core. In addition to the centered moments, the cumulants defined in Eq. (3.13) have been extracted from Cowan's data. The spin-orbit parameters $\langle\xi\rangle$ are 326.842 eV and 42.261 eV for $3p$ and $3d$ sub-shells respectively. With the present analytical formulas for $\langle V_{\rm so}^n\rangle$, we have computed the cumulants for each sub-shell separately as well as their sums. In Table 4.2, we verify that the sum of the contributions of each sub-shell is in fair agreement with the cumulant derived from Cowan's data. However, when the order n increases, since each cumulant is proportional to $\langle\xi\rangle^n$, the $3p$ sub-shell has a much larger contribution than the $3d$ sub-shell, and the additivity property loses its significance. That is why we restrict the analysis to $n \leq 6$.

Contrary to what was observed in the previous case of $3d^6$, the moments involving $V_{\rm ee}$ and $V_{\rm so}$ (column 2 of Table 4.2) do not differ much from the moments involving $V_{\rm so}$ only (column 3) whatever the order. This is because we consider here a configuration $3p^2 3d^6$ while the previous case involved only d electrons. As a rule, the spin-orbit integral decreases more rapidly with the angular momentum l than the Slater integrals.

Table 4.2: Centered moments and cumulants for the levels of $3p^2 3d^6$ configuration in Au^{59+} with a Mg-like core. The columns 2 and 3 contain the centered moments μ_n obtained with Cowan's code, with electron interaction respectively included or not. Column 4 gives the list of cumulants κ_n (3.13) derived from Cowan's data with only spin-orbit included. The three rightmost columns are computations using the spin-orbit parameter provided by the Cowan's code and the present analytical formulas. The tabulated cumulants refer to the $3p^2$ sub-shell, the $3d^6$ sub-shell, and the whole configuration for columns 5–7 respectively. All data relative to order n are in units of eV^n. The notation 9.26(4) stands for 9.26×10^4.

	Data from Cowan's code			Cumulants from analytical formulas		
n	$\mu_n(V_{\rm ee}, V_{\rm so})$	$\mu_n(V_{\rm so})$	$\kappa_n(V_{\rm so})$	$\kappa_n(3p^2)$	$\kappa_n(3d^6)$	κ_n total
2	9.48(4)	9.26(4)	9.26(4)	8.546(4)	7.144(3)	9.260(4)
3	−7.332(6)	−6.945(6)	−6.945(6)	−6.983(6)	3.774(4)	−6.945(6)
4	2.171(10)	2.092(10)	−4.804(9)	−4.793(9)	−1.287(7)	−4.806(9)
5	−7.394(12)	−6.991(12)	−5.599(11)	−5.595(11)	1.950(8)	−5.593(11)
6	8.23(15)	7.712(15)	1.992(15)	1.993(15)	5.265(10)	1.993(15)

4.1.2.2 Analysis of Gram-Charlier expansion

The evolution of the Gram-Charlier expansion (cf. Eq. (3.14)) built with the spin-orbit moments for the $3d^6$ configuration of Au^{55+} is shown on Fig. 4.1 for various truncation indexes p. The spectrum built with energies and degeneracies from Cowan's code where $V_{\rm ee}$ is unaccounted for is plotted too, with an arbitrary Lorentzian lineshape (cf. Eq.(2.75)) of 2-eV FWHM. This lineshape is included only to facilitate the visual comparison between distributions, but it is not included in the moment computations.

When varying the truncation index p we observed that the case $p = 3$ in the Gram-Charlier expansion is hardly distinguishable from the pure Gaussian case $p = 2$ — the difference being below 2% — and for the sake of clarity the $p = 3$ case was not plotted on Fig. 4.1. The same observation can be made for the next values $p \lesssim 10$. For $p = 12$ some asymmetry appears and increases gradually. The Gram-Charlier expansion is then changing significantly even when p increases by one unit. Two separate components appear in the distribution for $p > 15$. For $p = 22$ the expansion is clearly negative for energies around ±230 eV. The position of the peaks in the Gram-Charlier distribution gets in better agreement with Cowan's data when p increases.

Nevertheless we may check that for indexes p up to 42 no convergence is reached since the expansion still varies significantly.

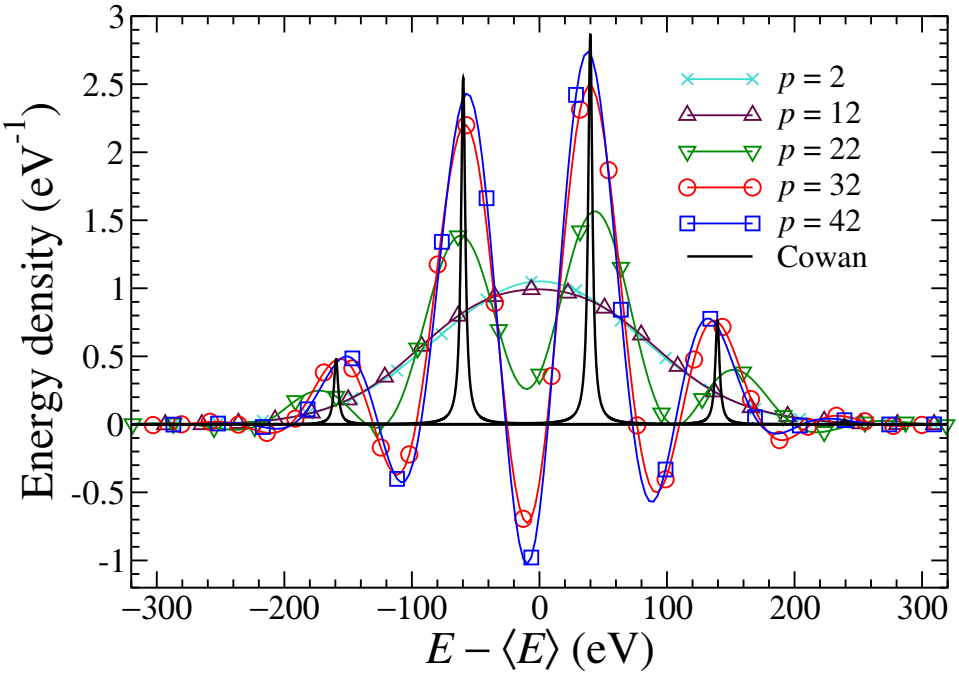

Figure 4.1: Gram-Charlier distribution for the spin-orbit energy of the $3d^6$-configuration in Au^{55+} with an Ar-like core. The various curves correspond to the expansions truncated at various indexes p. For comparison purpose one has plotted the data from Cowan's code where each energy level is arbitrarily represented by a Lorentzian of 2 eV FWHM not accounted for in the moment computation. The Gram-Charlier curves are normalized to the degeneracy $g = 210$. The ordinates for Cowan's data have been divided by a suitable factor in order to allow comparison.

Convolution procedure

This absence of convergence can be explained and amended as follows. The "theoretical" energy distribution we try to represent by a Gram-Charlier expansion is indeed a "Dirac comb" since no broadening is accounted for on individual components. From a general point of view, the Gram-Charlier expansion is relevant for statistical phenomena such as coalescent transition arrays and not when individual lines show up. In order to verify this point we have performed the convolution of the energy distribution by a Gaussian profile $\exp(-E^2/2\tau^2)/(2\pi)^{(1/2)}\tau$. This can be considered as a mathematical artifact to monitor convergence. More significantly from a physical point of view it may also account for various broadening processes such as Stark broadening or Zeeman effect with a inhomogeneous magnetic field. In favour of this analysis we mention that the convolution of a Gram-Charlier expansion characterized by variance σ^2 and coefficients c_n with a Gaussian profile of variance τ^2 is again a Gram-Charlier expansion with

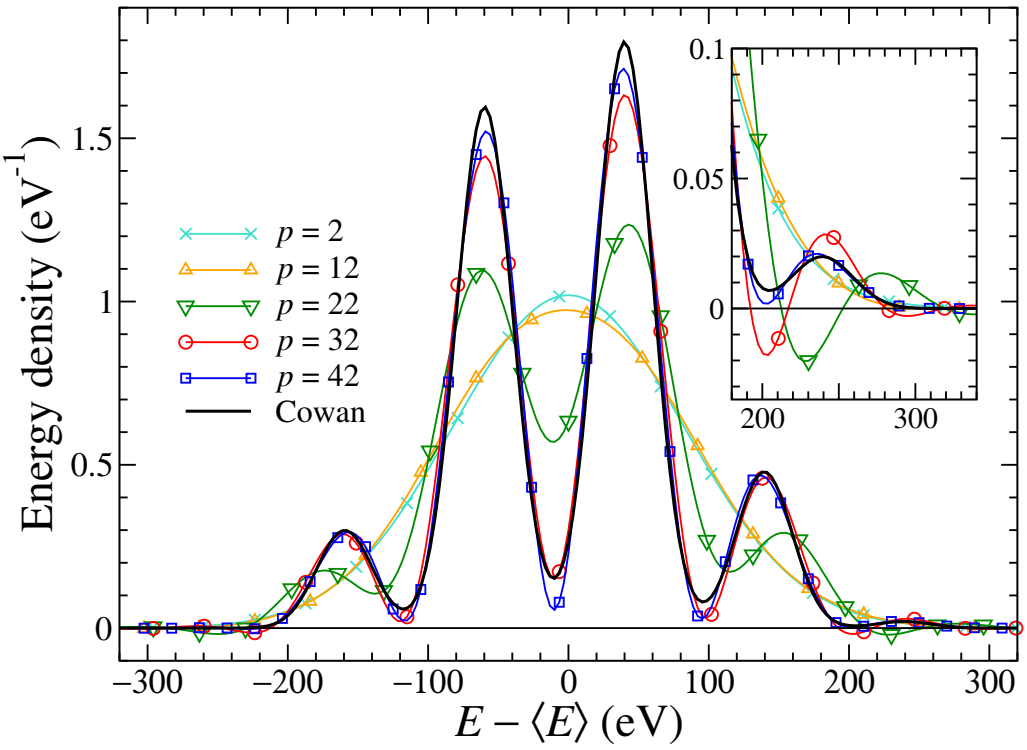

Figure 4.2: Gram-Charlier distribution for the spin-orbit energy of the $3d^6$-configuration in Au^{55+} with an Ar-like core convolved by a Gaussian profile with standard deviation $\tau = 20$ eV. The Gram-Charlier curves and Cowan's data are normalized to the degeneracy $g = 210$.

variance

$$\upsilon^2 = \sigma^2 + \tau^2 \tag{4.40a}$$

and coefficients $c'_n = (\sigma/\upsilon)^n c_n$, the convolved function being

$$F'_{\mathrm{GC}}(X) = \frac{g}{(2\pi)^{1/2}\upsilon} e^{-X^2/2\upsilon^2} \left(1 + \sum_n (\sigma/\upsilon)^n c_n He_n(X/\upsilon)\right). \tag{4.40b}$$

The scaled moments of the convolved energy distribution $\alpha'_n = \mu'_n/(\mu'_2)^{n/2}$ are related to the transformed coefficients c'_n through an equation formally similar to (3.15b). One gets

$$\alpha'_n = \frac{n!\sigma^n}{(\sigma^2+\tau^2)^{n/2}} \sum_j \frac{(\tau/\sigma)^{2j}\alpha_{n-2j}}{2^j j!(n-2j)!} \tag{4.41a}$$

$$= \frac{\pi^{-1/2}}{(\sigma^2+\tau^2)^{n/2}} \sum_k \binom{n}{k} \frac{1+(-1)^{n-k}}{2} \sigma^k (2\tau^2)^{(n-k)/2} \Gamma\left(\frac{n-k+1}{2}\right) \alpha_k \tag{4.41b}$$

a relation that was previously established by Pain and Gilleron (Eq. (40) in [A75]). The effect of this convolution is illustrated by Fig. 4.2 with the same Cowan's data as on Fig. 4.1 and including a convolution by a profile with standard deviation $\tau = 20$ eV which ensure the coalescence of lines. In this case a good agreement is observed between convolved Cowan's data and Gram-Charlier expansion at order $n \simeq 42$. One also notes that for high enough n, the negative part of the energy distribution has almost disappeared. Because of the factor $(\sigma/\upsilon)^n$ in Eq. (4.40b), increasing the Gaussian width τ improves the convergence speed.

Convergence analysis

In order to ensure that we did reach convergence in the latter case considered and not in the former, we have plotted on Fig. 4.3 the absolute value of the coefficients in the Gram-Charlier expansion $t(n) = c_n He_n(X/\sigma)$ (resp. $t'(n) = c'_n He_n(X/\upsilon)$) for the distribution before (resp. after) convolution. The case considered here is again the d^6 configuration with a non-convolved standard deviation $\sigma = 79.7$ eV and a convolution parameter $\tau = 20$ eV. Computations have been performed at an arbitrary energy $X = 1$ eV but the results would exhibit the same behaviour for any value of X. One notes that without convolution, the Gram-Charlier series hardly converges since the term $t(900)$ is about 0.02 in absolute value. The strong oscillations visible on this plot correspond to changes in sign and amplitude of both c_n and $He_n(X/\sigma)$ factors. Using the asymptotic form of Hermite polynomials [B59] one can verify that this second factor is indeed an oscillating function of n with increasing amplitude, while the present numerical analysis shows that c_n is an oscillating function with decreasing amplitude. Using two independent numerical methods — quadruple precision Fortran and Mathematica in arbitrary precision — we could verify that oscillations on Fig. 4.3 are not a computational artifact. It appears that the Gram-Charlier expansion converges toward the convolved energy distribution, though slowly if the ratio σ/υ is close to unity. This slow convergence of the Gram-Charlier distribution is reminiscent of the behaviour observed on the $3d^6$-$3d^5 4p$ transition array in bromine by Gilleron and Pain [A76] — though no convolution is then required since the array exhibits coalescence. The Gram-Charlier expansion, though slowly or poorly convergent in some cases, is the simplest form available to check the influence of moments at any order. Other distributions have been proposed but they either involve a reduced set of parameters or give rise to tedious formulas for

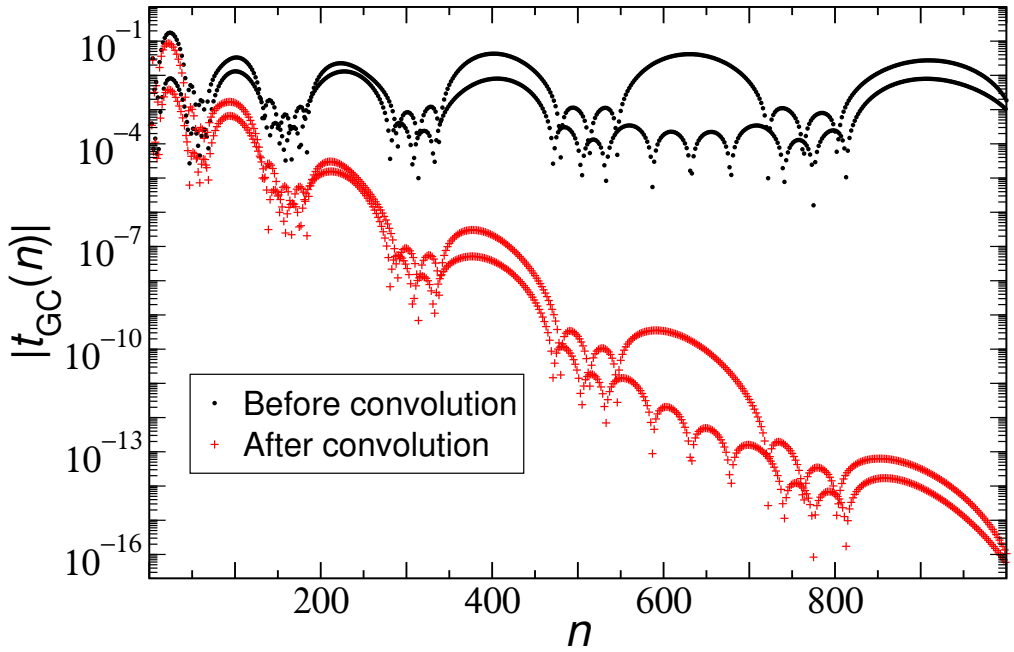

Figure 4.3: Absolute value of the Gram-Charlier term series $c_n He_n(X/\sigma)$ and $c'_n He_n(X/v)$ as a function of n for the d^6 configuration in Au^{+55}. The standard deviation on energy before convolution is $\sigma = 2\xi = 79.7$ eV. The original distribution has been convolved with a Gaussian profile with standard deviation $\tau = 20$ eV. See main text for more details.

defining their parameters as a function of the moments. This is why we restricted the present analysis to such an expansion.

While most of the theoretical effort has been devoted to electric dipole (E_1) transitions, the study of magnetic dipole (M_1) transitions in statistical spectroscopy is rather new. In the following section, M_1-type transitions in tungsten plasmas are investigated in statistical approach using the Flexible Atomic Code (FAC).

4.2 Magnetic dipole transitions in tungsten plasmas

Beyond the electric-dipole (E_1) transitions, Bar-Shalom *et al* [A77] provided formulas for the array widths involving the electric (E_n) and magnetic (M_n) multipole moments at any order, and Pain *et al* [A75] provided expressions for E_2 arrays. Recently it was pointed out by Krief and Feigel [A78] that formulas from Ref. [A77] needed to be corrected. Furthermore, these newly derived expressions have been implemented by the same authors in the FAC code[A30]. Widely used by the community of atomic physics in plasmas, this fully relativistic code is well adapted to the analysis of highly-charged ions of heavy elements, for instance tungsten (W, $Z = 74$), element chosen as plasma facing material in magnetic fusion devices [A54]. Large radiative losses in tungsten could drastically impact the tokamak operation, therefore their accurate calculation, including M_1 effects, is essential [P79]. Radtke *et al* have studied the complex N-shell band structure in W using an electron-beam ion trap [A80]. Several M_1 line

ratios involving highly-charged tungsten ion with an open $3d$ subshell provide reliable diagnostics for determining temperature and density in hot fusion devices [A81].

Owing to the availability of M_1-transition array formulas in FAC, we have studied absorption and emission spectra of W ions with a net charge of about 50, comparing detailed and statistical approaches.

4.2.1 Magnetic and electric dipole transition rates

The influence of lineshapes has been analyzed by comparing detailed or UTA spectra assuming lineshapes given first by Voigt profiles as shown in Eq.(2.76) and then by Gaussian, i.e., canceling the natural width in formulas. The former option leads to profiles behaving as $1/(E-E_{ab})^2$ in the wings, which is much slower than the Gaussian form.

Examples on 0d-emission spectra are given in Figs. 4.4a and 4.4b for E_1 and M_1 transitions respectively.

Considering the E_1 case, in the 0–100 eV region, the Voigt profile differs from the Gaussian profile in both detailed and UTA schemes because there are no transitions. In the region above 740 eV, the UTA Voigt profile significantly differs from the UTA Gauss profile because there are no UTA in this region, while detailed spectra are identical whatever the line profile. As a rule, when the density of lines is sufficient, lineshapes do not affect the spectra.

Accordingly, in the M_1 case illustrated by Fig. 4.4b, the lineshape effect is negligible, because the density of M_1 lines is more homogeneous than the density of E_1 lines.

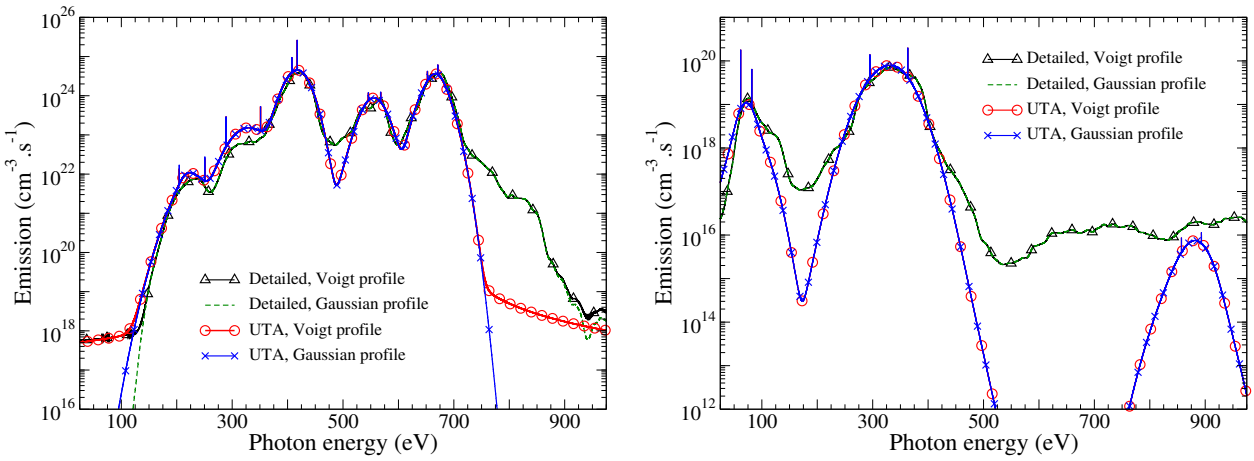

(a) Contribution of E_1 transitions to 0d-emission

(b) Contribution of M_1 transitions to 0d-emission

Figure 4.4: Lineshape effects on the W zero-dimensional emission: Voigt and Gaussian profiles are shown in the detailed and UTA cases, assuming an effective temperature of 180 eV and a density of 10^{14}e/cm^3. The detailed curves are convolved with a 10-eV FWHM response profile. The UTA profiles are not convolved. In the detailed case the convolution is performed using FFT (resp. analytical) method for the Voigt (resp. Gaussian) profiles.

The interest of magnetic dipole transitions [6] can be emphasized considering transition rates. For E_1 lines the transition rate from level b to level a is [B40]

$$A_{ba}(E_1) = \frac{4\alpha a_0^2 E_{ab}^3}{3\hbar^3 c^2 g_b} \left(aJ_a \,\|D\|\, bJ_b\right)^2 \tag{4.43a}$$

where α is the fine-structure constant, a_0 is the Bohr radius, E_{ab} the transition energy, $\hbar$ the quantum of angular momentum, c the speed of light, g_b the statistical weight of the upper level and $(aJ_a \,\|D\|\, bJ_b)$ the dimensionless reduced matrix element of the electric dipole vector in atomic units, such as

$$(aJ_a||D||bJ_b)^2 = \sum_{M_a M_b Q} \left|\left\langle aJ_a M_a \left| D_Q^{(1)} \right| bJ_b M_b \right\rangle\right|^2, \tag{4.43b}$$

$D_Q^{(1)}$ $(Q = 0, \pm 1)$ being the standard tensorial components of the electric dipole. Accordingly, the magnetic-dipole rate is [A82]

$$A_{ba}(M_1) = \frac{\alpha^3 a_0^2 E_{ab}^3}{3\hbar^3 c^2 g_b} \left(aJ_a \,\|M\|\, bJ_b\right)^2 \tag{4.44}$$

where $(aJ_a||M||bJ_b)$ is the reduced matrix element of the vector $\mathbf{M} = \mathbf{L} + 2\mathbf{S}$, $\mathbf{L}$ (resp. $\mathbf{S}$) being the total orbital (resp. spin) angular momentum. In a H-like picture the squared element (4.43b) scales as Z^{-2} if Z is the nucleus charge, while the magnetic moment is Z-independent. This shows that M_1/E_1 rates scale as $Z^2\alpha^2$, assuming analogous transition energies and "ordinary" matrix elements. For non-hydrogenic ions with an effective charge Z_c acting on outer electrons, this ratio is expected to be $\sim Z_c^2\alpha^2$. Therefore, the higher the average charge is, the more important M_1 transitions are.

In order to illustrate the above considerations,we present in Fig. 4.5a and Fig. 4.5b sample computations of the opacity of a tungsten plasma with an effective temperature of 180 eV, which intends to simulate the non-LTE charge distribution of a tokamak plasma. This work being devoted to spectral analysis and averaging procedures rather than to kinetic effects, rather than running NLTE codes, one may use the effective-temperature theory as indicated previously in Eq. 2.58a. Though the effective-temperature dispersion in the Fig. 2.2 looks rather large, we could check that the physical results shown in this work do not change significantly within such a range. Since this work is devoted to spectral analysis and averaging procedures rather than to kinetics effect, the crude approximation on the populations is acceptable with respect to our goal.

The inner K and L shells are filled, as in all other examples in this section. Detailed and UTA computations are plotted on the same graphs. Line shapes are assumed to be given by Voigt profiles, the natural broadening effect arising from bound-bound emission. The very narrow structures observed on the UTA opacity correspond to transition arrays consisting of only one line, with therefore no UTA broadening. To make the detailed-UTA comparison easier, the detailed spectra have been convolved with a Gaussian response function of 10-eV FWHM

[6] The Hamiltonians of electric $E1$ and magnetic $M1$ dipole transitions are given by

$$H_{E1} = e\overrightarrow{r}\,\overrightarrow{E}; \quad H_{M1} = \frac{e\hbar}{2m}(\overrightarrow{l} + \overrightarrow{2s})\,\overrightarrow{B} \tag{4.42}$$

The $E1$ and $M1$ selection rules :
$\Delta J = -1, 0, 1$ (except $0 \to 0$); $\Delta M_J = -1, 0, 1$; Parity change: yes for $E1$-type, non for $M1$-type.

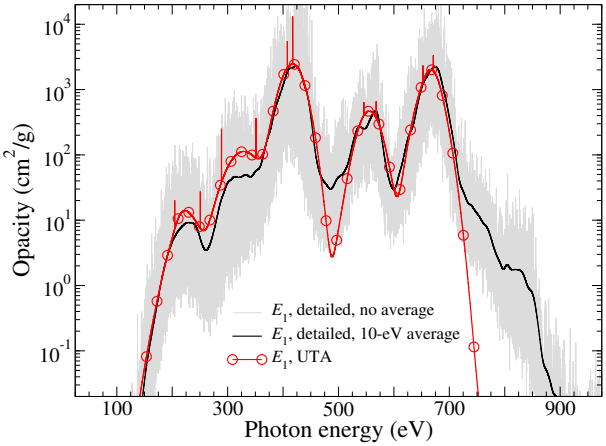

(a) Contribution of electric-dipole transitions to the opacity of a tungsten plasma with an electronic density of 10^{14} e/cm^3 and effective temperature $T_{\text{eff}} = 180$ eV. Ions from W^{49+} to W^{53+} and configurations $1*2\ 2*8\ 3*n$ are accounted for.

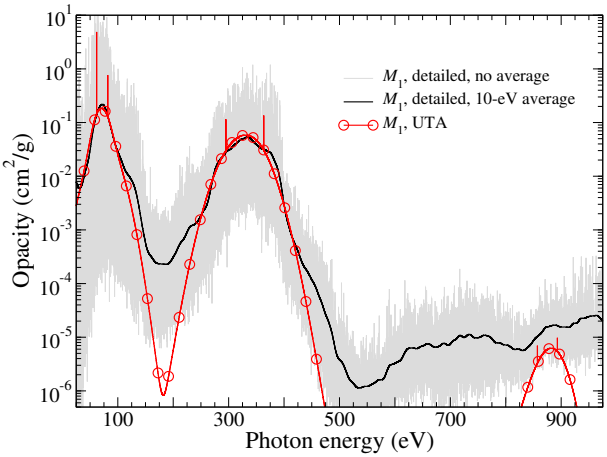

(b) Contribution of magnetic-dipole transitions to the opacity of a tungsten plasma in conditions analogous to those of Fig. 4.5a

Figure 4.5: Opacity in tungsten: electric-dipole and magnetic dipole contributions

using standard fast-Fourier transform (FFT) techniques [B83] and a 131072-point grid. As seen in Fig. 4.5a, except in the 800-eV wing and to a lesser extent close to 500 eV, the UTA formulas reproduce correctly the spectral opacity originating from E_1 transitions. Conversely considering the M_1 contribution shown in Fig. 4.5b, it turns out that the UTA formulas, though reproducing correctly the main structures around 90 eV and 330 eV, are orders of magnitude off when considering the far wings of these structures, e.g., around 650 eV.

Inconsistency between detailed and averaged spectra

Accordingly we show *0-d emission* spectra arising from M_1 transitions in tungsten plasma in Fig. 4.6. Four different charge states are plotted to show that the detailed-UTA discrepancy occurs independently of the ion considered.

4.2.2 Inter- and inner-configuration M1 transitions

In order to check the hypothesis that moments of order above 2 may play a role, the transition-array construction method shown in Sec. 3.2.2 has been applied to the cases analyzed in the previous section, namely the M_1 transitions within $3{*}n$ complex in W^{50+}, W^{51+}, W^{54+} and W^{58+} plasmas. Computing pseudo-UTA moments as explained by Eq. (3.22) up to order $k = 2$, we have been able to build the pseudo-statistical 0d-emission spectra shown as blue lines in Fig. 4.6. It turns out that these averaged spectra exhibit excellent agreement with the detailed spectra. This indicates that the higher-order moments, e.g, asymmetry ($k = 3$) or kurtosis ($k = 4$) [A84, A76], have no significant effect in all these cases. Using the construction method proposed in Sec. 3.2.2, the pseudo-UTAs are counted and compared their number to the number of UTAs from the standard FAC computation. The result is in the last two columns of Table 4.3 for the W ions considered above, where large differences show up. For example, the number of UTAs computed by FAC in the case of W^{50+} is 91, while the corresponding 18513 detailed lines gather in 649 pseudo-arrays. This difference leads us to examine the completeness of the UTA description currently implemented in FAC.

Ion	Levels	RCs	Lines	UTAs in FAC	Pseudo UTAs
W^{50+}	518	60	18513	91	649
W^{51+}	1313	94	93979	157	1520
W^{54+}	6164	187	1200580	352	6675
W^{58+}	2762	131	322827	232	3257

Table 4.3: Number of levels, relativistic configurations (RCs) and M_1 transitions within the complex $3{*}n$ in W^{50+}, W^{53+}, W^{54+}, and W^{58+} ions. Results are from FAC in detailed and UTA mode, that provide the numbers of transitions listed in columns 4 and 5 respectively. The method proposed in this work constructs pseudo-UTAs, counted in column 6, which include much more transitions than the standard UTA computation provided by FAC.

A careful analysis has been carried out on M_1 transitions arising from each pair of configurations in the four tungsten ions considered above. It appears that the detailed lines may be distributed into three categories, according to the corresponding transition occurring between a pair of configurations. These two configurations may be

- distinct and accounted for in FAC computation in UTA mode; such pairs are denoted by *Inter L*

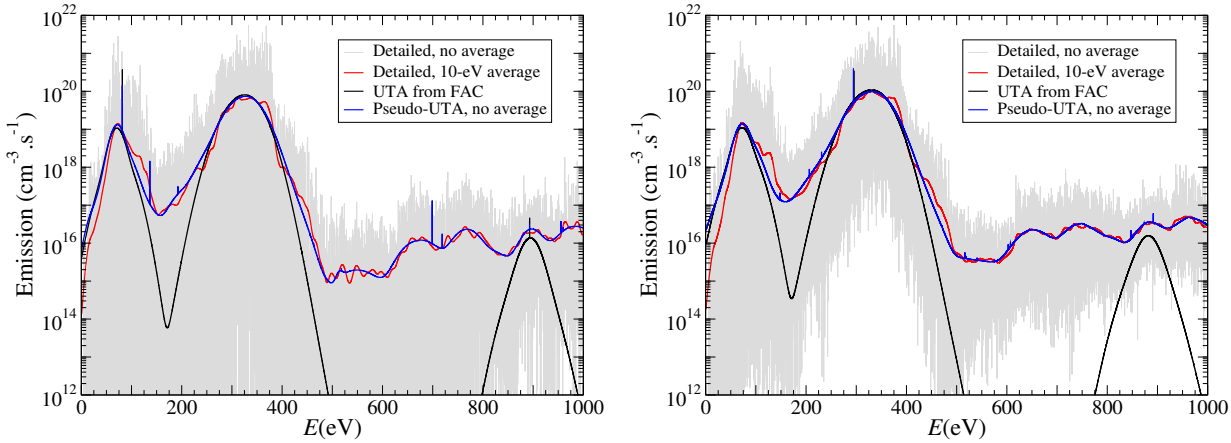

(a) W^{50+} with $3*14$ outer shell

(b) W^{51+} $(3*13)$

(c) W^{54+} $(3*10)$

(d) W^{58+} $(3*6)$

Figure 4.6: Zero-dimensional emission spectra accounting for M_1 transitions within the $3*n$ complex in W^{50+}, W^{51+}, W^{54+}, and W^{58+}, on subfigures 4.6a, 4.6b, 4.6c, and 4.6d respectively. FAC output is post-processed assuming an electron temperature of 200 eV and density of 10^{14} cm^{-3}. The grey line is the detailed computation including Doppler line shapes. The red curves are derived from the detailed computation after convolution by a 10-eV-FWHM response function. The black curves are the spectra obtained using the UTA formulas as provided by FAC. The blue curves are obtained from the detailed computation by collecting lines into pseudo-UTA, see Sec. 3.2.2 for details.

- distinct and not accounted for in FAC computation in UTA mode (*Inter NL*)
- identical and not accounted for in FAC computation in UTA mode (*Inner*).

Thus the missing UTAs are related to the *Inter NL* and *Inner* lines. Concerning the *Inner* transitions, it is worth mentioning that, while inner-configuration processes are not forbidden by M_1 selection rules — with respect to E_1 transition —, the corresponding transitions are absent in the UTA list generated by FAC. Concerning *Inter NL* lines, a deeper insight shows that the UTA computation of FAC does not take into account inter-configurational transitions involving *multiple-electron jumps* such as the 2-electron jumps $3d^2_{3/2} \rightarrow 3d^2_{5/2}$, $3p_{1/2}3d_{5/2} \rightarrow 3p_{3/2}3d_{3/2}$, or even the 3-electron jump $3s_{1/2}3d^2_{3/2} \rightarrow 3p^2_{3/2}3d_{5/2}$. The atomic part of the magnetic-dipole interaction, $\sum_i(\mathbf{l_i} + 2\mathbf{s_i})$ where i runs over all electrons, involves only one-electron operators. However such processes are possible through configuration interaction (CI) effect, which is a complex subject on its own occurring in both cases of E_1- and M_1-type transitions.

Relative contribution of the three categories lines

The contributions of these three categories of lines are represented in Fig. 4.7. The number of lines of each type and their respective contribution to the integrated absorption or emission spectra are listed in Table 4.4.

Ion	*Inter L*	*Inter NL*	*Inner*	Total
W^{50+} (3*14)	5124	12462	927	18513
W^{51+} (3*13)	23912	66239	3828	93979
W^{54+} (3*10)	257672	915807	27101	1200580
W^{58+} (3*6)	73592	242280	6955	322827

(a) Number of lines of each type and total

Ion	*Inter L*	*Inter NL*	*Inner*	Total
W^{50+}	2.52×10^{-5}	5.42×10^{-7}	7.00×10^{-7}	2.65×10^{-5}
W^{51+}	3.05×10^{-5}	1.18×10^{-6}	1.00×10^{-6}	3.27×10^{-5}
W^{54+}	4.76×10^{-5}	4.24×10^{-6}	1.14×10^{-6}	5.30×10^{-5}
W^{58+}	7.93×10^{-5}	6.62×10^{-6}	6.32×10^{-7}	8.66×10^{-5}

(b) Contribution of each type of lines to the dimensionless integrated absorption. The tabulated quantities are $\sum_{ab} p_a f_{ab}$ for each type of transitions.

Ion	*Inter L*	*Inter NL*	*Inner*	Total
W^{50+}	2.74×10^{9}	1.32×10^{8}	5.65×10^{5}	2.87×10^{9}
W^{51+}	3.90×10^{9}	2.94×10^{8}	1.49×10^{6}	4.20×10^{9}
W^{54+}	9.64×10^{9}	1.10×10^{9}	3.20×10^{6}	1.07×10^{10}
W^{58+}	2.30×10^{10}	1.75×10^{9}	1.29×10^{6}	2.47×10^{10}

(c) Contribution of each type of lines to the integrated emission. The tabulated quantities are $\sum_{ab} p_b E_{ab} A_{ba}$, in eV/s, for each type of transitions.

Table 4.4: Number of lines of each type and their integrated contribution to the absorption and emission spectra. See text for details.

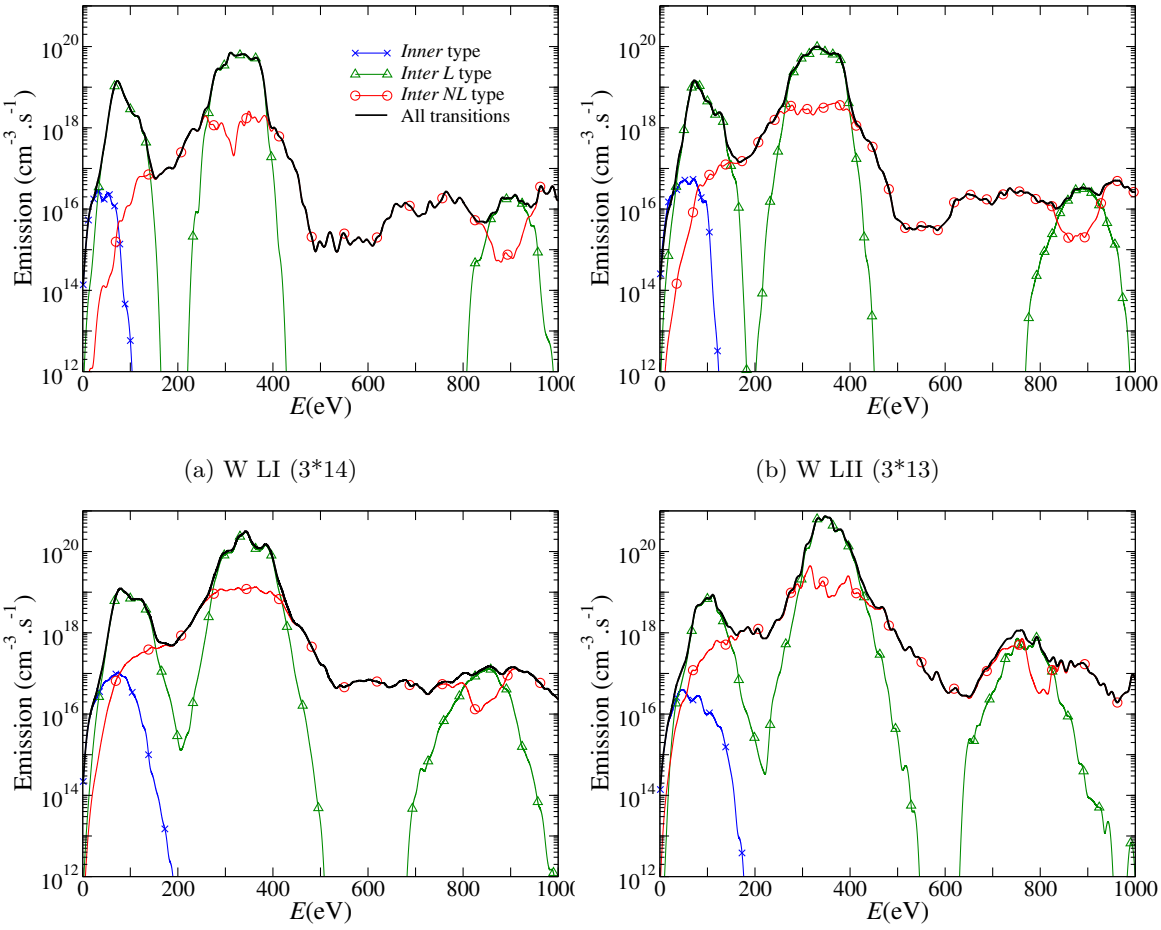

(a) W LI (3*14)

(b) W LII (3*13)

(c) W LV (3*10)

(d) W LIX (3*6)

Figure 4.7: Contribution of the various types of transitions to the emission spectra in W ions. The crosses (blue lines) correspond to transitions within a same relativistic configuration. The triangles (green lines) correspond to inter-configuration transitions present in the list of UTA computed by FAC. The circles (red lines) correspond to inter-configuration transitions not present in this list. The thick black line includes all contributions. Subfigures 4.7a, 4.7b, 4.7c, and 4.7d refer to ions W^{50+}, W^{51+}, W^{54+}, and W^{58+} respectively. All these spectra have been convolved by a 10-eV-FWHM Gaussian profile.

Averaging over the four W ions investigated, *Inter L* transitions represent only 25% of the total number of transitions, whereas the *Inter NL* and *Inner* items represent 70% and 5% respectively. This could lead us to estimate that the UTA formalism from FAC fails in the case of M_1 transitions. However, a more significant comparison concerns the *absorption or emission integrated over energy*. More precisely, we display in Tables 4.4b and 4.4c the *integrated absorption and emission* per ion. Namely, Table 4.4b presents the sum of $V_{\alpha\beta} = \sum_{a\in\alpha b\in\beta} p_a f_{ab}$, and Table 4.4c the corresponding sums for $U_{\alpha\beta} = \sum_{a\in\alpha b\in\beta} p_b A_{ba} E_{ab}$. The sums run on the pairs of configurations $\alpha\beta$ sorted as mentioned above.

It appears that the *Inter NL* lines which represent 70% of the total transition lines as mentioned above account for $\sim 7\%$ of the absorption and emission. Likewise, the *Inner* lines account for less than 3% of the integrated absorption and emission. Their weak contribution to the emission is due to the fact that the energy difference between levels inside a same configuration is usually small and that emission rates scale as E_{ab}^4. As mentioned above, the *Inter NL* lines correspond in most cases to transitions with multiple electron jumps which are allowed only through CI. Though such lines are numerous since many configurationg mixing schemes are possible, their overall contribution to absorption or emission remain limited in the present case.

In term of spectral dependency, each of these three transition categories appears in specific regions as shown on Fig. 4.7. The low-energy range (below 100 eV) is occupied by *Inner* transitions, as expected. The *Inter L* transitions are dominant in the 70 eV and 350 eV regions — and to a lesser extent 900 eV — which correspond to the maximum emission probability. Finally the *Inter NL* are present in regions (150–200 eV, 450–800 eV) where the most important discrepancy was observed between detailed and UTA computation by FAC in Fig. 4.6.

Chapter 5

Conclusion

> Nothing in life is to be feared, it is only to be understood.
> Now is the time to understand more [...]
>
> Marie Sklodowska-Curie

Summary

Within the framework of statistical spectroscopy, two features of highly ionized plasmas are considered, namely the increasing importance of spin-orbit effect with respect to Coulomb interaction, and of M_1-type transitions with respect to E_1. This thesis relies on mathematical methods developed by the Bauche *et al*, as well as numerical analysis based on recent developments around the Flexible Atomic Code, with a special focus on the calculation of distribution moments.

- The 1st and 2nd quantization techniques, together with angular momentum algebra have been applied to derive analytical expressions of configuration averages. High-order moments for the spin-orbit energy in a N-electron system are determined and put to computation tests with success : excellent agreement is found between the computed averages and numerical data from Cowan's code, and convergence of the Gram-Charlier expansion built with moments of spin-orbit energy is observed when a suitable convolution procedure is performed.
- Absorption and emission spectra arising from magnetic dipole transitions in hot tungsten plasmas have been investigated using the FAC code. A pseudo-UTA method has been constructed and applied in the post-processing procedure. It is demonstrated that the recent UTA formulas for M_1 transition arrays is limited. 2 categories of lines are missing : from inner-configurational transitions – specific to magnetic type, as well as from inter-configurational transitions due to configuration mixing effect.

Of course, it would be better if the above results could have been compared to experimental data. [1] Possible collaboration projects may be pursued later on, when opportunities arise.

[1] We have attempted to establish research collaborations on tungsten spectroscopy project with the team of M.G.O'Mullane from the University of Strathclyde – member of ADAS (Atomic Data and Analysis Structure) organisation, unfortunately in vain by lack of a common timetable.

While positioning in the overall areas of the statistical properties of complex atomic spectra, the author is aware that the present thesis more likely touched upon this large topic. For instance, the corrections at low temperatures for line modelling in a transition array have not been considered, neither some general properties such as propensity rule nor generalized J-file sum rule [A85][P61].

Perspectives

In what follows, for the purposes of contributing to forbidden-line spectroscopy, one may develop UTA formulas for inner-configurational transitions – possibly using the analytical techniques applied in the derivation of spin-orbit averages. Furthermore, a deeper insight can be given into configuration interaction involved in inter-configurational transitions, as well as the issue of plasma temperature in moments derivation.

In terms of numerical work, the FAC code is mostly considered in this thesis as a support for our theoretical understanding, rather than a subject of study on its own. However, even without exploring the large number of functions available for various radiative and collisional processes computations, useful when plasmas are considered in NLTE conditions, the FAC code retains a strong growth potential, for instance, *parallelized* calculations (eg. per ion or per configuration) may represent an interesting development path to follow. Together with the ongoing implementation tests of detailed-statistical hybrid models [A86][A87], more statistical options – STA, PRTA (Partially Resolved Transition Array) [A88], etc. – may be considered, which would provide FAC a wider range of applicability.

Appendices

Appendix A

Systems of units

Although the International System of Units (SI) was approved as the official system of measurement in the 1960s, the use of variants of the metric system can be mainstream and more convenient in a given area of study. For instance, the CGS system is commonly adopted in theoretical physics, which is based on measuring lengths in centimetres (cm), mass in grams (g), and time in seconds (s). While the MKS system, standing for meter-kilogram-second system of units, is widely used in engineering and physics instruction [W89].

In order to guarantee the correctness in computer programming, it is important to ensure the consistency of units used for various quantities in the implemented formulas. Otherwise, the gap among numerical values can be of large orders of magnitude.

By way of illustration, let's give some examples of units frequently associated to energy and temperature.

- Energy (J, erg, eV)
  In the CGS system, energy values are expressed in erg, where

$$1 \text{ erg } = 10^{-7} \text{ J} . \tag{A.1}$$

  In atomic physics, it is customary to use the Rydberg unit of energy,

$$1 \text{ Ry } = 13.605693009(84) \text{ eV} , \tag{A.2}$$

  with

$$1 \text{ eV } = 1.602176487(40) \times 10^{-19} \text{ J} . \tag{A.3}$$

  Actually, such units are constructed from experimental values [1] with the standard uncertainty in the last digits given in parenthesis. Namely, 1 Ry corresponds to the ionization energy of the hydrogen atom, 1 eV is the kinetic energy acquired by an electron in passing through a potential difference of 1 V in vacuum [O90].

- Temperature (K, °C, eV)
  The SI unit of temperature is Kelvin, denoted by K. Celsius temperature t (°C) is defined

[1] Other noteworthy examples can be found in the reference booklet [O90]. For instance, the astronomical unit (ua) is approximately equal to the mean Earth-Sun distance, 1 ua = $1.49597870691(6) \times 10^{11}$ m; the unified atomic mass unit (u) is equal to 1/12 times the mass of a free carbon 12 atom, at rest and in its ground state, 1 u = $1.660538782(83) \times 10^{-27}$ kg.

in terms of thermodynamic temperature T (K) by the equation

$$t = T - T_0, \tag{A.4}$$

where $T_0 = 273.15$ K by definition. It is customary to express plasmas temperatures through their equivalent thermal energies, therefore, the Boltzmann constant k_B[W91]

$$k_B = 8.6173303(50) \times 10^{-5} \text{eV/K}, \tag{A.5}$$

may not appear in formulas.

Hartree atomic units

In this thesis, the preference is given to the Hartree atomic units (a.u.), where [B41]

- the unit of mass is that of the electron :

$$m_e \approx 9.109 \times 10^{-31} \text{ kg} , \tag{A.6}$$

- the unit of charge is that of the proton :

$$e \approx 1.602 \times 10^{-19} \text{ C} , \tag{A.7}$$

- the unit of length is the Bohr radius :

$$a_0 = \frac{4\pi\epsilon_0\hbar^2}{m_e e^2} \approx 5.292 \times 10^{-11} \text{ m} , \tag{A.8}$$

- the unit of energy is the Hartree energy :

$$E_h = \frac{e^2}{4\pi\epsilon_0 a_0} = \alpha^2 m_e c^2 \approx 4.360 \times 10^{-18} \text{ J } \approx 27.211 \text{ eV} , \tag{A.9}$$

where the fine structure constant

$$\alpha = \frac{e^2}{4\pi\epsilon_0\hbar c} \approx \frac{1}{137.036} \tag{A.10}$$

- the unit of time :

$$\tau = \frac{\hbar}{E_h} \approx 2.419 \times 10^{-17} \text{ s} . \tag{A.11}$$

Notably, [2].

$$e = 1, \quad \hbar = 1, \quad m_e = 1 \tag{A.12}$$

quantities like elementary charge e, etc. are set up as of dimension one and are expressed simply as numbers, and the speed of light in vacuum is linked to α as $c = \alpha^{-1}$.

[2] 1 a.u. of permittivity is $4\pi\epsilon_0 = 1.113 \times 10^{-10}$ C$^2 \cdot$J$^{-1} \cdot$m^{-1}. 1 a.u. of action is $\hbar = 1.0546 \times 10^{-34}$ J$\cdot$s. In the SI, the value of the velocity of light in vacuum is $c = 299\ 792\ 458$ m/s exactly [O90].

Appendix B

Angular momentum in atomic system

As a conservative quantity of system [1], angular momentum is fundamental in theoretical studies of atomic structure and transitions. For instance, *selection rules* for radiative transitions between levels are governed by angular momentum *addition rules* [B42].

B.1 Angular momentum

B.1.1 Classical and quantum angular momenta

It is well known that in classic mechanics, a particle moving with linear momentum p at a position r with respect to a given reference point has an orbital angular momentum L, defined by

$$L = r \times p. \tag{B.1}$$

In quantum mechanics, the corresponding angular momentum *operator* – in the case of one neutral particle without spin – can be obtained by expressing p as a function of the ∇ operator such as

$$p = -i\hbar\nabla, \quad L = -i\hbar[r \times \nabla]. \tag{B.2}$$

Compared to angular momenta in classic mechanics for rotating systems, angular momentum operators applied to atomic structure exhibit notable quantization and spin-related features.

- Similarly to quantized atomic level energies in the *Bohr model* of the atom, angular momenta in quantum physics do not vary continuously, but only have allowed discrete values involving Planck constant h ($h = 4 \cdot 10^{-15}$eV$\cdot s$).

- Accounting for the intrinsic spin 1/2 (in units of $\hbar$) of each electron, spin angular momentum represented by spin operator S constitutes an additional angular momentum with respect to a classical particle. Therefore, the conservation of angular momentum in quantum mechanics applies to the total angular momentum $J = L + S$, but not to L (or S). For example, the spin-orbit interaction as shown in Eq. (2.3) allows transfers of angular momentum between L and S while their sum remains constant.

[1] *Noether's theorem* proves that angular momentum is conserved whenever physical laws are rotationally invariant.

B.1.2 Characteristics of angular momentum operators

The fact that an electron is commonly characterized by the sets of quantum numbers [2] $\{nlm_l m_s\}$ (resp. $\{nljm\}$) is not insignificant. Actually, one-electron wave functions as defined in Eqs. (2.13)(2.14) are eigenfunctions of the one-electron angular and spin momentum operators $\{L^2, L_z, S^2, S_z\}$ (resp.$\{L^2, L_z, J, J_z\}$) which constitute a complete set of commuting observables (CSCO). A CSCO is a set of compatible observables $\{O_1, O_2, ...\}$ among which each pair commutes

$$[O_a, O_b] = O_a O_b - O_b O_a = 0, \tag{B.3}$$

and the number of operators involved or of quantum numbers related to the eigenvalues of these operators is such that each physical state is fully characterized by them.The commutation relation in Eq. (B.3) means that the order of measurement has no effect on the final eigenvalue result, so that different observables may be measured simultaneously. Moreover, a common set of basis states exits of which any state of the system can be expressed as a linear combination.

Angular momentum operators are self-adjoint operators j_x, j_y, j_z that satisfy the following commutation relation

$$[j_a, j_b] = j_a j_b - j_b j_a = \epsilon_{abc} i\hbar j_c, \tag{B.4}$$

where $(a, b, c) = \{x, y, z\}$ and ϵ_{abc} denoting a permutation symbol with

$$\epsilon_{abc} = \begin{cases} 1, & \text{in the case of circular permutation of } (a,b,c) \\ 0, & \text{otherwise.} \end{cases} \tag{B.5}$$

Furthermore, operators defined as

$$j_\pm = j_x \pm i j_y \tag{B.6a}$$

$$j^2 = j_x^2 + j_y^2 + j_z^2 = j_+ j_- + j_z^2 - j_z = j_- j_+ + j_z^2 + j_z \tag{B.6b}$$

are widely used, which satisfy commutation relations

$$\left[j^2, j_\pm\right] = 0, \quad \left[j^2, j_z\right] = 0. \tag{B.6c}$$

[2] Recall that quantum numbers are discrete sets of integers and half-integers used to describe quantized observable quantities.

- the principal quantum number : $n = 1, 2, ...$
- the orbital (or azimuthal) quantum number : $l = 0, 1, ..., n-1$
- the orbital projection (or magnetic) quantum number : $m_l = -l, -l+1, ..., l-1, l$
- the spin quantum number : $s = \frac{1}{2}$
- the spin projection quantum number : $m_s = -\frac{1}{2}, \frac{1}{2}$
- the total angular momentum quantum number : $j = |l \pm s| = |l \pm \frac{1}{2}|$
- the total angular momentum projection quantum number : $m_j \equiv m = -j, -j+1, ..., j-1, j$

For instance, denoting $|jm\rangle$ the eigenstates of $\{j^2, j_z\}$ where j may stand for L, S, J, the following eigenvalue equations are of great use in the matrix calculation :

$$\boldsymbol{j^2} \mid jm\rangle = \hbar^2 j(j+1) \mid jm\rangle, \quad j = \{0, \frac{1}{2}, 1, \frac{3}{2}, ...\}; \tag{B.7a}$$

$$\boldsymbol{j_z} \mid jm\rangle = \hbar m \mid jm\rangle, \quad m = \{-j, -j+1, ..., j-1, j\}; \tag{B.7b}$$

$$\boldsymbol{j_\pm} \mid jm\rangle = \hbar c_\pm(j,m) \mid j(m\pm 1)\rangle \quad c_\pm(j,m) = \sqrt{j(j+1) - m(m\pm 1)} \tag{B.7c}$$

As examples of angular momentum operators,

- In the case of $j = L$, the simultaneous eigenfunctions of $\{L^2, L_z\}$ are called *spherical harmonics* $Y_{m_l}^{(l)}(\theta, \phi)$. They are linked to their adjoints by the relation such as

$$Y_{-m_l}^{(l)}(\theta, \phi) = (-1)^m Y_{m_l}^{*(l)}(\theta, \phi). \tag{B.8a}$$

  Explicit values can be derived, for examples

$$Y_0^{(0)} \equiv Y_{00} = \sqrt{\frac{1}{4\pi}}, \quad Y_0^{(1)} \equiv Y_{10} = \sqrt{\frac{3}{4\pi}} cos\theta. \tag{B.8b}$$

- If $j = S$, the simultaneous eigenstates of $\{S^2, S_z\}$ are called *spinors* $\chi_\nu, (\nu = \pm 1/2)$ which are 2-component vectors $\chi_{1/2} = \begin{pmatrix} 1 \\ 0 \end{pmatrix}$, $\chi_{-1/2} = \begin{pmatrix} 0 \\ 1 \end{pmatrix}$. In the space spanned by χ_ν, spin operators can be represented as 2x2 matrices such as :

$$S^2 = \frac{3}{4}\hbar^2 \begin{pmatrix} 1 & 0 \\ 0 & 1 \end{pmatrix}, \quad S_z = \frac{1}{2}\hbar \begin{pmatrix} 1 & 0 \\ 0 & -1 \end{pmatrix}, \quad S_+ = \hbar \begin{pmatrix} 0 & 1 \\ 0 & 0 \end{pmatrix}, \quad S_- = \hbar \begin{pmatrix} 0 & 0 \\ 1 & 0 \end{pmatrix} \tag{B.9}$$

  It is common to represent S operator as a function of *Pauli matrices* σ defined by :

$$\sigma_x = \begin{pmatrix} 0 & 1 \\ 1 & 0 \end{pmatrix}, \quad \sigma_y = \begin{pmatrix} 0 & -i \\ i & 0 \end{pmatrix}, \quad \sigma_z = \begin{pmatrix} 1 & 0 \\ 0 & -1 \end{pmatrix} \tag{B.10}$$

  so that $S = \frac{1}{2}\hbar\sigma$.

B.2 Clebsch-Gordan coefficients and 3j symbols

As expansion coefficients in basis changes, the Clebsch-Gordan coefficients or their closely related Wigner 3j symbols arise from angular momentum coupling.

Clebsch-Gordan coefficients

When using a two-electron product function $|j_1 m_1\rangle|j_2 m_2\rangle \equiv |j_1 j_2 m_1 m_2\rangle$ to form its coupled function $|j_1 j_2 jm\rangle$ – eigenfunction of $\{J_1^2, J_2^2, J^2 \equiv (J_1 + J_2)^2, J_z \equiv J_{1z} + J_{2z}\}$, it turns out that

$$|j_1 j_2 jm\rangle = \sum_{m_1=-j_1}^{j_1} \sum_{m_2=-j_2}^{j_2} C(j_1 j_2 m_1 m_2; jm) |j_1 j_2 m_1 m_2\rangle \tag{B.11}$$

where $C(j_1 j_2 m_1 m_2; jm) = \langle j_1 j_2 m_1 m_2 \,|\, jm \rangle$ are Clebsch-Gordan coefficients.

Similarly, coupled basis $|\, nljm\rangle$ and uncoupled basis $|\, nlm_l m_s\rangle$ are linked by Clebsch-Gordan coefficients $C(lsm_l m_s; jm) = \langle lsm_l m_s \,|\, jm\rangle$ as

$$|\, nljm\rangle = \sum_{m_l m_s} C(lsm_l m_s; jm)\, |\, nlm_l m_s\rangle \tag{B.12}$$

Wigner 3j symbols

Symmetry properties of the Clebsch-Gordan coefficients are made more straigntforward by introducing the Wigner 3j symbols [B42], which are algebraic functions with 6 arguments [B40]

$$\begin{pmatrix} j_1 & j_2 & j_3 \\ m_1 & m_2 & -m_3 \end{pmatrix} = \frac{(-1)^{j_1 - j_2 + m_3}}{\sqrt{2j_3 + 1}} C(j_1 j_2 m_1 m_2; j_3 m_3) \tag{B.13}$$

nonvanishing only if $m_1 + m_2 - m_3 = 0$.
For example, the Clebsch-Gordan coefficients in Eq. (B.12) can be expressed in terms of the 3j symbols as

$$C(lsm_l m_s; jm) = (2j+1)^{1/2} (-1)^{l-s+m} \begin{pmatrix} l & s & j \\ m_l & m_s & -m \end{pmatrix} \tag{B.14}$$

General expressions of $C(j_1 j_2 m_1 m_2; jm)$ and the 3j symbols can be found in [B42][B40]. Nevertheless, they are too cumbersome to be applied. In practice, built-in routines in Mathematica as well as in Fortran can be used to evaluate the Clebsch-Gordan coefficients and the 3j symbols.

Properties

Despite their cumbersome expressions, high symmetry properties of the 3j symbols are of great use for explicit analytical calculation in angular momentum coupling.

- Symmetry under interchange of columns :
  - symmetric under even (circular) permutation of the indices (123) :

$$\begin{pmatrix} j_1 & j_2 & j_3 \\ m_1 & m_2 & m_3 \end{pmatrix} = \begin{pmatrix} j_2 & j_3 & j_1 \\ m_2 & m_3 & m_1 \end{pmatrix} = \begin{pmatrix} j_3 & j_1 & j_2 \\ m_3 & m_1 & m_2 \end{pmatrix} \tag{B.15}$$

  - change by a phase under odd permutation of (123) :

$$\begin{pmatrix} j_2 & j_1 & j_3 \\ m_2 & m_1 & m_3 \end{pmatrix} = (-1)^{j_1 + j_2 + j_3} \begin{pmatrix} j_1 & j_2 & j_3 \\ m_1 & m_2 & m_3 \end{pmatrix} \tag{B.16}$$

- Change the sign of m_1, m_2, m_3 :

$$\begin{pmatrix} j_1 & j_2 & j_3 \\ -m_1 & -m_2 & -m_3 \end{pmatrix} = (-1)^{j_1 + j_2 + j_3} \begin{pmatrix} j_1 & j_2 & j_3 \\ m_1 & m_2 & m_3 \end{pmatrix} \tag{B.17}$$

  which is equivalent to the previous equation.

- Orthogonality relations :

$$\sum_{m_1,m_2} \begin{pmatrix} j_1 & j_2 & j_3' \\ m_1 & m_2 & m_3' \end{pmatrix} \begin{pmatrix} j_1 & j_2 & j_3 \\ m_1 & m_2 & m_3 \end{pmatrix} = \frac{1}{2j_3+1} \delta_{j_3 j_3'} \delta_{m_3 m_3'} \tag{B.18}$$

$$\sum_{j_3,m_3} (2j_3+1) \begin{pmatrix} j_1 & j_2 & j_3 \\ m_1 & m_2 & m_3 \end{pmatrix} \begin{pmatrix} j_1 & j_2 & j_3 \\ m_1' & m_2' & m_3 \end{pmatrix} = \delta_{m_1 m_1'} \delta_{m_2 m_2'} \tag{B.19}$$

Appendix C

Average calculations of product $V_{\mathbf{ee}}V_{\mathbf{so}}^2$ operators

Context

Within the framework of statistical spectroscopy, one may analyze the interaction energy in Eq.(4.2) at the 3rd order, whose Hamiltonian reads

$$(H^{'})^3 = (V_{\mathrm{ee}} + V_{\mathrm{so}})^3 \tag{C.1}$$

In terms of average values, the matrix elements can be decomposed into four parts [1]:

$$\left\langle (H^{'})^3 \right\rangle = \left\langle V_{\mathrm{ee}}^3 \right\rangle + 3\left\langle V_{\mathrm{ee}}^2 V_{\mathrm{so}} \right\rangle + 3\left\langle V_{\mathrm{ee}} V_{\mathrm{so}}^2 \right\rangle + \left\langle V_{\mathrm{so}}^3 \right\rangle. \tag{C.2}$$

1. For symmetry reason, $\langle V_{\mathrm{ee}}^2 V_{\mathrm{so}} \rangle = 0$.

2. The derivation of $\langle V_{\mathrm{ee}}^3 \rangle$ is a lengthy process. The result of the centered moment $\mu_3^c(V_{\mathrm{ee}})$ was firstly published by Kučas and Karazija [A67]. Some partial checks of Kučas and Karazija's formula for $\langle V_{\mathrm{ee}}^3 \rangle$ have been performed, a sign error was found out and the correct formula was published, cf. Eq.(B3) in [A32].

3. The spin-orbit effects at any order $\left\langle V_{\mathrm{so}}^k \right\rangle$ have been discussed in Sec.4.1, the result of $\langle V_{\mathrm{so}}^3 \rangle$ is shown in Eq.(4.18).

[1] Actually, the combination of V_{so} at the 2nd order and V_{ee} at the 1st order in H_{int}^3 is equal to $V_{\mathrm{ee}}V_{\mathrm{so}}^2 + V_{\mathrm{so}}V_{\mathrm{ee}}V_{\mathrm{so}} + V_{\mathrm{so}}^2 V_{\mathrm{ee}}$. However, due to properties of a matrix trace, $\left\langle V_{\mathrm{ee}}V_{\mathrm{so}}^2 \right\rangle = \langle V_{\mathrm{so}}V_{\mathrm{ee}}V_{\mathrm{so}} \rangle = \left\langle V_{\mathrm{so}}^2 V_{\mathrm{ee}} \right\rangle$.

C.1 Product operator $V_{\rm ee}V_{\rm so}^2$

By definitions of $V_{\rm ee}$ and $V_{\rm so}$ operators, their product operator $V_{\rm ee}V_{\rm so}^2$ can be developed as

$$V_{\rm ee}V_{\rm so}^2 = \left(\sum_{i<j}\frac{1}{r_{ij}}\right)\left(\sum_p \xi_p l_p s_p\right)^2 \tag{C.3a}$$

$$= \left(\sum_{i<j}\frac{1}{r_{ij}}\right)\left(\sum_p \xi_p^2 (l_p s_p)^2 + 2\sum_{p<q}\xi_p\xi_q (l_p s_p)(l_q s_q)\right) \tag{C.3b}$$

$$= \sum_{i<j}\sum_p \frac{1}{r_{ij}}\xi_p^2 (l_p s_p)^2 + 2\sum_{i<j}\sum_{p<q}\frac{1}{r_{ij}}\xi_p\xi_q (l_p s_p)(l_q s_q) \tag{C.3c}$$

where depending on various possible (p,q) values related to (i,j), the sum can be split as

- $$\sum_{i<j}\sum_p \frac{1}{r_{ij}}\xi_p^2 (l_p s_p)^2 = \sum_{\substack{i<j\\ p=i}}\frac{1}{r_{ij}}\xi_i^2 (l_i s_i)^2 + \sum_{\substack{i<j\\ p=j}}\frac{1}{r_{ij}}\xi_j^2 (l_j s_j)^2 + \sum_{\substack{i<j\\ p\neq(i,j)}}\frac{1}{r_{ij}}\xi_p^2 (l_p s_p)^2 \tag{C.4}$$

- $$\begin{aligned} 2\sum_{i<j}\sum_{p<q}\frac{1}{r_{ij}}\xi_p\xi_q (l_p s_p)(l_q s_q) = {} & 2\sum_{\substack{i<j\\ p=i,q=j}}\frac{1}{r_{ij}}\xi_i\xi_j (l_i s_i)(l_j s_j) + 2\sum_{i<j}\sum_{\substack{p<q\\ p,q\neq(i,j)}}\frac{1}{r_{ij}}\xi_p\xi_q (l_p s_p)(l_q s_q) \\ & + 2\sum_{\substack{i<j\\ p=i}}\sum_{q>i}\frac{1}{r_{ij}}\xi_i\xi_q (l_i s_i)(l_q s_q) + 2\sum_{\substack{i<j\\ p=j}}\sum_{q>j}\frac{1}{r_{ij}}\xi_j\xi_q (l_j s_j)(l_q s_q) \\ & + 2\sum_{\substack{i<j\\ q=i}}\sum_{p<i}\frac{1}{r_{ij}}\xi_p\xi_i (l_p s_p)(l_i s_i) + 2\sum_{\substack{i<j\\ q=j}}\sum_{p<j}\frac{1}{r_{ij}}\xi_p\xi_j (l_p s_p)(l_j s_j). \end{aligned} \tag{C.5}$$

The various terms in the sums above can be regrouped into 3 categories W_k, characterized by the number of particles k involved in each operator. One gets

$$\boxed{\mathrm{Tr}V_{\rm ee}V_{\rm so}^2 = \mathrm{Tr}W_2 + \mathrm{Tr}W_3 + \mathrm{Tr}W_4} \tag{C.6}$$

Separations into k-particle operators : $W_k (k = 2,3,4)$

W_2=2-particle operator:

$$W_2 = \sum_{i<j}\frac{1}{r_{ij}}\xi_i^2 (l_i s_i)^2 + \sum_{i<j}\frac{1}{r_{ij}}\xi_j^2 (l_j s_j)^2 + 2\sum_{i<j}\frac{1}{r_{ij}}\xi_i\xi_j (l_i s_i)(l_j s_j) \tag{C.7a}$$

$$= \frac{1}{2}\sum_i\sum_j\left(\frac{1}{r_{ij}}\xi_i^2 (l_i s_i)^2 + \frac{1}{r_{ij}}\xi_j^2 (l_j s_j)^2 + 2\frac{1}{r_{ij}}\xi_i\xi_j (l_i s_i)(l_j s_j)\right) \tag{C.7b}$$

W_3=3-particle operator, can be divided into 2 parts, depending on whether $(l_i s_i), (l_j s_j)$ product is squared S or crossed C, so that $\langle W_3\rangle = \langle S\rangle + \langle C\rangle$:

- as,

$$\sum_{i<j}\sum_{p} = \left\langle \sum_{i<j<p} + \sum_{i<p<j} + \sum_{p<i<j} \Rightarrow 3\left(\frac{1}{6}\sum_{i}\sum_{j}\sum_{p}\right) \right. \tag{C.8}$$

so,

$$S = \sum_{i<j}\sum_{p}\frac{1}{r_{ij}}\xi_p^2(l_p s_p)^2 \Rightarrow \frac{1}{2}\sum_{i}\sum_{j}\sum_{p}\frac{1}{r_{ij}}\xi_p^2(l_p s_p)^2 \tag{C.9}$$

-

$$\begin{aligned} C = 2\times \sum_{i<j<q}\left(\frac{1}{r_{ij}}\xi_i\xi_q(l_i s_i)(l_q s_q) + \frac{1}{r_{ij}}\xi_j\xi_q(l_j s_j)(l_q s_q)\right) \\ +2\times \sum_{p<i<j}\left(\frac{1}{r_{ij}}\xi_i\xi_p(l_i s_i)(l_p s_p) + \frac{1}{r_{ij}}\xi_j\xi_p(l_j s_j)(l_p s_p)\right) \\ +2\times\left(\sum_{i<p<j}\frac{1}{r_{ij}}\xi_j\xi_p(l_j s_j)(l_p s_p) + \sum_{i<q<j}\frac{1}{r_{ij}}\xi_i\xi_q(l_i s_i)(l_q s_q)\right) \end{aligned} \tag{C.10a}$$

$$\begin{aligned} \Rightarrow \frac{1}{3}\sum_{i}\sum_{j}\sum_{p}\left(\frac{1}{r_{ij}}\xi_i\xi_p(l_i s_i)(l_p s_p) + 2\frac{1}{r_{ij}}\xi_j\xi_p(l_j s_j)(l_p s_p)\right) \\ +\frac{1}{3}\sum_{i}\sum_{j}\sum_{q}\left(\frac{1}{r_{ij}}\xi_j\xi_q(l_j s_j)(l_q s_q) + 2\frac{1}{r_{ij}}\xi_i\xi_q(l_i s_i)(l_q s_q)\right) \end{aligned} \tag{C.10b}$$

because of the indistinguishability of electrons, $p = q$, thus

$$C = \sum_{i}\sum_{j}\sum_{p}\left(\frac{1}{r_{ij}}\xi_i\xi_p(l_i s_i)(l_p s_p) + \frac{1}{r_{ij}}\xi_j\xi_p(l_j s_j)(l_p s_p)\right) \tag{C.10c}$$

W_4=4-particle operator: as,

$$\sum_{i<j}\sum_{p<q} = \sum_{i<j<p<q} + \sum_{i<p<j<q} + \sum_{i<p<q<j} + \sum_{p<i<j<q} + \sum_{p<i<q<j} + \sum_{p<q<i<j} \Rightarrow 6\times\left(\frac{1}{24}\sum_{i}\sum_{j}\sum_{p}\sum_{q}\right) \tag{C.11}$$

so:

$$W_4 = 2\times\sum_{i<j}\sum_{p<q}\frac{1}{r_{ij}}\xi_p\xi_q(l_p s_p)(l_q s_q) = \frac{1}{2}\sum_{i}\sum_{j}\sum_{p}\sum_{q}\frac{1}{r_{ij}}\xi_p\xi_q(l_p s_p)(l_q s_q) \tag{C.12}$$

C.2 Evaluation of matrix elements $\left\langle V_{\rm ee} V_{\rm so}^2 \right\rangle$

Following the Eq. C.6 and remind that according to the Uylings' theorem (cf.Eq.(4.4)), the number of electrons to take into account in the basis states of a W_k operator can be restricted to k, this section shows calculations of matrix elements $\langle W_k \rangle \quad (k = 2,3,4)$ for a $(nl)^k$ configuration in their respective $k-$particle coupled basis. The radial part for the considered subshell $\langle \xi_i \rangle^k = \langle nl\,|\xi(r)|\,nl\rangle^k$ is a common factor in all these formulas and will be dropped unless mentioned. In

order to shorten the formulas derived, let's take two notations as following

$$x(j_1,j_2,l) = \left(j_1^2 + j_1 + j_2^2 + j_2 - 2(l^2+l+\frac{3}{4})\right)^2 \tag{C.13a}$$

$$X_k = (2l+1)^2 \begin{pmatrix} l & k & l \\ 0 & 0 & 0 \end{pmatrix}^2 F^{(k)}(ll) = \left(l \left\| C^{(k)} \right\| l\right)^2 F^{(k)}(ll) \tag{C.13b}$$

where X_k is the product of the squared reduced matrix element $\left(l \left\| C^{(k)} \right\| l\right)^2$ and of the $F^{(k)}(ll)$ Slater integral [B40].

C.2.1 Average of a 2-electron operator : $\langle W_2 \rangle$

In a two-particle coupled basis $|12\rangle_{jm}$, 2! permutation states are involved in the matrix element calculation $\langle W_2 \rangle_2$. The average of configuration $(nl)^2$ is given by:

$$\langle W_2 \rangle_2 = \frac{1}{g_2} \sum_P (-1)^\tau \langle 12|W_2|\tau(1)\tau(2)\rangle = \frac{1}{g_2}(\langle 12|W_2|12\rangle - \langle 12|W_2|21\rangle) \tag{C.14}$$

where P, τ stand for permutations, and the degeneracy g_2 such as

$$\frac{1}{g_2} = \begin{pmatrix} 4l+2 \\ 2 \end{pmatrix}^{-1} = \frac{2}{(1+4l)(2+4l)}. \tag{C.15}$$

With respect to Eq.(C.7a), the matrix element $\langle W_2 \rangle$ can be decomposed by squared terms like $\left\langle \frac{1}{r_{ij}}(l_k s_k)^2 \right\rangle$ and crossed term $\left\langle \frac{1}{r_{ij}}(l_i s_i)(l_j s_j) \right\rangle$ such as :

$$\left\langle \frac{1}{r_{ij}}(l_k s_k)^2 \right\rangle = \left\langle ij|\frac{1}{r_{12}}|ij \right\rangle \left\langle k|(ls)^2|k \right\rangle - \left\langle ij|\frac{1}{r_{12}}|ji \right\rangle \left\langle k'|(ls)^2|k' \right\rangle \tag{C.16a}$$

$$\left\langle \frac{1}{r_{ij}}(l_i s_i)(l_j s_j) \right\rangle = \langle i|ls|i\rangle \langle j|ls|j\rangle \left(\left\langle ij|\frac{1}{r_{12}}|ij \right\rangle - \left\langle ij|\frac{1}{r_{12}}|ji \right\rangle \right) \tag{C.16b}$$

with $(k,k') \in \{i,j\}$ and $k \neq k'$. Furthermore, with

$$\left\langle \frac{1}{r_{12}}(l_1 s_1)^2 \right\rangle + \left\langle \frac{1}{r_{12}}(l_2 s_2)^2 \right\rangle = \left(\left\langle 12|\frac{1}{r_{12}}|12 \right\rangle - \left\langle 12|\frac{1}{r_{12}}|21 \right\rangle \right) \left(\left\langle 1|(ls)^2|1 \right\rangle + \left\langle 2|(ls)^2|2 \right\rangle \right) \tag{C.17a}$$

$$2 \times \left\langle \frac{1}{r_{12}}(l_1 s_1)(l_2 s_2) \right\rangle = 2 \times \langle 1|(ls)|1\rangle \langle 2|(ls)|2\rangle \left(\left\langle 12|\frac{1}{r_{12}}|12 \right\rangle - \left\langle 12|\frac{1}{r_{12}}|21 \right\rangle \right) \tag{C.17b}$$

one gets

$$\langle W_2 \rangle_2 = \frac{1}{g_2}\frac{1}{2} \sum_{j_1,m_1} \sum_{j_2,m_2} \left(\left\langle 12|\frac{1}{r_{12}}|12 \right\rangle - \left\langle 12|\frac{1}{r_{12}}|21 \right\rangle \right) (\langle 1|ls|1\rangle + \langle 2|ls|2\rangle)^2 \tag{C.18}$$

where $(\langle 1|ls|1\rangle + \langle 2|ls|2\rangle)^2 = \frac{1}{4}x(j_1,j_2,l)$.

The average formula of $\langle W_2 \rangle_2$ is given by

$$\begin{aligned}\langle W_2 \rangle_2 &= \frac{1}{8g_2}\left(\sum_{j_1,j_2} F^0(ll)[j_1,j_2]x(j_1,j_2,l) - \sum_{j_1,j_2,k} X_k[j_1,j_2]x(j_1,j_2,l)\begin{Bmatrix} j_1 & k & j_2 \\ l & s & l \end{Bmatrix}^2\right) \\ &= \frac{1}{8g_2}(D-E) \end{aligned} \tag{C.19}$$

where in terms of the j_1, j_2, k summations,

$$D = \sum_{j_1=l-1/2}^{l+1/2}\sum_{j_2}^{l+1/2} F^0(ll)[j_1,j_2]x(j_1,j_2,l) \tag{C.20}$$

$$E = \sum_k \sum_{j_1}\sum_{j_2} X_k[j_1,j_2]x(j_1,j_2,l)\begin{Bmatrix} j_1 & k & j_2 \\ l & s & l \end{Bmatrix}^2 \tag{C.21}$$

Using Mathematica for example, the double summation in the D term can be easily determined,

$$D = 8F^0(ll)l(l+1)(2l+1)^2 \tag{C.22}$$

whereas due to the sums over 6j-symbols $\sum_{j_1}\sum_{j_2}...\begin{Bmatrix} j_1 & k & j_2 \\ l & s & l \end{Bmatrix}^2$, the E term requires more development,

$$\begin{aligned} E = &\sum_k X_k[l+\frac{1}{2},l+\frac{1}{2}]\begin{Bmatrix} l+\frac{1}{2} & k & l+\frac{1}{2} \\ l & \frac{1}{2} & l \end{Bmatrix}^2 x(j_1 = l+\frac{1}{2}, j_2 = l+\frac{1}{2}, l) \\ &+\sum_k X_k[l-\frac{1}{2},l-\frac{1}{2}]\begin{Bmatrix} l-\frac{1}{2} & k & l-\frac{1}{2} \\ l & \frac{1}{2} & l \end{Bmatrix}^2 x(j_1 = l-\frac{1}{2}, j_2 = l-\frac{1}{2}, l) \\ &+2\sum_k X_k[l+\frac{1}{2},l-\frac{1}{2}]\begin{Bmatrix} l-\frac{1}{2} & k & l+\frac{1}{2} \\ l & \frac{1}{2} & l \end{Bmatrix}^2 x(j_1 = l+\frac{1}{2}, j_2 = l-\frac{1}{2}, l) \end{aligned} \tag{C.23a}$$

decomposing further with

$$E_1 = [l,l,l+\frac{1}{2},l+\frac{1}{2}]\begin{Bmatrix} l+\frac{1}{2} & k & l+\frac{1}{2} \\ l & \frac{1}{2} & l \end{Bmatrix}^2 = (1+2l-k)(2+2l+k)$$

$$E_2 = [l,l,l-\frac{1}{2},l-\frac{1}{2}]\begin{Bmatrix} l-\frac{1}{2} & k & l-\frac{1}{2} \\ l & \frac{1}{2} & l \end{Bmatrix}^2 = (2l-k)(1+2l+k)$$

$$E_3 = [l,l,l+\frac{1}{2},l-\frac{1}{2}]\begin{Bmatrix} l-\frac{1}{2} & k & l+\frac{1}{2} \\ l & \frac{1}{2} & l \end{Bmatrix}^2 = k(1+k)$$

$$x(++) = x(j_1 = l+\frac{1}{2}, j_2 = l+\frac{1}{2}, l) = 4l^2$$

$$x(--) = x(j_1 = l-\frac{1}{2}, j_2 = l-\frac{1}{2}, l) = 4(l+1)^2$$

$$x(+-) = x(j_1 = l+\frac{1}{2}, j_2 = l-\frac{1}{2}, l) = 1$$

the Eq.(C.23a) can be simplified as

$$E = \sum_k X_k \cdot (x(++)E_1 + x(--)E_2 + 2x(+-)E_3)/[l,l] \tag{C.23b}$$

$$= -2\sum_k X_k \cdot (k(k+1) - 4l(l+1)) \tag{C.23c}$$

Therefore,

$$\boxed{\langle W_2\rangle_2 = \frac{1}{g_2}\left(l(l+1)[l,l]F^0(ll) - l(l+1)\sum_k X_k + \frac{1}{4}\sum_k k(k+1)X_k\right)} \tag{C.24}$$

C.2.2 Average of 3-electron operator : $\langle W_3\rangle$

In a three-particle coupled basis,

$$\langle W_3\rangle_3 = \frac{1}{g_3}\sum_P (-1)^\tau \langle ijp|W_3|\tau(i)\tau(j)\tau(p)\rangle \tag{C.25}$$

where

$$\frac{1}{g_3} = \binom{4l+2}{3}^{-1} = \frac{3}{2l(1+4l)(2+4l)}. \tag{C.26}$$

Furthermore, the summation over permutations of three particles contains 3! terms: $(+|ijp\rangle, +|jpi\rangle, +|pij\rangle, -|jip\rangle, -|ipj\rangle, -|pji\rangle)$, which means that

$$\sum_P (-1)^\tau \langle ijp|O|\tau(i)\tau(j)\tau(p)\rangle = \langle ijp|O|ijp\rangle + \langle ijp|O|jpi\rangle + \langle ijp|O|pij\rangle$$
$$- \langle ijp|O|jip\rangle - \langle ijp|O|ipj\rangle - \langle ijp|O|pji\rangle \tag{C.27}$$

Based on the expressions of W_3 operator, cf. Eqs. (C.9)(C.10c), one gets $\langle W_3\rangle = \langle S\rangle + \langle C\rangle$, where

$$\langle S\rangle = \frac{1}{2}\sum_i\sum_j\sum_p \left\langle \frac{1}{r_{ij}}(l_p s_p)^2 \right\rangle \tag{C.28}$$

$$\langle C\rangle = \sum_i\sum_j\sum_p \left\langle \frac{1}{r_{ij}}(l_i s_i)(l_p s_p) + \frac{1}{r_{ij}}(l_j s_j)(l_p s_p) \right\rangle. \tag{C.29}$$

The squared term of the average over 6 permutation states : $\langle S\rangle$

The trace over 6 permutation states is given by

$$\left\langle \frac{1}{r_{ij}}(l_p s_p)^2 \right\rangle = \left(\left\langle ij|\frac{1}{r_{12}}|ij\right\rangle - \left\langle ij|\frac{1}{r_{12}}|ji\right\rangle\right)\left(\left\langle p|(ls)^2|p\right\rangle - \left\langle i|(ls)^2|i\right\rangle - \left\langle j|(ls)^2|j\right\rangle\right) \tag{C.30}$$

which can be further separated into 2 parts $\langle S \rangle = \langle S_0 \rangle + \langle S_k \rangle$, with

$$\langle S_0 \rangle = \frac{1}{2} \sum_i \sum_j \left\langle ij|\frac{1}{r}|ij \right\rangle \sum_p \left\langle p|(ls)^2|p \right\rangle - \sum_i \sum_j \left\langle ij|\frac{1}{r}|ij \right\rangle \left\langle j|(ls)^2|j \right\rangle \tag{C.31}$$

$$\langle S_k \rangle = -\frac{1}{2} \sum_i \sum_j \left\langle ij|\frac{1}{r}|ji \right\rangle \sum_p \left\langle p|(ls)^2|p \right\rangle + \sum_i \sum_j \left\langle ij|\frac{1}{r}|ji \right\rangle \left\langle j|(ls)^2|j \right\rangle \tag{C.32}$$

Using closure relation for matrix computation, one gets

$$\langle S_0 \rangle = 2l^2(l+1)(1+2l)^2 F^0(ll), \quad \langle S_k \rangle = -l^2(l+1)(1+2l)^2 \sum_k X_k$$

The crossed term of the average over 6 permutation states : $\langle C \rangle$

Since

$$\left\langle \frac{1}{r_{ij}}(l_p s_p)(l_k s_k) \right\rangle = \left(\left\langle ij|\frac{1}{r_{12}}|ij \right\rangle \langle k|ls|k\rangle - \left\langle ij|\frac{1}{r_{12}}|ji \right\rangle \langle k'|ls|k'\rangle \right) (\langle p|ls|p\rangle - \langle i|ls|i\rangle - \langle j|ls|j\rangle) \tag{C.34}$$

with $(k,k') \in \{i,j\}$ and $k \neq k'$,

$$\begin{aligned} \left\langle \frac{1}{r_{ij}}(l_i s_i)(l_p s_p) + \frac{1}{r_{ij}}(l_j s_j)(l_p s_p) \right\rangle = & \left\langle ij|\frac{1}{r}|ij \right\rangle \times (\langle i|ls|i\rangle + \langle j|ls|j\rangle)(\langle p|ls|p\rangle - \langle i|ls|i\rangle - \langle j|ls|j\rangle) \\ & - \left\langle ij|\frac{1}{r}|ji \right\rangle \times (\langle i|ls|i\rangle + \langle j|ls|j\rangle)(\langle p|ls|p\rangle - \langle i|ls|i\rangle - \langle j|ls|j\rangle). \end{aligned} \tag{C.35a}$$

All terms with $\langle p|ls|p\rangle$ as factor vanish, so that

$$\left\langle \frac{1}{r_{ij}}(l_i s_i)(l_p s_p) + \frac{1}{r_{ij}}(l_j s_j)(l_p s_p) \right\rangle = \langle C_0 \rangle + \langle C_k \rangle \tag{C.35b}$$

with

$$\langle C_0 \rangle = -\left\langle ij|\frac{1}{r}|ij \right\rangle \times (\langle i|ls|i\rangle + \langle j|ls|j\rangle)^2 = -2l(l+1)(1+2l)^2 F^0(ll) \tag{C.35c}$$

$$\langle C_k \rangle = \left\langle ij|\frac{1}{r}|ji \right\rangle \times (\langle i|ls|i\rangle + \langle j|ls|j\rangle)^2 = -\frac{1}{2} \sum_k k(k+1) X_k + 2l(l+1) \sum_k X_k \tag{C.35d}$$

Finally, in order to obtain $\langle W_3 \rangle$, it's sufficient to sum up the direct part $\langle S_0 \rangle + \langle C_0 \rangle$ and the exchange part $\langle S_k \rangle + \langle C_k \rangle$, which gives

$$\boxed{\langle W_3 \rangle_3 = \frac{1}{g_3} \left(A(l)[l,l] F^0(ll) + B(l) \sum_k X_k - \frac{1}{2} \sum_k C(k) X_k \right)} \tag{C.36a}$$

$$\text{with} \quad A(l) = 2l(l-1)(l+1), \quad B(l) = l(l+1)(2-l), \quad C(k) = k(k+1). \tag{C.36b}$$

C.2.3 Average of 4-electron operator : $\langle W_4\rangle$

Similarly, in a four-particle coupled basis,

$$\langle W_4\rangle_4 = \frac{1}{g_4}\sum_P (-1)^\tau \langle ijpq|W_4|\tau(i)\tau(j)\tau(p)\tau(q)\rangle \tag{C.37}$$

one gets

$$\frac{1}{g_4} = \binom{4l+2}{4}^{-1} = \frac{6}{l(4l-1)(4l+1)(4l+2)}. \tag{C.38}$$

The summation over permutations – even $(-1)^\tau = 1$ and odd $(-1)^\tau = -1$ ones – of four particles contains 4!=24 terms : $\begin{array}{c|c|cccccccccc} (-1)^\tau=1 & |ijpq\rangle & |ipqj\rangle & |iqjp\rangle & |jiqp\rangle & |jpiq\rangle & |jqpi\rangle & |pijq\rangle & |pjqi\rangle & |pqij\rangle & |qi \\ \hline (-1)^\tau=-1 & |ijqp\rangle & |ipjq\rangle & |iqpj\rangle & |jipq\rangle & |jpqi\rangle & |jqip\rangle & |piqj\rangle & |pjiq\rangle & |pqji\rangle & |qi \end{array}$ which can be regrouped into 10 categories, listed in Table C.1. Since due to the symmetry properties of the operator $\frac{1}{r_{12}}(l_3s_3)(l_4s_4)$, several matrix elements contribute to the average value $\langle W_4\rangle_4$ in the same way . The last 5 terms give null contribution to the average calculation,

Table C.1: Regroupment by symmetry: reduction of the 24 terms into 10 contribution terms. Only the first five terms contribute to the average calculation.

Index	States
1	$(34) = \|ijqp\rangle$
2	$(12)(34) = \|jiqp\rangle$
3	$(134) = \|pjqi\rangle, (143) = \|qjip\rangle, (234) = \|ipqj\rangle, (243) = \|iqjp\rangle$
4	$(1234) = \|jpqi\rangle, (1342) = \|piqj\rangle, (1243) = \|jqip\rangle, (1432) = \|qijp\rangle$
5	$(1324) = \|pqji\rangle, (1423) = \|qpij\rangle$
6	identity=$\|ijpq\rangle$
7	$(12) = \|jipq\rangle$
8	$(13) = \|pjiq\rangle, (14) = \|qjpi\rangle, (23) = \|ipjq\rangle, (24) = \|iqpj\rangle$
9	$(13)(24) = \|pqij\rangle, (14)(23) = \|qpji\rangle$
10	$(123) = \|jpiq\rangle, (124) = \|jqpi\rangle, (132) = \|pijq\rangle, (142) = \|qipj\rangle$

and the first 5 terms represent 5 types of matrix elements to be calculated applying the closure relations.

1. (34) : $\sum_{ijpq}\left\langle ijpq|\frac{1}{r_{12}}(l_3s_3)(l_4s_4)|ijqp\right\rangle = \sum_{ijp}\left\langle ij|\frac{1}{r}|ij\right\rangle\langle p|(ls)^2|p\rangle$

$$\sum_{ij}\left\langle ij|\frac{1}{r}|ij\right\rangle\sum_p\left\langle p|(ls)^2|p\right\rangle = 4(1+2l)^2F^0(ll)\cdot\frac{l(1+l)(1+2l)}{2} = 2l(1+l)(1+2l)^3F^0(ll) \tag{C.39}$$

2. $(12)(34)$: $\sum_{ijpq}\left\langle ijpq|\frac{1}{r_{12}}(l_3s_3)(l_4s_4)|jiqp\right\rangle = \sum_{ijp}\left\langle ij|\frac{1}{r}|ji\right\rangle\langle p|(ls)^2|p\rangle$

$$\sum_{ij}\left\langle ij|\frac{1}{r}|ji\right\rangle\sum_p\left\langle p|(ls)^2|p\right\rangle = 2\sum_k X_k\frac{l(1+l)(1+2l)}{2} = l(1+l)(1+2l)\sum_k X_k \tag{C.40}$$

3. (243) : $\sum_{ijpq}\left\langle ijpq|\frac{1}{r_{12}}(l_3s_3)(l_4s_4)|iqjp\right\rangle = \sum_{ij}\left\langle ij|\frac{1}{r}|ij\right\rangle\langle j|(ls)^2|j\rangle$

$$\sum_{ij}\left\langle ij|\frac{1}{r}|ij\right\rangle\left\langle j|(ls)^2|j\right\rangle = \sum_{j_1j_2}[j_1,j_2]F^0(ll)\times\frac{(j_2(j_2+1)-l(l+1)-3/4)^2}{4} = l(1+l)(1+2l)^2F^0(ll) \tag{C.41}$$

4. (1432) : $\sum_{ijpq}\left\langle ijpq|\frac{1}{r_{12}}(l_3s_3)(l_4s_4)|qijp\right\rangle = \sum_{ij}\left\langle ij|\frac{1}{r}|ji\right\rangle\langle j|(ls)^2|j\rangle$

$$\sum_{ij}\left\langle ij|\frac{1}{r}|ji\right\rangle\left\langle j|(ls)^2|j\right\rangle = E_1x(+)+E_2x(-)+E_3(x(+)+x(-)) = \frac{l(1+l)}{2}\sum_k X_k \tag{C.42}$$

where $x(j)=\langle j|(ls)^2|j\rangle = [(j(j+1)-l(l+1)-3/4)^2]/4$

5. (1423) : $\sum_{ijpq}\left\langle ijpq|\frac{1}{r_{12}}(l_3s_3)(l_4s_4)|qpij\right\rangle = \sum_{ij}\left\langle ij|\frac{1}{r}|ji\right\rangle\langle i|(ls)|i\rangle\langle j|(ls)|j\rangle$

$$\sum_{ij}\left\langle ij|\frac{1}{r}|ji\right\rangle\langle i|(ls)|i\rangle\langle j|(ls)|j\rangle = -\frac{1}{4}\sum_k k(k+1)X_k+\frac{l(l+1)}{2}\sum_k X_k \tag{C.43}$$

The non-zero part of $\langle W_4\rangle_4 = \frac{1}{2}(-(34)+(12)(34)+4\cdot(243)-4\cdot(1432)-2\cdot(1423))$.

$$\boxed{\langle W_4\rangle_4 = \frac{1}{g_4}\left(l(1+l)(1-2l)[l,l]F^0(ll)+l(l+1)(l-1)\sum_k X_k+\frac{1}{4}\sum_k k(k+1)X_k\right)} \tag{C.44}$$

Finally, using the Uylings theorem, cf. Eq.(4.4), the average calculations of product $V_{\rm ee}V_{\rm so}^2$ operators give rise to

$$\left\langle V_{\rm ee}V_{\rm so}^2\right\rangle = \binom{N}{2}\langle W_2\rangle_2+\binom{N}{3}\langle W_3\rangle_3+\binom{N}{4}\langle W_4\rangle_4, \tag{C.45}$$

where the average values of k-particle operators $W_k(k=2,3,4)$ are derived previously whose results are shown in the boxed equations above.

Bibliography

Articles

[A8] C Chenais-Popovics et al. "Radiative heating of B, Al and Ni thin foils at 15V temperatures". In: *J. Quant. Spectrosc. Radiat. Transfer* 65, 2000, pp. 117 –133. URL: http://www.sciencedirect.com/science/article/pii/S0022407399000618 (cit. on p. 22).

[A9] J. M. Foster et al. "L-shell absorption spectrum of an open-M-shell germanium plasma: Comparison of experimental data with a detailed configuration-accounting calculation". In: *Phys. Rev. Lett.* 67, 1991, pp. 3255–3258. URL: https://link.aps.org/doi/10.1103/PhysRevLett.67.3255 (cit. on p. 22).

[A10] Y. Aglitskiy et al. "X-ray emission from plasmas created by smoothed KrF laser irradiation". In: *Phys. Plasmas* 3, 1996, pp. 3438–3447 (cit. on p. 22).

[A11] T.S. Perry et al. "Quantitative measurement of mid-Z opacities". In: *J. Quant. Spectrosc. Radiat. Transfer* 54, 1995. Radiative Properties of Hot Dense Matter II, pp. 317 –324. URL: http://www.sciencedirect.com/science/article/pii/002240739500066T (cit. on p. 22).

[A12] G. Loisel et al. "Absorption spectroscopy of mid and neighboring Z plasmas : iron, nickel, copper and germanium". In: *High Energy Density Phys.* 5, 2009, pp. 173–181 (cit. on p. 22).

[A13] J. E. Bailey et al. "A higher-than-predicted measurement of iron opacity at solar interior temperatures". In: *Nature* 517, 2015, pp. 56–59. URL: http://dx.doi.org/10.1038/nature14048 (cit. on p. 22).

[A14] M J Seaton. "Atomic data for the calculation of radiative accelerations and diffusion of Mn in HgMn stars". In: *Physica Scripta* 1996, 1996, p. 129. URL: http://stacks.iop.org/1402-4896/1996/i=T65/a=018 (cit. on p. 22).

[A15] M. J. Seaton. "Radiative accelerations in stellar envelopes". In: *Mon. Not. R. Astron. Soc.* 289, 1997, pp. 700–720 (cit. on p. 22).

[A16] J.-F. Gonzalez et al. "Improvements on radiative acceleration calculations in stellar envelopes". In: *Astron. Astrophys.* 297, 1995, pp. 223–236 (cit. on p. 22).

[A17] J.-F. Gonzalez, M.-C. Artru, and G. Michaud. "Radiative accelerations on carbon, nitrogen and oxygen." In: *Astron. Astrophys.* 302, 1995, p. 788 (cit. on p. 22).

[A21] Bengt Edlén. "Spectra of highly ionized atoms". In: *Physica* 13, 1947, pp. 545 –554. URL: http://www.sciencedirect.com/science/article/pii/0031891447900232 (cit. on p. 23).

[A22] Steven A. Moszkowski. “On the energy distribution of terms and line arrays in atomic spectra”. In: *Progress of Theoretical Physics* 28, 1962, p. 1. URL: http://ptp.oxfordjournals.org/content/28/1/1.abstract (cit. on pp. 23, 49).

[A23] C. Bauche-Arnoult, J. Bauche, and M. Klapisch. “Variance of the distributions of energy levels and of the transition arrays in atomic spectra. III. Case of spin-orbit-split arrays”. In: *Phys. Rev. A* 31, 1985, pp. 2248–2259 (cit. on p. 23).

[A24] A. Bar-Shalom et al. “Super-transition-arrays: A model for the spectral analysis of hot, dense plasma”. In: *Phys. Rev. A* 40, 1989, pp. 3183–3193 (cit. on p. 23).

[A25] J.-C. Pain et al. “The hybrid opacity code SCO-RCG: recent developments”. In: *ArXiv e-prints*, 2013 (cit. on p. 23).

[A26] J.-C. Pain et al. “The Hybrid Detailed / Statistical Opacity Code SCO-RCG: New Developments and Applications”. In: *ArXiv e-prints*, 2013 (cit. on p. 23).

[A28] A. Bar-Shalom, M. Klapisch, and J. Oreg. “HULLAC, an integrated computer package for atomic processes in plasmas”. In: *Journal of Quantitative Spectroscopy and Radiative Transfer* 71, 2001. Radiative Properties of Hot Dense Matter, pp. 169 –188. URL: http://www.sciencedirect.com/science/article/pii/S0022407301000668 (cit. on p. 23).

[A30] M F Gu. “The flexible atomic code”. In: *Can. J. Phys.* 86, 2008, pp. 675–689 (cit. on pp. 23, 35, 36, 53, 73).

[A32] Xieyu Na and M. Poirier. “High-order moments of spin-orbit energy in a multielectron configuration”. In: *Phys. Rev. E* 94, 2016, p. 013206. URL: https://link.aps.org/doi/10.1103/PhysRevE.94.013206 (cit. on pp. 23, 49, 57, 68, 95).

[A33] Xieyu Na and Michel Poirier. “Analysis of magnetic-dipole transitions in tungsten plasmas using detailed and configuration-average descriptions”. In: *High Energy Density Physics* 23, 2017, pp. 200 –206. URL: http://www.sciencedirect.com/science/article/pii/S1574181817300435 (cit. on pp. 23, 54, 57).

[A35] J. C. Slater. “The Theory of Complex Spectra”. In: *Phys. Rev.* 34, 1929, pp. 1293–1322. URL: https://link.aps.org/doi/10.1103/PhysRev.34.1293 (cit. on p. 25).

[A37] G Racah. “Theory of Complex Spectra. I”. In: *Phys. Rev.* 61, 1942, pp. 186–197. URL: https://link.aps.org/doi/10.1103/PhysRev.61.186 (cit. on pp. 25, 50).

[A38] G Racah. “Theory of Complex Spectra. II”. In: *Phys. Rev.* 62, 1942, pp. 438–462. URL: https://link.aps.org/doi/10.1103/PhysRev.62.438 (cit. on pp. 25, 50).

[A45] Robert D. Cowan. “Theoretical Calculation of Atomic Spectra Using Digital Computers*”. In: *J. Opt. Soc. Am.* 58, 1968, pp. 808–818. URL: http://www.osapublishing.org/abstract.cfm?URI=josa-58-6-808 (cit. on pp. 33, 34).

[A46] P H M Uylings. “Extended theory of the spin-orbit interaction”. In: *Journal of Physics B: Atomic, Molecular and Optical Physics* 22, 1989, p. 2947. URL: http://stacks.iop.org/0953-4075/22/i=19/a=008 (cit. on p. 33).

[A48] Douglas H. Sampson, Hong Lin Zhang, and Christopher J. Fontes. “A fully relativistic approach for calculating atomic data for highly charged ions”. In: *Physics Reports* 477, 2009, pp. 111 –214. URL: http://www.sciencedirect.com/science/article/pii/S037015730900129X (cit. on p. 36).

[A52] J. Bauche, C. Bauche-Arnoult, and O. Peyrusse. "Effective temperatures in hot dense plasmas". In: *J. Quant. Spectrosc. Radiat. Transfer* 99, 2006, pp. 55 –66. URL: http://www.sciencedirect.com/science/article/pii/S0022407305001330 (cit. on p. 41).

[A53] S.B. Hansen et al. "A comparison of detailed level and superconfiguration models of neon". In: *J. Quant. Spectrosc. Radiat. Transfer* 99, 2006, pp. 272 –282. URL: http://www.sciencedirect.com/science/article/pii/S0022407305001524 (cit. on p. 41).

[A54] Christoph Biedermann et al. "Spectroscopy of highly charged tungsten ions relevant to fusion plasmas". In: *Phys. Scr.* 2009, 2009, p. 014026. URL: http://stacks.iop.org/1402-4896/2009/i=T134/a=014026 (cit. on pp. 41, 73).

[A55] C.J. Fontes et al. "Review of the NLTE-5 kinetics workshop". In: *High Energy Density Phys.* 5, 2009, pp. 15 –22. URL: http://www.sciencedirect.com/science/article/pii/S1574181809000056 (cit. on p. 41).

[A56] H.-K. Chung et al. "Comparison and analysis of collisional-radiative models at the NLTE-7 workshop". In: *High Energy Density Phys.* 9, 2013, pp. 645 –652. URL: http://www.sciencedirect.com/science/article/pii/S157418181300147X (cit. on p. 41).

[A57] H.-K. Chung et al. "FLYCHK: Generalized population kinetics and spectral model for rapid spectroscopic analysis for all elements". In: *High Energy Density Phys.* 1, 2005, p. 3. URL: https://e-reports-ext.llnl.gov/pdf/321476.pdf (cit. on p. 42).

[A58] Robert C. Hilborn. "Einstein coefficients, cross sections, f values, dipole moments, and all that". In: *American Journal of Physics* 50, 1982, pp. 982–986. URL: http://dx.doi.org/10.1119/1.12937 (cit. on pp. 43, 44).

[A60] S.R. Drayson. "Rapid computation of the Voigt profile". In: *J. Quant. Spectrosc. Radiat. Transfer* 16, 1976, pp. 611 –614. URL: http://www.sciencedirect.com/science/article/pii/0022407376900297 (cit. on p. 46).

[A62] C. Bauche-Arnoult, J. Bauche, and M. Klapisch. "Variance of the distributions of energy levels and of the transition arrays in atomic spectra". In: *Phys. Rev. A* 20, 1979, pp. 2424–2439 (cit. on p. 47).

[A63] J. Bauche, C. Bauche-Arnoult, and M. Klapisch. "Transition Arrays in the Spectra of Ionized Atoms". In: *Adv. At. Mol. Phys.* 23, 1988. Ed. by David Bates and Benjamin Bederson, pp. 131–195 (cit. on pp. 47, 49, 58).

[A65] E. Nardi and Z. Zinamon. "Radiative opacity of high-temperature and high-density gold". In: *Phys. Rev. A* 20, 1979, pp. 1197–1200. URL: http://link.aps.org/doi/10.1103/PhysRevA.20.1197 (cit. on p. 49).

[A66] R. Karazija. "Evaluation of explicit expressions for mean characteristics of atomic spectra". In: *Acta Phys. Hung.* 70, 1991, pp. 367–379. URL: http://dx.doi.org/10.1007/BF03054151 (cit. on p. 49).

[A67] S Kučas and R Karazija. "Global characteristics of atomic spectra and their use for the analysis of spectra. I. Energy level spectra". In: *Phys. Scr.* 47, 1993, p. 754. URL: http://stacks.iop.org/1402-4896/47/i=6/a=012 (cit. on pp. 49, 62, 95).

[A72] J.-Ch. Pain et al. "Effect of third- and fourth-order moments on the modeling of unresolved transition arrays". In: *High Energy Density Physics* 5, 2009, pp. 294 –301. URL: http://www.sciencedirect.com/science/article/pii/S1574181809000433 (cit. on pp. 51, 53).

[A73] P H M Uylings. "Energies of N equivalent electrons expressed in terms of two-electron energies and independent three-electron parameters: a new complete set of orthogonal operators. I. Theory". In: *J. Phys. B: At. Mol. Opt. Phys.* 17, 1984, p. 2375. URL: http://stacks.iop.org/0022-3700/17/i=12/a=009 (cit. on p. 58).

[A74] F Rajadell, J Planelles, and J Karwowski. "Traces of powers of the Hamiltonian operator in finite-dimensional antisymmetric model spaces". In: *Journal of Physics A: Mathematical and General* 26, 1993, p. 3883. URL: http://stacks.iop.org/0305-4470/26/i=15/a=036 (cit. on p. 58).

[A75] Jean-Christophe Pain et al. "Statistics of electric-quadrupole lines in atomic spectra". In: *J. Phys. B: At. Mol. Opt. Phys.* 45, 2012, p. 135006. URL: http://stacks.iop.org/0953-4075/45/i=13/a=135006 (cit. on pp. 72, 73).

[A76] Franck Gilleron et al. "Impact of high-order moments on the statistical modeling of transition arrays". In: *Phys. Rev. E* 77, 2008, p. 026708. URL: http://link.aps.org/doi/10.1103/PhysRevE.77.026708 (cit. on pp. 72, 77).

[A77] A. Bar-Shalom, J. Oreg, and W. H. Goldstein. "Effect of configuration widths on the spectra of local thermodynamic equilibrium plasmas". In: *Phys. Rev. E* 51, 1995, pp. 4882–4890. URL: http://link.aps.org/doi/10.1103/PhysRevE.51.4882 (cit. on p. 73).

[A78] Menahem Krief and Alexander Feigel. "Variance and shift of transition arrays for electric and magnetic multipole transitions". In: *High Energy Density Phys.* 17, 2015, pp. 254 –262. URL: http://www.sciencedirect.com/science/article/pii/S1574181815000695 (cit. on p. 73).

[A80] R. Radtke et al. "Line and band emission from tungsten ions with charge 21+ to 45+ in the 45-–70Å range". In: *Phys. Rev. A* 64, 2001, p. 012720. URL: http://link.aps.org/doi/10.1103/PhysRevA.64.012720 (cit. on p. 73).

[A81] Yu. Ralchenko et al. "Spectroscopy of diagnostically important magnetic-dipole lines in highly charged $3d^n$ ions of tungsten". In: *Phys. Rev. A* 83, 2011, p. 032517. URL: http://link.aps.org/doi/10.1103/PhysRevA.83.032517 (cit. on p. 74).

[A82] George H. Shortley. "The Computation of Quadrupole and Magnetic-Dipole Transition Probabilities". In: *Phys. Rep.* 57, 1940, pp. 225–234. URL: http://link.aps.org/doi/10.1103/PhysRev.57.225 (cit. on p. 75).

[A84] C. Bauche-Arnoult, J. Bauche, and M. Klapisch. "Asymmetry of $l^{N+1} - l^N l'$ transition-array patterns in ionic spectra". In: *Phys. Rev. A* 30, 1984, pp. 3026–3032. URL: http://link.aps.org/doi/10.1103/PhysRevA.30.3026 (cit. on p. 77).

[A85] J.-C. Pain. "Regularities and symmetries in atomic structure and spectra". In: *High Energy Density Physics* 9, 2013, pp. 392–401 (cit. on p. 84).

[A86] S Mazevet and J Abdallah Jr. "Mixed UTA and detailed line treatment for mid- Z opacity and spectral calculations". In: *Journal of Physics B: Atomic, Molecular and Optical Physics* 39, 2006, p. 3419. URL: http://stacks.iop.org/0953-4075/39/i=16/a=022 (cit. on p. 84).

[A87] S.B. Hansen et al. “Hybrid atomic models for spectroscopic plasma diagnostics”. In: *High Energy Density Physics* 3, 2007. Radiative Properties of Hot Dense Matter, pp. 109 –114. URL: http://www.sciencedirect.com/science/article/pii/S1574181807000171 (cit. on p. 84).

[A88] Carlos A. Iglesias and Vijay Sonnad. “Partially resolved transition array model for atomic spectra”. In: *High Energy Density Physics* 8, 2012, pp. 154 –160. URL: http://www.sciencedirect.com/science/article/pii/S157418181200002X (cit. on p. 84).

Proceedings

[P19] C. J. Keane. “Atomic physics in Inertial Confinement Fusion (ICF)”. In: *American Institute of Physics Conference Series*. Vol. 443. American Institute of Physics Conference Series. 1998, pp. 281–281 (cit. on p. 22).

[P27] J.-C. Pain et al. “The hybrid detailed / statistical opacity code SCO-RCG: New developments and applications”. In: *AIP Conference Proceedings*. Vol. 1811. 2017 (cit. on p. 23).

[P61] J.-C. Pain and F. Gilleron. “Statistical properties of levels and lines in complex spectra: a tribute to Jacques Bauche and Claire Bauche-Arnoult”. In: *AIP Conference Proceedings*. Vol. 1811. 2017 (cit. on pp. 47, 84).

[P79] Y. Ralchenko et al. “Multi-Code Ab Initio Calculation of Ionization Distributions and Radiation Losses for Tungsten in Tokamak Plasmas”. In: *American Institute of Physics Conference Series*. Ed. by K. B. Fournier. Vol. 1161. American Institute of Physics Conference Series. 2009, pp. 242–250 (cit. on p. 73).

Books

[B1] T.J.M. Boyd and J.J. Sanderson. *The Physics of Plasmas*. United Kingdom: Cambridge University Press, 2003. ISBN: 978-0-521-45912-5 (cit. on pp. 19, 21).

[B3] Francis F. Chen. *Introduction to Plasma Physics and Controlled Fusion*. US: Springer US, 1984. ISBN: 978-1-4419-3201-3 (cit. on p. 21).

[B4] David Salzmann. *Atomic Physics in Hot Plasmas*. 198 Madison Avenue, New York, 10016: Oxford University Press, Inc, 1998. ISBN: 0-19-510930-9 (cit. on pp. 22, 39, 45).

[B18] R. Neu. *Tungsten as a Plasma Facing Material in Fusion Devices*. IPP (Series : Garching bei München, Germany). IPP, 2003. URL: https://books.google.fr/books?id=Tj5NNQAACAAJ (cit. on p. 22).

[B20] Jacques Bauche, Claire Bauche-Arnoult, and Olivier Peyrusse. *Atomic properties in hot plasmas. From levels to superconfigurations*. Berlin: Springer-Verlag, 2015. ISBN: 978-3-319-18146-2 (cit. on pp. 23, 26, 47, 49–51, 61, 68).

[B34] Z. Rudzikas. *Theoretical Atomic Spectroscopy*. Cambridge Monographs on Atomic, Molecular and Chemical Physics. Cambridge University Press, 1997. ISBN: 9780521444255. URL: https://books.google.fr/books?id=MDqLnQAACAAJ (cit. on pp. 25, 30).

[B36] E.U.Condon and G.H.Shortley. *The Theory of Atomic Spectra*. 198 Madison Avenue, New York, 10016: Cambridge University Press, 1935. ISBN: 978-0-521-09209-8 (cit. on pp. 25, 47).

[B39] B. R. Judd. *Second quantization and atomic spectroscopy*. Baltimore, Maryland: John Hopkins Press, 1967 (cit. on p. 25).

[B40] R. D. Cowan. *The theory of atomic structure and spectra*. Berkeley, California: University of California Press, 1981 (cit. on pp. 26, 28, 32, 33, 35, 37, 38, 49, 57, 67, 75, 92, 98).

[B41] I.P.Grant. *Relativistic Quantum Theory of Atoms and Molecules*. Plenum Press, New York: Springer US, 2007. ISBN: 978-1-4612-8044-6 (cit. on pp. 26–28, 30, 88).

[B42] Walter R. Johnson. *Atomic Structure Theory. Lectures on Atomic Physics*. Berlin: Springer-Verlag, 2007. ISBN: 978-3-642-08762-2 (cit. on pp. 27, 30, 89, 92).

[B50] Hans R. Griem. *Principles of Plasma Spectroscopy*. Cambridge Monographs on Plasma Physics. Cambridge University Press, 1997 (cit. on p. 41).

[B59] M. Abramowitz and I.A. Stegun. *Handbook of Mathematical Functions*. Washington DC, USA: National Bureau of Standards, 1972 (cit. on pp. 46, 52, 72).

[B68] A. Stuart and K. Ord. *Kendall's Advanced Theory of Statistics: Volume 1: Distribution Theory*. Wiley, 2009 (cit. on p. 50).

[B69] Alan Stuart and J. Keith Ord. *Kendall's Advanced Theory of Statistics, Distribution Theory*. Vol. 1. London UK: Charles Griffin and Co, 1987 (cit. on pp. 50, 51, 59).

[B70] Anirban DasGupta. *Asymptotic Theory of Statistics and Probability*. New York: Springer-Verlag, 2008 (cit. on p. 50).

[B83] William H. Press. *Numerical Recipes in Fortran 90. The Art of Scientific Computing*. 198 Madison Avenue, New York, 10016: Cambridge University Press, 2007. ISBN: 9788185618173 (cit. on p. 77).

Web

[W2] http://www.particlecentral.com/plasma_page.html (cit. on p. 19).

[W6] https://en.wikipedia.org/wiki/Plasma_(physics) (cit. on p. 22).

[W29] https://www-amdis.iaea.org/w/index.php/HULLAC (cit. on p. 23).

[W43] https://en.wikipedia.org/wiki/Aufbau_principle (cit. on p. 32).

[W44] https://physics.nist.gov/cgi-bin/ASD/energy1.pl (cit. on p. 32).

[W49] http://www.lanl.gov/projects/dense-plasma-theory/background/physical-regimes.php (cit. on p. 40).

[W51] https://www.comsol.com/blogs/thermodynamic-equilibrium-of-plasmas/ (cit. on p. 41).

[W64] https://en.wikipedia.org/wiki/Moment_(mathematics) (cit. on p. 49).

[W71] https://en.wikipedia.org/wiki/Cumulant_(statistiques) (cit. on p. 50).

[W89] http://scienceworld.wolfram.com/physics/cgs.html (cit. on p. 87).

[W91] https://physics.nist.gov/cuu/Constants/index.html (cit. on p. 88).

Other sources

[O5] H. Zohm. "Physics of Hot Plasmas". In: *Plasma Physics: Confinement, Transport and Collective Effects*. Ed. by Andreas Dinklage et al. Springer Berlin Heidelberg, 2005, pp. 75–93. URL: https://doi.org/10.1007/11360360_4 (cit. on p. 22).

[O7] J. Meichsner. "Low Temperature Plasmas". In: *Plasma Physics: Confinement, Transport and Collective Effects*. Ed. by Andreas Dinklage et al. Springer Berlin Heidelberg, 2005, pp. 95–116. URL: https://doi.org/10.1007/11360360_5 (cit. on p. 22).

[O31] M.F.Gu. *FAC 1.1.1 Manual*. https://github.com/fnevgeny/fac/tree/master/doc (cit. on pp. 23, 36, 53).

[O47] P.Ewart. *Atomic Physics*. https://users.physics.ox.ac.uk/~ewart/Atomic%20Physics%20lecture%20notes%20C%20port.pdf (cit. on p. 35).

[O90] Ambler Thompson and Barry N. Taylor. *Guide for the Use of the International System of Units (SI)*. Ed. by NIST Special Publication 811. https://physics.nist.gov/cuu/pdf/sp811.pdf. 2008 (cit. on pp. 87, 88).

université PARIS-SACLAY | ÉCOLE DOCTORALE Ondes et Matière (EDOM)

Titre : Étude spectroscopique des plasmas hautement ionisés : approches détaillée et statistique

Mots clés : Spectroscopie atomique, ETL, Raies et faisceaux de transition, Méthodes statistiques (UTA, SOSA), Moments de distribution

Résumé : La description des propriétés spectrales des plasmas hautement ionisés – comme ceux rencontrés en fusion nucléaire, en astrophysique et en expérimentation laser-plasmas –peut nécessiter différents types d'interprétation, parmi lesquels l'approche détaillée ou raie-par-raie impliquant de la diagonalisation de l'Hamiltonien du système et, l'approche statistique basée sur la charactérisation des structures spectrales à travers les moments de distribution.

Ce travail de thèse a pour objectif d'étudier et de mettre en oeuvre les méthodes statistiques traitant des cas où de nombreuses raies se regroupent en faisceaux de transition non résolus (UTA pour Unresolved Transition Array).

Pour cela, des études analytique et numérique ont été menées. D'une part, les moments d'ordre élevé de la distribution d'énergies spin-orbite ont été obtenus, en utilisant les techniques de calcul de moyennes qui font intervenir les résultats de la seconde quantification et de l'algèbre de moment angulaire. D'autre part, après avoir implémenté un programme de post-traitement des données atomiques produites par le code FAC (Flexible Atomic Code), en mode détaillée comme en mode UTA, les spectres d'émission et d'absorption des plasmas de tungstène ont été analysés dans les conditions thermodynamiques équivalentes à celles d'un tokamak.
Nous espérons que les travaux de cette thèse permettrons de stimuler de futures analyses sur le calcul des moyennes incluant des processus de transition complexes.

Title : Spectroscopic study of highly ionised plasmas : detailed and statistical approaches

Keywords : Atomic spectroscopy, LTE, Transition lines and arrays, Statistical methods (UTA, SOSA), Distribution moments

Abstract : The description of spectral properties of highly ionized plasmas – as those studied in stellar atmospheres, facilities for nuclear fusion, or laser-plasmas experiments – may require different types of interpretation, among which the detailed line-by-line accounting which relies on Hamiltonian diagonalization and the statistical approach based on the characterization of spectral structures through distribution moments.

My PhD work aims at developing statistical methods dealing with situations where abundant lines gather in Unresolved Transition Arrays (UTA).

To this end, analytical and numerical analysis have been carried out. On one hand, high-order moments of spin-orbit energy have been derived using averaging calculation techniques based on second quantization results and angular momentum algebra. On the other hand, after implementing a post-processing program for both detailed and UTA computations of the Flexible Atomic Code (FAC), emission and absorption spectra of tungsten plasmas have been studied in tokamak-equivalent thermodynamic conditions.
Results of this thesis should hopefully stimulate further analysis on averages computation involving complex transition processes.

Université Paris-Saclay
Espace Technologique / Immeuble Discovery
Route de l'Orme aux Merisiers RD 128 / 91190 Saint-Aubin, France